To the Graduate Council:
I am submitting here with a thesis written by Kamren Sargent entitled "Development of an Aluminum Multi-Material via Sequential Additive Friction Stir Deposition and Wire Arc Additive Manufacturing." I have examined the final paper copy of this thesis for form and content and recommend that it be accepted in partial fulfillment of the requirements for the degree of Master of Science, with a major in Mechanical Engineering.

Bradley Jared, Major Professor

We have read this thesis
and recommend its acceptance:

Bradley Jared

Brett Compton

Eric Lass

Accepted for the Council:

Dixie L. Thompson

Vice Provost and Dean of the Graduate School

To the Graduate Council:
I am submitting here with a thesis written by Kamren Sargent entitled "Development of an Aluminum Multi-Material via Sequential Additive Friction Stir Deposition and Wire Arc Additive Manufacturing." I have examined the final electronic copy of this thesis for form and content and recommend that it be accepted in partial fulfillment of the requirements for the degree of Master of Science, with a major in Mechanical Engineering.

Bradley Jared, Major Professor

We have read this thesis
and recommend its acceptance:

Bradley Jared

Brett Compton

Eric Lass

Accepted for the Council:

Dixie L. Thompson

Vice Provost and Dean of the Graduate School

(Original signatures are on file with official student records.)

Development of an Aluminum Multi-Material via Sequential Additive Friction Stir Deposition and Wire Arc Additive Manufacturing

A Thesis Presented for the

Master of Science

Degree

The University of Tennessee, Knoxville

Kamren Sargent

December 2025

© by Kamren Sargent, 2025
All Rights Reserved.

I dedicate this thesis to my loving wife, Natali. Your unwavering support has made this achievement possible. I am eternally grateful to share not only this accomplishment, but every step of life's journey, with you.

Acknowledgements

I would like to thank my advisor, Dr. Bradley Jared, for providing guidance and teaching me research best practices. I would not be where I am without him, as he provided guidance during a time of uncertainty. He prioritizes his students, even when schedules are filled. He has pushed me to accomplish this feat and I am grateful for his continued support.

I also thank my committee members, Dr. Brett Compton and Dr. Eric Lass as they have given advice and provided different avenues to achieve this accomplishment. They have taken time out to serve on my committee and ensure the completion of my thesis.

I would like to thank all my colleagues within the various research groups at the University of Tennessee. Particularly, Mason Smith, Ben Pollard, Shane Glasser, and Dr. Stephen Puplampu have provided assistance outside of the TN-MADE facility. I would like to thank my colleagues at TN-MADE, and provide a special thank you to Josh Kincaid, Lauren Miller, Hutch Peter, Jose Nazario, Tyler Woodard, Ryan Garcia, Tyler Poon and Tyler Rowden as each person has contributed toward this work.

Lastly, I would like to thank all my friends and family for providing support throughout this journey. This would not of been possible without them. To my wife, Natali, thank you for everything.

"Success is not final, failure is not fatal: it is the courage to continue that counts."

– Winston Churchill

Abstract

Development of an aluminum metal-metal multi-material (MM) is achieved through robotic wire arc additive manufacturing (WAAM) and additive friction stir deposition (AFSD). Using both additive processes enables the deposition of two distinct alloys to create one monolithic component. The interface formed by combining these two additive processes, represents an unexplored region. A comprehensive understanding of the microstructural characteristics and mechanical behavior is necessary to evaluate its influence on the performance of the bimetallic interface.

AFSD is a solid-state additive manufacturing (AM) process that plastically deforms the feedstock material, enabling deposition layer-by-layer. Robotic WAAM uses a gas metal arc welding (GMAW) torch, attached to the end effector of a robotic mechanism, to fuse material together, layer-by-layer. AFSD has higher deposition rates and can deposit alloys that are traditionally known as unweldable, specifically aluminum alloy 6061, which is prone to solidification cracking. Current AFSD machines are limited to 3-axis deposition, which limits capabilities within the printing process. Robotic WAAM has multi-axis deposition capabilities but must use aluminum filler wire, such as aluminum alloy 4943, that is less susceptible to solidification cracking. Printing with AFSD and WAAM sequentially, facilitates printing of complex geometries, where material versatility and deposition capability can be utilized from both AM processes. The resulting deposits are composed of multiple materials with discrete interfaces. Using AFSD, Al6061 is deposited, subsequently, WAAM Al4943 is deposited on the AFSD surface with varying

orientations. The AFSD Al6061 and WAAM Al4943 interface is investigated through metallographic analysis in conjunction with mechanical testing. Results are then compared to the parent alloys as well as a wrought Al6061-T6 counterpart.

Al6061 deposited via AFSD and Al4943 WAAM both exhibited an overaging effect in the as-deposited (AD) condition. This is attributed to the repeated thermal cycles during the deposition processes. Strengthening precipitates coarsen, diminishing the deposited material's mechanical performance. The discrete interface demonstrated superior mechanical performance compared to the weaker parent alloys, the AFSD Al6061. Under post T6 heat treatment, both alloys exhibited homogeneity, allowing strengthening mechanisms to develop, resulting in improved mechanical properties. Uniformity along the interface region was also observed, where the mechanical performance exceeded the Al6061 AFSD region. Characterization of the interface in both the as-deposited and heat treatment conditions, indicate that this region will not initiate failure, proved by its sufficient structural integrity. Such performance suggests the further use of aluminum MM developed through sequential AM of AFSD and WAAM without failure at the interface.

Table of Contents

1 Introduction **1**

1.1 Background 1

1.2 Motivation 1

1.3 Objective 2

2 Literature Review **4**

2.1 Additive manufacturing 4

2.1.1 Overview of additive manufacturing 4

2.1.2 Metal additive manufacturing 4

2.2 Aluminum 6061 5

2.2.1 Overview of wrought aluminum 6061 5

2.2.2 Heat treatment of aluminum 6061 6

2.2.3 Additive manufacturing of aluminum 6061 7

2.3 Additive friction stir deposition 9

2.3.1 Overview of additive friction stir deposition 9

2.3.2 Path planning for additive friction stir deposition 12

2.3.3 Additive friction stir deposition of aluminum alloy 6061 15

2.4 Aluminum 4943 19

2.4.1 Overview of aluminum 4943 19

2.5 Gas metal arc welding 20

2.5.1 Overview of gas metal arc welding 20

2.5.2 Gas metal arc welding of aluminum . . . 22
2.5.3 Gas metal arc welding of aluminum 4043 . . . 24
2.5.4 Gas metal arc welding of aluminum 4943 . . . 26
2.6 Wire arc additive manufacturing . . . 27
2.6.1 Overview of robotic wire arc additive manufacturing . . . 27
2.6.2 Cold metal transfer . . . 29
2.6.3 Wire arc additive manufacturing of aluminum 4943 . . . 29
2.6.4 Wire arc additive manufacturing using 4XXX and 5XXX series aluminum . . . 31
2.6.5 Aluminum WAAM and substrate interface . . . 31
2.7 Metal-metal multi-materials . . . 34
2.7.1 Overview of multi-materials . . . 34
2.7.2 WAAM of multi-materials . . . 35

3 Materials and Methods 39
3.1 Overview of multi-material deposits . . . 39
3.2 AFSD of aluminum 6061 . . . 39
3.2.1 AFSD process parameters . . . 39
3.2.2 Single-track Al6061 AFSD walls . . . 41
3.2.3 Dual-track AFSD walls . . . 44
3.3 WAAM of aluminum 4943 . . . 46
3.3.1 WAAM process parameters . . . 46
3.3.2 WAAM walls . . . 46
3.3.3 WAAM only build variations . . . 50
3.4 Al6061-Al4943 multi-material builds . . . 50
3.4.1 Multi-material builds . . . 50
3.4.2 Dual-track multi-material build variations . . . 51
3.5 Deposited builds . . . 54
3.5.1 Overview of deposited builds . . . 54

3.6 Heat treatment of deposits . . . 54
3.6.1 T6 heat treatment . . . 54
3.7 Sample Extraction . . . 57
3.7.1 Single alloy microindentation hardness sample extraction . . . 57
3.7.2 Single-track multi-material sample extraction . . . 57
3.7.3 Dual-track multi-material sample extraction . . . 59
3.8 Metallography . . . 62
3.8.1 Metallography sample preparation . . . 62
3.8.2 Optical microscopy . . . 62
3.8.3 Scanning electron microscopy . . . 64
3.9 Mechanical testing . . . 64
3.9.1 Tensile testing . . . 64
3.9.2 Microindentation hardness mapping . . . 64
3.10 Fractography . . . 66
3.10.1 Fracture analysis of tensile specimens . . . 66

4 Results and Discussion **68**
4.1 Surface roughness results . . . 68
4.2 Metallography results . . . 70
4.2.1 Optical microscopy results . . . 70
4.2.2 Scanning electron microscopy results . . . 79
4.3 Mechanical testing results . . . 88
4.3.1 Microindentation hardness results . . . 88
4.3.2 Parent alloy microindentation hardness results . . . 89
4.3.3 Multi-material microindentation hardness results . . . 91
4.3.4 Tensile testing results . . . 100
4.3.5 Parent alloy tensile testing results . . . 100
4.3.6 Multi-material tensile testing results . . . 106
4.3.7 Modified tensile testing results . . . 116

4.3.8 Fractography results 117

5 Conclusions and Future Work **128**

5.1 Conclusions 128

5.2 Future work 130

Bibliography **131**

A Figures and Tables **141**

A.1 Literature review 141

A.2 Materials and methods 143

A.2.1 Heat treatment certification 143

A.2.2 Sample Extraction 146

A.3 Results and Discussion 149

A.3.1 Surface Roughness 149

A.3.2 Optical Microscopy 151

A.3.3 SEM 158

A.3.4 Microindentation hardness testing 160

A.3.5 Tensile testing 167

A.3.6 Fractography 177

Vita **186**

List of Tables

2.1 Chemical composition of wrought aluminum alloy 6061 (1). 6

2.2 Temper designation and relating mechanical properties of aluminum alloy 6061 (1; 2; 3; 4; 5). 8

2.3 Chemical composition of aluminum alloy 4043 and 4943 (6; 7). 21

2.4 Tensile properties of Al4043 and Al4943 in the expected as-welded and observed as-deposited conditions. 30

2.5 As-deposited properties of Al4043 walls deposited via WAAM. 32

3.1 Process parameters used during single-track and dual-track AFSD of Al6061. 43

3.2 Process parameters used during WAAM of Al4943. 47

4.1 Average surface roughness of each Al6061 surface before Al4943 deposition. 69

4.2 Yield Strength of Al6061 AFSD and Al4943 WAAM under AD and HT conditions. 104

4.3 Ultimate Tensile Strength of Al6061 AFSD and Al4943 WAAM under AD and HT conditions. 104

4.4 Total elongation at fracture of Al6061 AFSD and Al4943 WAAM under AD and HT conditions. 104

4.5 Comparison of the calculated YS and UTS values derived from the hardness data and the measured YS and UTS. 105

4.6 Mechanical strength of the modified tensile specimens compared to the parent alloys. 119

A.1 Average microindentation hardness for each parent alloy in the AD and HT condition. 162

A.2 Yield Strength of Al6061 AFSD, Al4943 WAAM, and interfaces under AD and HT conditions. 172

A.3 Ultimate Tensile Strength of Al6061 AFSD, Al4943 WAAM, and interfaces under AD and HT conditions. 173

A.4 Total elongation at fracture of Al6061 AFSD, Al4943 WAAM, and interfaces under AD and HT conditions. 174

List of Figures

1.1 Schematic showcasing a cross section of an Al6061 AFSD and Al4943 WAAM bimetallic. 3

2.1 Diagram of the AFSD process (8). 11
2.2 An AFSD tool with teardrop-like protrusions on the tool face (9). . . 11
2.3 Schematic of the advancing and retreating side of an AFSD deposit (10). 14
2.4 Etched cross sections of various bead overlap conditions of Al7075 deposited using AFSD (11). 16
2.5 Hardness profile of a sectioned Al6061 build in the AD condition (12). 18
2.6 Tensile strength of aluminum 4043 and 4943 (13). 21
2.7 Schematic of the GMAW process (14). 23
2.8 Hardness profile of the HAZ for Al6061-T4 and Al6061-T6 base materials in the as-welded (AW) and postweld aged (PWA) conditions (15). 25
2.9 Microindentation hardness of Al4943 and other aluminum alloy welded joints (16). 28
2.10 Tensile strength of Al4943 and other aluminum alloy welded joints (16). 28
2.11 Grain structure of an Al4043 thick wall WAAM deposit. (17). 33
2.12 Cross sections of the WAAM and FS interface before and after etching (18). 36
2.13 Hardness profile across the WAAM and FS interface (18). 37
2.14 SEM images of the mild steel and silicon bronze WAAM interface (19). 37

3.1 All printed build orientations. 40
3.2 Schematic of the MELD L3 machine. 42
3.3 Graphical representation of a single-track Al6061 AFSD wall. 45
3.4 Graphical representation of a dual-track Al6061 AFSD wall. 45
3.5 Schematic of the AML3D Arcemy WAAM cell. 48
3.6 First layer path plan for an Al4943 WAAM wall using WAMsoft. . . . 49
3.7 Graphical representation of an Al4943 wall deposited via WAAM. . . 49
3.8 Graphical representation of an Al6061-Al4943 multi-material with Al4943 deposited on the top surface of a single-track Al6061 wall. . . 52
3.9 Graphical representation of an Al6061-Al4943 multi-material with Al4943 deposited on the side surface of a single-track Al6061 wall. . . 52
3.10 Graphical representation of an Al6061-Al4943 multi-material with Al4943 deposited on the top surface of a dual-track Al6061 wall. . . . 53
3.11 Different build orientations after deposition. 55
3.12 A halved multi-material build consisting of a single-track Al6061 AFSD with Al4943 deposited via WAAM on the top AD AFSD surface. . . . 56
3.13 Extraction site of a microindentation hardness sample from an Al6061 AFSD single-track wall. 58
3.14 Sample extraction from the halved Al4943 deposited on the AD Al6061 AFSD surface wall. 60
3.15 Sample extraction from Al4943 deposited on the Al6061 machined top surface wall. 61
3.16 Sample extraction from the Al4943 deposited on the Al6061 machined side surface wall. 61
3.17 Extraction site of a microindentation hardness sample from an Al4943 deposited on the Al6061 AFSD dual-track wall. 63
3.18 Hardness mapping across single-track AFSD 60 mm long samples using a 117 x 5 grid. 67

3.19 Hardness mapping across dual-track AFSD 60 mm long samples using a 60 x 13 grid. 67

4.1 Etched Al6061 deposited via AFSD in the AD condition. 71
4.2 Grain size within the AD Al6061 deposited via AFSD, measuring approximately 5 - 10 μm. 71
4.3 Grain structure of a bead overlap region from an Al4943 WAAM deposit in the AD condition. 73
4.4 Higher magnification of the grain structure of Al4943 deposited via WAAM in the AD condition. 73
4.5 HAZ into the AD Al6061 AFSD from the Al4943 WAAM. 74
4.6 Grain structure near the Al6061-Al4943 interface in the AD condition. 74
4.7 Grain structure of an Al6061 AFSD deposit in the HT condition. . . 76
4.8 Grain structure of an Al4943 WAAM deposit in the HT condition. . . 77
4.9 Grain structure near the Al6061-Al4943 interface in the HT condition. 78
4.10 Grain structure near the Al6061-Al4943 interface in the HT condition at 300x magnification. 78
4.11 SEM with EDS images of Al6061 material deposited via AFSD where iron-rich intermetallics are present. 81
4.12 SEM with EDS images of Al4943 material deposited via WAAM where high concentrations of silicon are located at the grain boundaries. . . 82
4.13 SEM with EDS images of Al6061-Al4943 interface deposited via AFSD and WAAM. 83
4.14 SEM with EDS images of Al6061 deposited via AFSD post HT process. 85
4.15 SEM with EDS images of Al4943 deposited via WAAM post HT process. 86
4.16 SEM with EDS images of Al6061-Al4943 interface deposited via AFSD and WAAM post HT process. 87
4.17 Microindentation hardness across single-track and dual-track AD and HT Al6061 AFSD samples. 90

4.18 Microindentation hardness across an AD and HT Al4943 WAAM sample. 92
4.19 Microindentation hardness profile across the AD Al6061-Al4943 interface. 94
4.20 Microindentation hardness within the AD Al6061 AFSD, Al6061-Al4943 interface and Al4943 WAAM samples. 95
4.21 Microindentation hardness within the HT Al6061 AFSD, Al6061-Al4943 interface and Al4943 WAAM samples. 96
4.22 Average microindentation hardness across all single-track MM deposits with various conditions. 98
4.23 Average microindentation hardness across all dual-track MM deposits with various conditions. 99
4.24 Engineering stress-strain curves for the AD and HT condition of Al6061 deposited via AFSD. 102
4.25 Engineering stress-strain curves for the AD and HT condition of Al4943 deposited via WAAM. 103
4.26 Engineering stress-strain curves for the AD and HT condition of the Al6061-Al4943 interface for Al4943 deposited on the Al6061 AFSD AD top surface. 107
4.27 Engineering stress-strain curves for the AD and HT condition of the AD and machined Al6061-Al4943 interface. 109
4.28 Engineering stress-strain curves for the AD and HT condition of the Al6061-Al4943 interface along the machcined side of the Al6061 AFSD deposit. 111
4.29 Yield strength of each print orientation in the AD and HT condition. 113
4.30 Ultimate tensile strength of each print orientation in the AD and HT condition. 114
4.31 Total elongation of each print orientation in the AD and HT condition. 115
4.32 Engineering stress-strain curves for the AD and HT conditions of the modified tensile specimens. 118
4.33 Fracture surface in the AD condition of Al6061 deposited via AFSD. 121

4.34 Fracture surface in the HT condition of Al6061 deposited via AFSD. . 121
4.35 Fracture surface in the AD condition of Al4943 deposited via WAAM. 123
4.36 Fracture surface in the HT condition of Al4943 deposited via WAAM. 123
4.37 Fracture surface in the AD condition of the interface, where Al4943 was deposited on the AFSD AD top surface. 125
4.38 Fracture surface in the HT condition of the interface, where Al4943 was deposited on the AFSD AD top surface. 125
4.39 Fracture surface in the AD condition of the interface, where Al4943 was deposited on the machined AFSD side surface. 127
4.40 Fracture surface in the HT condition of the interface, where Al4943 was deposited on the machined AFSD side surface. 127

A.1 Cross section of a starting location of an AFSD deposit with the uncertainty zone along the edges of the build (12). 142
A.2 Temperature vs time during the solution and quenching steps of the heat treatment T6 process. 144
A.3 Temperature vs time during the artificial aging step of the heat treatment T6 process. 145
A.4 Extraction site of microindentation hardness sample from an Al6061 AFSD dual-track wall. 147
A.5 Extraction site of microindentation hardness sample from an Al4943 WAAM wall. 148
A.6 Surface roughness from the Al6061 AFSD AD top surface. 150
A.7 Stitched image of the etched Al6061 deposited via AFSD in the AD condition. 152
A.8 Grain structure of Al4943 material deposited via WAAM in the AD condition. 153
A.9 Stitched image of the etched Al4943 deposited via WAAM in the AD condition. 154

A.10 Stitched image of the etched Al6061-Al4943 interface deposited in the AD condition. 155
A.11 Stitched image of the etched Al6061 deposited via AFSD in the HT condition. 156
A.12 Stitched image of the etched Al4943 deposited via WAAM in the HT condition. 157
A.13 Iron rich intermetallic found during SEM with EDS of Al6061 deposited via AFSD post HT process. 159
A.14 Microindentation hardness across an AD Al4943 WAAM sample. . . . 161
A.15 Average microindentation hardness with two standard deviation across all MM deposits with various conditions. 163
A.16 Average microindentation hardness with two standard deviation across all dual-track MM deposits with various conditions. 164
A.17 Average microindentation hardness across all MM deposits with various conditions. 165
A.18 Average microindentation hardness with two standard deviation across all MM deposits with various conditions. 166
A.19 Miniature tensile specimen dimensions used for tensile testing. 168
A.20 Modified tensile specimen dimensions used for tensile testing. 169
A.21 Tensile grips used during tensile testing of the miniature tensile specimens. 170
A.22 Engineering stress-strain curves for the AD condition of Al6061 deposited via AFSD containing an outlier. 171
A.23 Yield strength of the modified tensile specimens compared to the parent alloys. 175
A.24 Ultimate tensile strength of the modified tensile specimens compared to the parent alloys. 176
A.25 Higher magnification of the fracture surface in the AD condition of Al6061 deposited via AFSD. 178

A.26 Fracture surface in the HT condition of Al4943 deposited via WAAM where porosity is observed. 179
A.27 Fracture location of the Al4943 WAAM deposited on the AD AFSD top surface when in the AD condition. 180
A.28 Fracture location of the Al4943 WAAM deposited on the AD AFSD top surface when in the HT condition. 181
A.29 Fracture location of the Al4943 WAAM deposited on the machined AFSD side surface when in the AD condition. 182
A.30 Fracture location of the Al4943 WAAM deposited on the machined AFSD side surface when in the HT condition. 183
A.31 Fracture location of the modified specimens when in the AD condition. 184
A.32 Fracture location of the modified specimens when in the HT condition. 185

Chapter 1

Introduction

1.1 Background

The work herein uses two different metal additive manufacturing (AM) methods to print a metal-metal multi-material. Additive friction stir deposition (AFSD) and wire arc additive manufacturing (WAAM) are used sequentially to achieve a multi-material wall geometry. Using AFSD, Al6061 is deposited and then using WAAM, Al4943 is deposited on the AFSD surface. This creates a discrete bimetallic interface where the two aluminum alloys meet. AFSD and WAAM are both metal AM methods that are being leveraged to create the monolithic multi-material.

1.2 Motivation

Although not a replacement, metal AM serves as a supplement to traditional manufacturing methods, such as casting and forging. A lack of infrastructure for large castings and lengthy lead times from foreign sourcing, prompts alternative solutions for manufacturing large components in the United States (US) (20). AFSD and WAAM provide large build volumes, high deposition rates, and relatively low upfront costs, making large-scale component production ideal. These metal AM methods drive US production and complement the deficiencies of traditional manufacturing

methods. Developing a metal-metal multi-material part using both AFSD and WAAM showcases the freedom within AM. A tailored manufacturing plan can provide localized target material properties utilizing the two AM methods. AFSD offers higher deposition rates that reach approximately 13.6 kg/hr for aluminum alloys (21), while also having the ability to deposit Al6061 with enhanced mechanical properties. Robotic WAAM has multi-axis printing capability of Al4943 with a higher printing fidelity. Using their advantages, a large-scale component can consist of multiple materials while retaining a near-net shape profile. Other metal alloys can potentially be used to create unique multi-material components utilizing these metal AM methods.

1.3 Objective

This research presents a novel approach to manufacture a bimetallic wall consisting of Al6061 deposited via AFSD and Al4943 deposited via WAAM. A discrete interface of unknown material characteristics distinguishes the two materials. The Al6061 and Al4943 interface must be evaluated to determine its bond quality for future deployment of such components. The interface is characterized, tested and compared to its wrought counterpart. The influence of the deposition surface roughness, orientation, and post-process heat treatment conditions on the bimetallic is evaluated. Figure 1.1 presents a representative example of the Al6061-Al4943 multi-material.

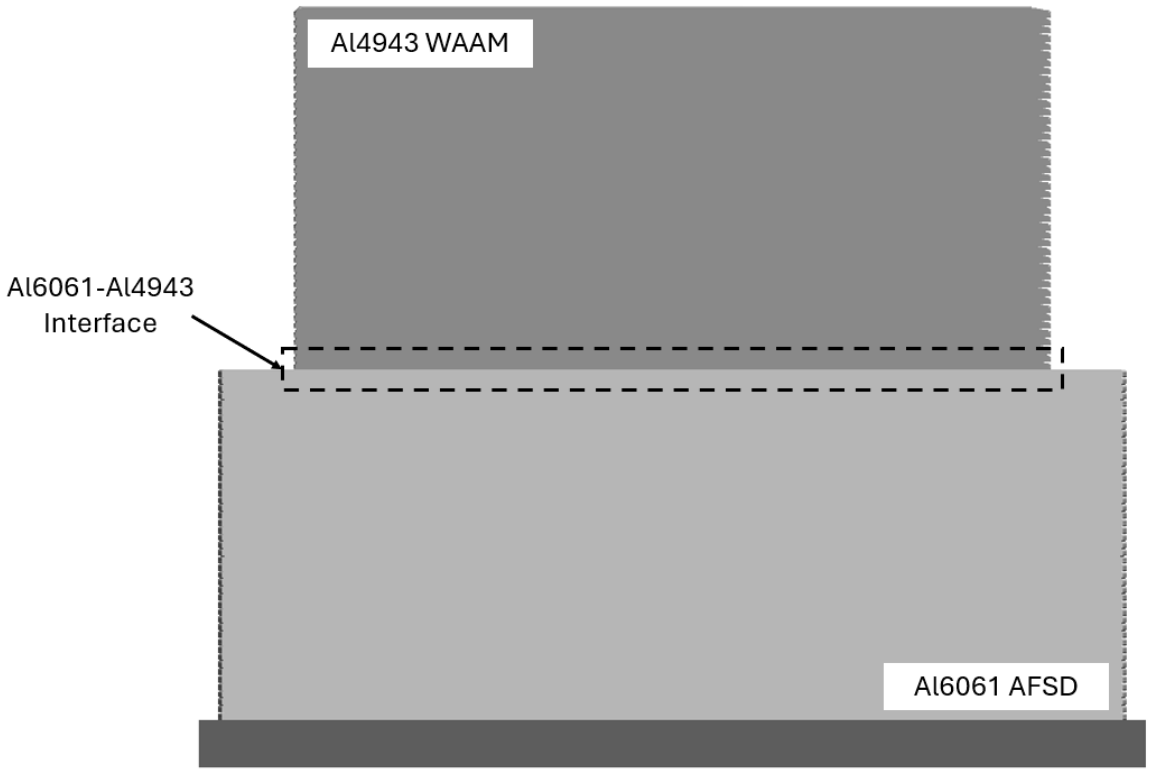


Figure 1.1: Schematic showcasing a cross section of an Al6061 AFSD and Al4943 WAAM bimetallic.

Chapter 2

Literature Review

2.1 Additive manufacturing

2.1.1 Overview of additive manufacturing

AM is the process of joining material in a layer-by-layer method to create 3-dimensional parts (22). Computer aided design (CAD) models are sliced into 2-dimensional cross sections and printing path plans are generated for each slice. The AM machine follows the planned path for each layer, while depositing material to 3D print a component. AM can be used to print complex near-net shape geometries to reduce material waste (23). Different AM processes have advantages and disadvantages that can be leveraged depending on the desired print qualities. Desired material, material properties, deposition rate, print complexity and build volume all dictate the optimal AM process to be used.

2.1.2 Metal additive manufacturing

There are many metal additive manufacturing (MAM) technologies that are currently being used. Directed energy deposition (DED) and powder bed fusion (PBF) are MAM fusion-based processes. They both use an energy source to create a melt pool

that incorporates the substrate and wire or powder feedstock. Melt pool mixing enables fusion of the newly deposited layer. These are layer-by-layer processes that promote localized melting of material by the energy source while following a planned trajectory based on a CAD model (24). The melt pool material solidifies, enabling deposition of each layer. Both DED and PBF have a wide range of material deposition capabilities but certain materials remain incompatible due to the fusion-based nature of the processes.

Solid-state AM is a MAM process that deposits material without melting. Operating below the melting temperature, material is plastically deformed and bonded to the substrate. Deposition is achieved and repeated layer-by-layer to 3D print metal components. AFSD and cold spray additive manufacturing (CSAM) are solid-state AM techniques that follow these principles. Due to the nature of solid-state deformation based processes many material systems which are prone to solidification cracking, such as 6xxx series aluminum, may be deposited.

Aerospace and marine industries desire metal alloys that are lightweight, have high strength and are corrosion resistant (25; 26; 27). Using traditional manufacturing methods for larger components tend to have lengthy lead times and are costly. With the freedoms of metal AM, desired material properties can be met, and complex geometries can be printed.

2.2 Aluminum 6061

2.2.1 Overview of wrought aluminum 6061

Aluminum alloy 6061 is a heat treatable wrought alloy that is mechanically worked into sheet, plate or extrusion from a cast billet. The elemental composition of the Al6061 can be seen in table 2.1. 6xxx series aluminum is primarily an Al-Mg-Si system, where magnesium and silicon are the principal alloying elements. These enable the formation of magnesium silicide (Mg_2Si) precipitates, otherwise known as

Table 2.1: Chemical composition of wrought aluminum alloy 6061 (1).

Aluminum Alloy	Si	Fe	Cu	Mn	Mg	Zn	Other	Al
6061	0.40-0.8	0.7	0.15-0.40	0.15	0.8-1.2	0.25	0.04-0.35Cr	Bal

the beta phase, β, during heat treatment (1). Various β phases are present depending on the aging but overall they act as a strengthening mechanism for Al6061. Being a lightweight material with good mechanical properties, corrosion resistance, and weldability makes Al6061 highly sought after. It is a general-purpose aluminum alloy that is heavily used in the aerospace and automotive industries.

2.2.2 Heat treatment of aluminum 6061

Aluminum 6061 strengthens once heat treated to a desired temper designation. Heat treatment of metals enable microstructural changes without altering the component's geometry. Thermal processing is imposed on the component by a heating element for a specified amount of time. For aluminum alloys, this process is made up of a solution treatment, quenching, and an artificial aging.

Solution treating reaches temperatures above recrystallization producing a complete dissolution of the solute. This is followed with a quenching step to rapidly cool the component. The part is submerged in water until a thermal steady state is established. A supersaturated solid solution is retained, where precipitates can not form. Magnesium and silicon are trapped in the supersaturated solid solution known as the aluminum matrix (α-Al). Lastly, artificial aging of the component, also known as precipitation hardening, is imposed by elevating the temperature for a specified amount of time to control precipitation of the β phase (4). During the aging process, as time duration increases, solute atom clusters form, where they then evolve into Guinier-Preston (GP) zones. Beta double prime (β") forms next, with

beta prime (β') and β following (4). The desired β phase can be achieved through alteration of the heat treatment schedule. The precipitation hardening enhances the mechanical properties through the formation of fine precipitates which impede dislocation motion. Heat treatment schedules can be altered to achieve a desired microstructure with relating mechanical properties. This creates varied alloys that are assigned to a temper designation. Temper designations can be mechanical and/or thermal treatments that are used to produce varied alloys. For this thesis, only thermal treatments will be evaluated. Table 2.2 summarizes the different temper designations and their resulting mechanical properties.

2.2.3 Additive manufacturing of aluminum 6061

Components made from Al6061 are traditionally formed or post-machined from a wrought workpiece, as challenges exist associated with its deposition via AM. Fusion processes require melting and solidification of the deposition material. Some aluminum alloys, like Al6061 are prone to solidification cracking. As the melt pool cools, it begins to solidify and contract due to the thermal expansion coefficient. Surrounding the melt pool is the mushy zone that consists of a mixture of liquid and solid material. The solid material undergoes thermal contraction, while the liquid material does not. The difference in thermal contraction introduces tensile stresses at the solid-liquid interface. High stresses can prevent full melt pool flow, leading to underfeeding of material in shrunk locations that drives cracking during solidification (28; 29). This makes usage of fusion techniques unachievable without modifying the alloy composition.

Laser melting has been used to deposit a modified composition of Al6061. Mehta et al. (30) printed using an Al6061 composition that added 1 wt% zirconium (Zr) to the powder feedstock and compared to an unmodified Al6061 deposit. Cracks were found in the unmodified builds while the Zr modified Al6061 was crack free. Rosito et al. (31) printed using a reactive additive manufacturing (RAM) Al6061

Table 2.2: Temper designation and relating mechanical properties of aluminum alloy 6061 (1; 2; 3; 4; 5).

Temper designation	**Temper description**	**Heat treatment schedule**	**Strengthening mechanism**	**UTS (MPa)**	**YS (MPa)**	**Elongation (%)**	**Hardness (HV)**
O	Annealed	Heat to 415°C for 2 to 3 hours, then cool at a rate of 30°C/h until reaching 260°C	Recrystallized grain structure without precipitates	125	55	25	32
T4	Solution heat treated and then naturally aged	Heat to 529°C for 8 hours, quench in water reaching 43°C max, age at room temperature for about 96 hours	Guinier-Preston (GP) clusters form (pre-β")	240	145	22	74
T6	Solution heat treated and then artificially aged	Heat to 529°C for 8 hours, quench in water reaching 43°C max, age at 177°C for 8 hours	Precipitation of fine needle like shaped β" phase	310	275	12	111

powder that included reactive titanium (Ti) and boron carbide (B_4C) powders. This created in situ chemical reactions forming ceramic reinforcement, resulting in crack free parts. Fedotowsky et al. (32) was able to deposit crack free samples using laser power directed energy deposition (LP-DED) with Al6061-RAM2 wire.

Without modification of the Al6061 composition, fusion based AM techniques are unable to deposit this alloy. Solid-state AM processes enable deposition of Al6061 without composition modification. Deposition is achieved because there is no melting, which prevents solidification. AFSD and cold spray additive manufacturing are two commercialized solid-state AM techniques that deposit Al6061. Both utilize plastic deformation of a feedstock to deposit material, layer-by-layer. They have the capability to achieve fully dense components with enhanced mechanical properties (33; 34; 35). AFSD of Al6061 has high deposition rates with grain refinement from the feedstock as severe plastic deformation creates fine equiaxed grains (35; 36). Mechanical properties are comparable to wrought properties, making this AM technique sought after.

2.3 Additive friction stir deposition

2.3.1 Overview of additive friction stir deposition

AFSD is a solid-state AM process that utilizes frictional heating and stirring to deposit material. A consumable material feedstock rotates with a non-consumable tool head at a specified spindle speed (Ω), spindle torque, or temperature and is forced onto a substrate at a specified material feed rate (MFR). Deposition is possible, as a commanded path is followed while the rotating feedstock is forced onto the stationary substrate causing frictional heating (37). Increased feedstock and substrate temperatures soften the feedstock material, resulting in plastic material flow (38). The plastically deformed material mixes with the substrate or previously deposited layers, enabling bonding of the layers to create a solid metallic structure, layer-by-layer.

There are different methods that alter the feedstock or tool head configuration. Powder, wire, and square or round rod feedstock can be used during the AFSD process with square rod feedstock being the most common. Tool head configurations consist of using the consumable feedstock as the tool or using a non-consumable tool to promote mixing of material. Using consumable feedstock rods as the tool is traditionally known as friction surfacing (FS) (39). A rotating round feedstock rod, acting as a tool, traverses across a stationary substrate while an axial force pushes the rod down against the substrate. This process generates frictional heat that results in hot working of the rod without reaching melting temperatures of the metal. Plasticization of the feedstock enables a solid-state deposition of material. Aluminum FS can be used to print components with a fine-grained microstructure of 4.2 to 4.6 μm and have mechanical properties comparable to its wrought counterpart (40; 41). This process tends to generate an excess amount of flash near the bottom of the feedstock. Using a rotating tool configuration promotes mixing of material that pushes any flash to the boundary of the deposit. MELD has developed a commercialized AFSD machine that uses a square rod feedstock with a rotating hollow square hole tool (42). The tool head is a non-consumable with teardrop-like protrusions on the tool face to assist with heat generation and mixing of material. The tool face is displaced by a desired layer height from the substrate in the build direction to provide a gap for material to flow. The tool face protrusions remain in contact with the substrate during the deposition. The feedstock rotates with the tool as it is forced down by an actuator onto the substrate. Frictional heat is generated from the feedstock and tool rotation on the substrate. The feedstock material is softened, and its flow stress is decreased to further facilitate plastic flow. A solid-state metallurgical bond between the deposited layer and substrate is achieved. Important process inputs that influence the flow of material are the spindle speed, traverse rate, and MFR.

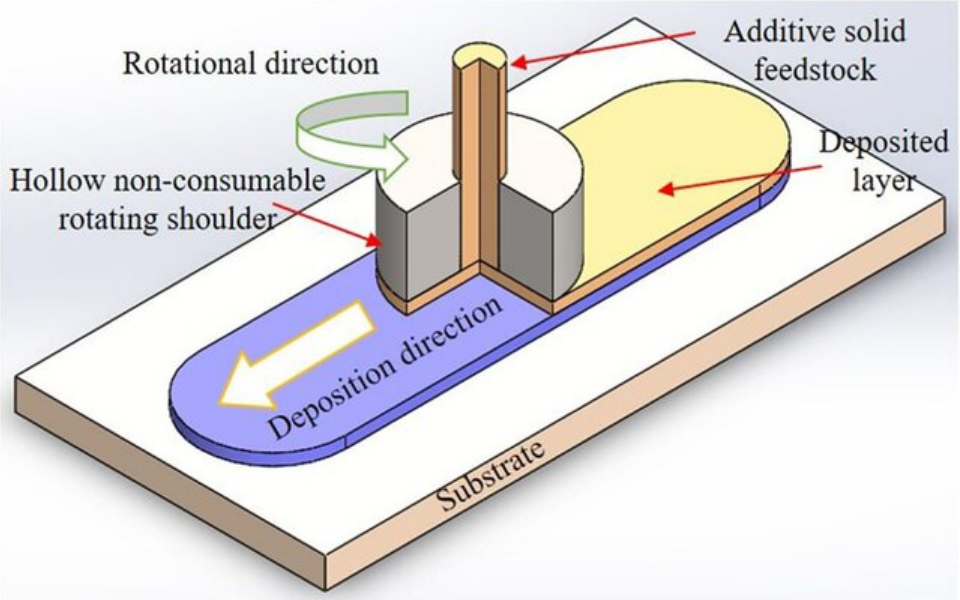


Figure 2.1: Diagram of the AFSD process (8).



Figure 2.2: An AFSD tool with teardrop-like protrusions on the tool face (9).

2.3.2 Path planning for additive friction stir deposition

Current AFSD machines are limited to 3-axis deposition which limits the near net shape capabilities and prevents multi-axis printing. This AM method has high deposition rates and enables large scale printing for simpler geometries (43; 44). When depositing Al6061, deposition rates reach 14.54 kg/h during stationary deposition experiments (45). AFSD specializes in printing material quickly but studies and information on bead overlap properties are limited. To deposit large fully dense components, multi-track builds must be used, and their properties need to be better understood.

Single track AFSD builds dominate current research. Deposit morphology is dictated by the process parameters and the specified layer height, usually 1 to 2 mm. As material is forced onto the substrate, excess material is forced to the edges of the track extending out radially past the tool. This creates an area of uncertainty as forces are lower due to lack of contact with the tool face. Defects reside along the edges of a build due to lack of tool pressure. Defects include a kissing bond, where layers are not metallurgically bonded but rather contacting each other, tunnel defects, which are voids within the material and flash, which is over-displaced material beyond the track width. It is recommended to machine away the edges of the deposited material until the remaining surface is positioned 2 mm inside the AFSD tool's radius (12). This ensures defect-free material that has been deposited in a steady state manner. An AFSD cross sectioned deposit shows these defects in appendix A.1. During deposition an advancing and retreating side is created in the deposit where microstructure and mechanical properties vary between the two. The advancing side occurs when the tangential velocity of the rotating tool and traverse direction are aligned. The retreating side occurs when the tangential velocity of the rotating tool and traverse direction are opposing in direction. Metz et al. (10) found that when depositing Al6061, the advancing side had larger grain sizes at roughly 15 μm whereas the retreating side was about 6 μm. The center of the build was about 16 μm. Spatial

variations of properties are found due to the variations in strain and temperature during deposition. Temperature during deposition is dictated by the spindle speed and traverse rate used during deposition. Process parameters drive mechanical and microstructural properties within the build. Higher feed rates and rotational speeds lead to larger grain sizes due to increased deposition temperatures (46).

Little research has been completed on the bead overlap properties in multi-track builds. Phillips et al. (47) printed a dual-track Al6061 wall following an alternating raster pattern that successfully bonded the overlapping passes. A minimum material flow rate was determined during the overlap pass to ensure adequate material fill was achieved. A reduction in Vickers hardness of roughly 15 HV was measured at the center of the bead overlap compared to the bulk deposit. Repeated thermal cycles from the overlapping passes dissolve strengthening precipitates, reducing the hardness. The tensile strength at the bead overlap increased when compared to the single track build but exhibited lower mechanical strength than the feedstock material. Li et al. (48) explored the influence of the width of the bead overlap in AFSD when cladding an Al6061-T651 feedstock on a 316 stainless steel substrate. A single-track deposit showed a lack of metallurgical bonding at the substrate interface while the bead overlap deposits exhibited improved bond integrity. As the bead overlap width increased, thermal input increased, resulting in reduced hardness and coarser grains. A bead overlap deposit improves bonding because temperatures increase but mechanical properties degrade. Cahalan et al. (11) studied the effects of the bead overlap width ranging on Al7075 from -6.4 mm to 19.1 mm overlap. Using a 38.1 mm diameter tool, nine total builds were deposited, increasing the bead overlap by 3.2 mm per build. As the overlap conditions increased, the bonding integrity improved but an excess of overlap width contributes to increased material waste. An average grain size of approximately 4 μm was measured for all builds. The Vickers hardness ranged from 120 HV to 125 HV. An overlap width of at least 25% of the deposition width is recommended to achieve proper metallurgical bonding. For the tool used in this study, an overlap width of 6.35 mm to 9.53 mm is recommended to achieve proper

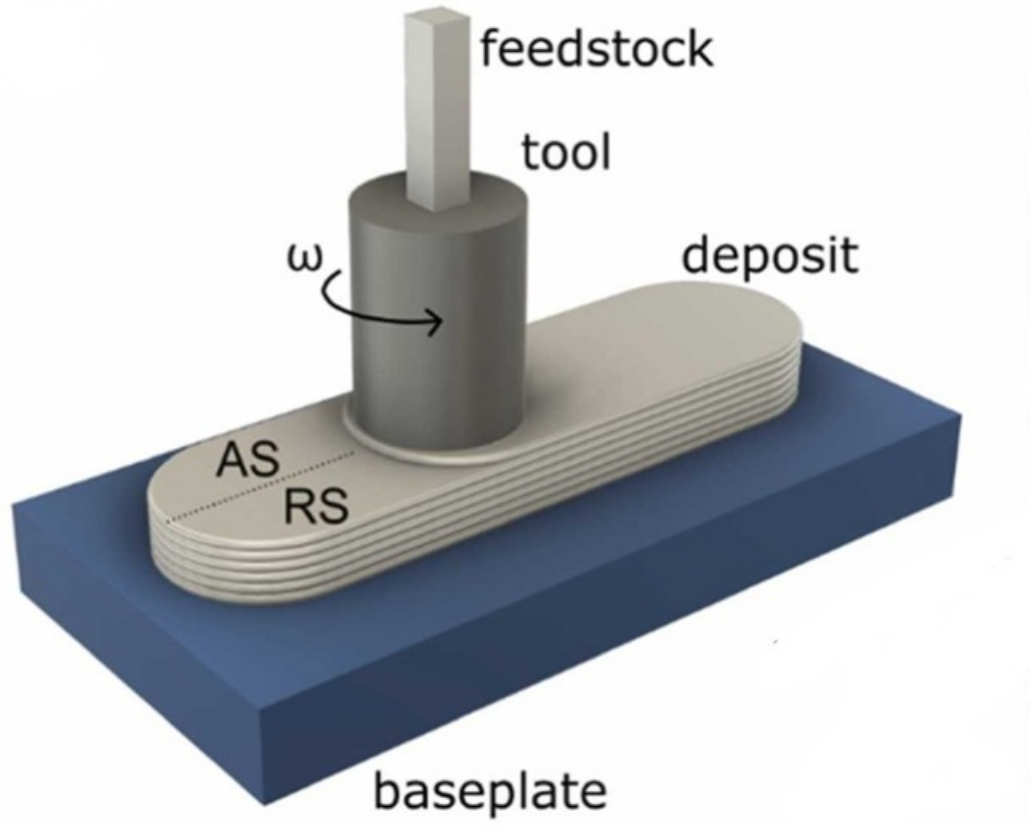


Figure 2.3: Schematic of the advancing and retreating side of an AFSD deposit (10).

bonding that produces the best mechanical properties while minimizing material waste. Kincaid et al. (49) evaluated path planning effects on bead overlaps when depositing Al6061. A predicted deposit width was calculated based on the MFR and traverse rate of the tool. This was used to create a bead overlap with minimal flash generation. Validation was proven through various multi-track builds where the print direction was altered by the advancing and retreating conditions. Minimal flash was generated when intermixing the advancing side of the second track into the retreating side of the first track.

AFSD is not restricted by solidification issues due to it being a solid-state process. This enables deposition of materials that are usually unable to be deposited with fusion processes, such as Al6061.

2.3.3 Additive friction stir deposition of aluminum alloy 6061

AM technologies that use solidification techniques often consider Al6061 to be unweldable, due to its susceptibility to solidification cracking. AFSD remains below the melting temperature during deposition, permitting the deposition of Al6061.

Evaluation of the precipitates within the material can be achieved by X-ray diffraction (XRD) and scanning electron microscopy (SEM) with energy dispersive spectroscopy (EDS). XRD is used to identify crystalline phases and estimate the phase compositions present. When combined with EDS, an SEM can be used to map the distribution of elements within a material. These are common material characterization techniques used in additive manufacturing.

Gao et al. (35) investigated the microstructure and mechanical properties in the as-deposited (AD) condition of AFSD using Al6061. Fine equiaxed grains are produced due to dynamic recrystallization. Continuous dynamic recrystallization is the evolution of grain morphology through misorientation without nucleation (50). This occurs during the AFSD process because of the hot working of material where dynamic recovery is significant. Aluminum alloys like Al6061 and Al7075 have

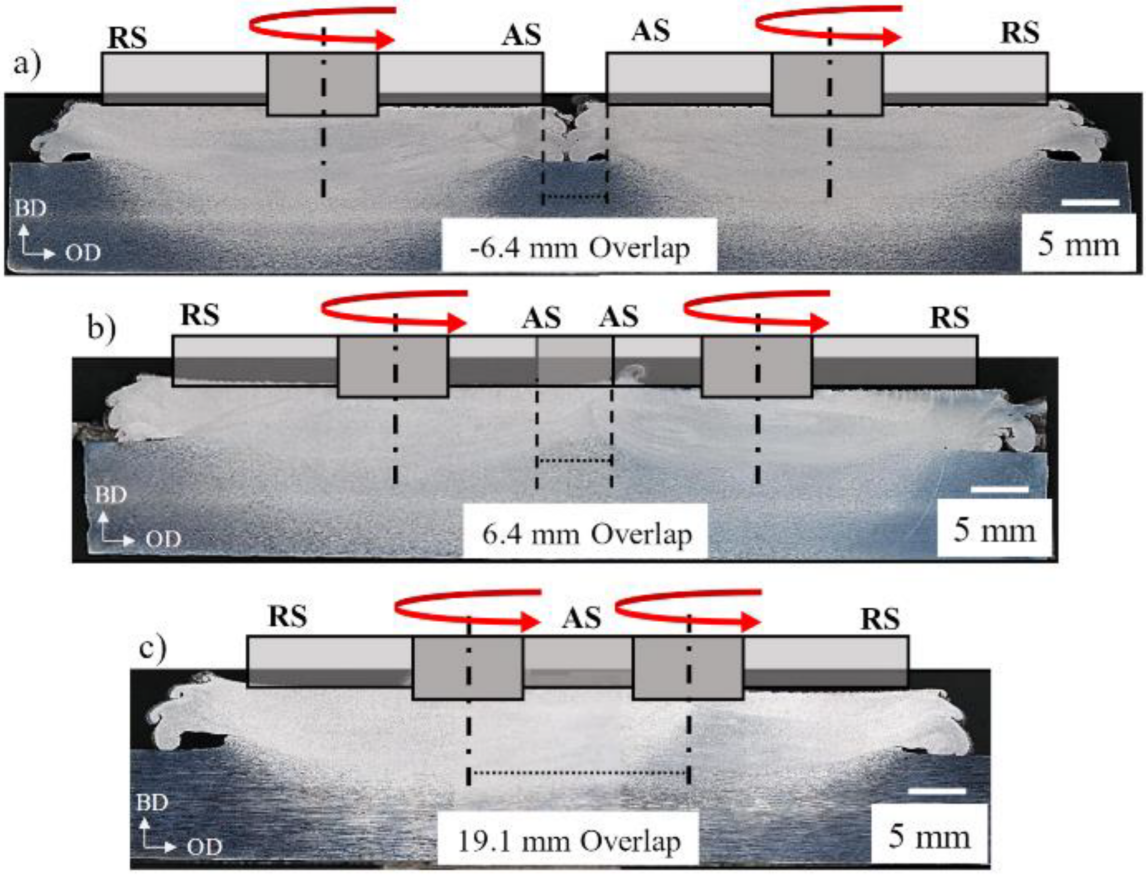


Figure 2.4: Etched cross sections of various bead overlap conditions of Al7075 deposited using AFSD (11).

high stacking fault energy (SFE) that favor reorientation of grains. The stirring causes severe plastic deformation leading to intense shear deformation at elevated temperatures, reorienting the grains into fine equiaxed grains. Electron back scatter diffraction (EBSD) revealed a grain size refinement from 200 μm in the feedstock to 15 μm in the deposit of Al6061 by Gao. While the grain size was reduced, a 20% reduction in Vickers hardness from the feedstock to the deposit was measured. The dissolution of the β strengthening precipitates during the deposition process is responsible for the decrease in hardness.

Post process heat treatment of AFSD builds enhance mechanical properties from the AD condition. The AD hardness and tensile strength tend to be less than the base material or heat treated builds. In the AD condition the average microindentation hardness is about 50 HV and in the T6 condition it is about 100 HV (51; 52). Hardness profiles in the AD condition revealed that closer to the top surface of the build the hardness increases where the top surface is the hardest. Repeated thermal input softens the material below and thus the top surface has not been exposed to such conditions, retaining the hardness (35; 52; 12). Heat treatment conditions have shown to provide realtively uniform hardness across the whole build.

Tensile properties of Al6061 deposited using AFSD can be improved with post process heat treatment as well. In the AD condition ultimate tensile strength (UTS) reaching up to 300 MPa has been reported (53). However, other studies have shown mixed results with anisotropic behavior. UTS values in the build direction reaching only about 135 MPa (35). In the heat treated condition, UTS values have reached 361 MPa (53). The precipitation of the β" phase during the heat treatment process strengthens the material, improving the mechanical properties. This is exemplified in the hardness and tensile strength.

In the AD condition XRD analysis of Al6061 prints, has proven that the precipitates dissolve back into the α-Al matrix due to the processing temperatures. Al6061-T6 base material have α-Al matrix peaks with secondary phases present. The AD AFSD builds show mostly α-Al peaks with minimal secondary phases. Post

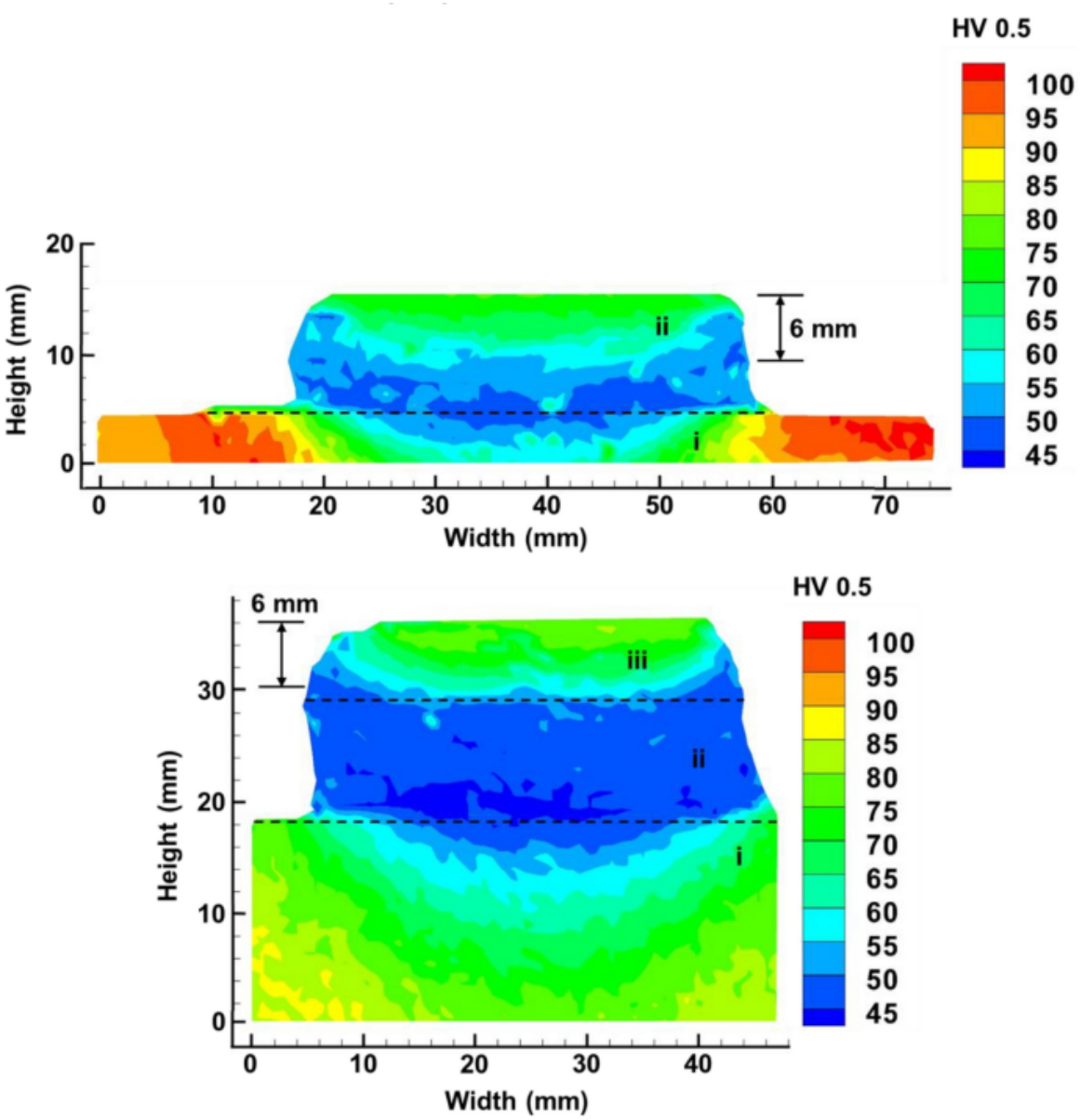


Figure 2.5: Hardness profile of a sectioned Al6061 build in the AD condition (12).

T6 heat treatment of the AFSD builds show changes in the peaks from the AD condition (53; 51). This formation of fine β" precipitates during the aging process prompt the changes in the peaks which has been confirmed by microscopy. SEM techniques have shown fine β" precipitates are absent in the AD builds but are present post heat treatment. An iron rich intermetallic is also present at times, β-Al_5FeSi phase (53; 35). Combining SEM with EDS provides insight into elemental composition within the deposit. The AD builds appear to have less Mg content than the base material or when in the heat treated condition due to the dissolution of the precipitates into the solid solution (51).

2.4 Aluminum 4943

2.4.1 Overview of aluminum 4943

Aluminum ER4943 was developed as a welding filler wire to join aluminum, specifically 6xxx series. Aluminum filler wires are formulated with higher amounts of silicon or magnesium that help prevent solidification cracking. Al4943 is not commercially available in wrought or cast forms but primarily as a welding wire.

Hobart Filler Metals first introduced the wire in 2012 showcasing the development of the alloy (54). Weld metal composition is primarily aluminum and silicon with some significance of iron and magnesium. The composition was based on ER4043 wire, but was modified to enable post-weld heat treat (PWHT) capabilities. The composition of ER4043 and ER4943 wires are shown in table 2.3. ER4943 filler wire has the capability to weld wrought 1xxx, 3xxx, some 5xxx, 6xxx, and A356 casting base metals. Important features during the welding process include minimal welding smut, low melting temperature with high melt pool fluidity and low shrinkage rates to prevent solidification cracking. Post weld features include moderate to high strength, moderate electrical conductivity, excellent corrosion resistance and the ability for heat treat and aging applications to improve mechanical properties (13). This alloy

is seen as a general-purpose filler wire to be used in automotive, aerospace and marine applications. Other common aluminum filler wires have similar properties and applications but lack the ability for PWHT including Al4043 and Al5356. As-welded properties of Al4043 are detailed in subsection 2.5.3 and WAAM properties are shown in subsection 2.6.4. As-welded and PWHT properties of Al4943 are detailed in subsection 2.5.4 and its WAAM properties are provided in subsection 2.6.3.

2.5 Gas metal arc welding

2.5.1 Overview of gas metal arc welding

Gas metal arc welding (GMAW), traditionally known as metal inert gas (MIG) welding is an arc welding process that enables the joining of metals through fusion. A consumable wire electrode is fed from a spool mounted on a power supply through a welding gun and towards the workpiece. A torch with a nozzle is mounted to the end of the welding gun where an electric arc, acting as the heat source, is established between the wire and workpiece, melting both materials in the process. A liquid metal pool is created, which is known as the melt pool. An inert shielding gas flows from the nozzle, protecting the melt pool from environmental gases, specifically oxygen and nitrogen. As the operator traverses the torch, localized heating creates the molten metal pool that subsequently cools and solidifies, fusing the weld metal to the workpiece (55; 14).

Welding parameters control the quality of the welded material. Process parameters include voltage and current that are input commands on the power supply. These control the amount of energy input into the system which affect the penetration depth of the weld. Travel speed is the velocity of the torch relative to the workpiece and wire feed rate is the velocity of the wire as it is being fed into the melt pool. These must be coupled together for a consistent bead geometry. The diameter of the wire coupled with the wire feed rate has a direct impact on the deposition rate. As the

Table 2.3: Chemical composition of aluminum alloy 4043 and 4943 (6; 7).

Aluminum Alloy	Si	Fe	Cu	Mn	Mg	Zn	Ti	Be	Other	Al
4043	4.5–6.0	0.80	0.30	0.05	0.05	0.10	0.20	0.0003	<0.15	Bal
4943	5.0–6.0	0.40	0.10	0.05	0.30–0.50	0.10	0.15	<0.0003	0.15	Bal

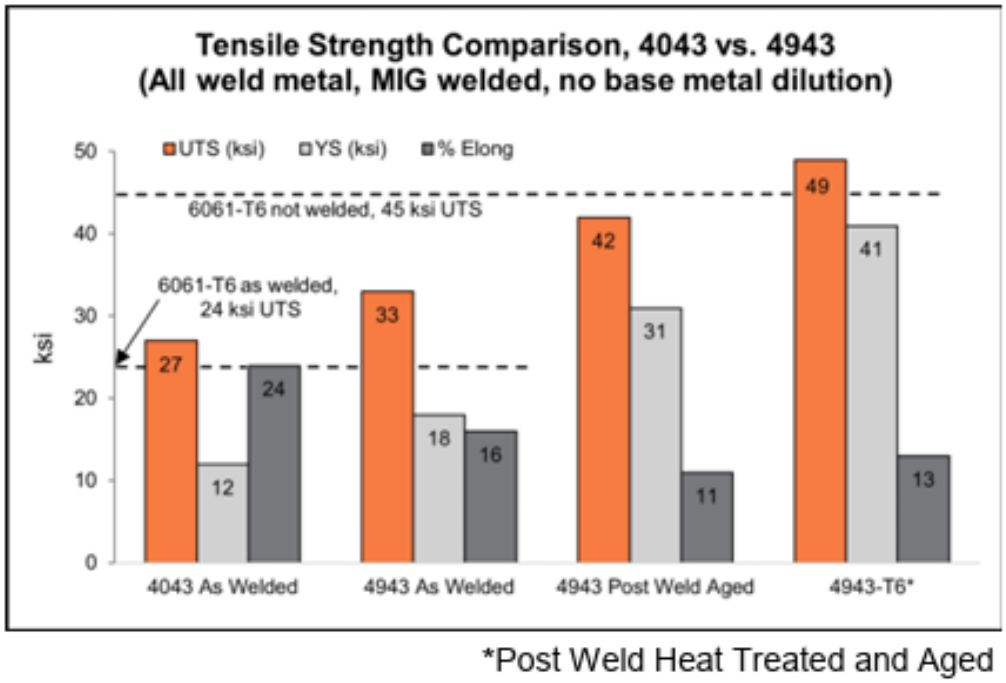


Figure 2.6: Tensile strength of aluminum 4043 and 4943 (13).

wire is fed towards the workpiece, there is a distance from the end of the contact tip to the workpiece, known as the contact tip to workpiece distance (CTWD). This value affects the current and changes in CTWD can affect weld quality. Lastly, shielding gas must be used with appropriate flow rates to achieve an acceptable weld quality (55). Optimal process parameters are usually found through experimentation. GMAW can join a wide range of material types including aluminum alloys.

2.5.2 Gas metal arc welding of aluminum

Wrought and casting forms of aluminum can successfully be welded. The composition of the workpiece dictates its weldability. Many aluminum alloys can be joined but specific filler wire may need to be considered. The primary concern for aluminum, however, is its sensitivity to solidification cracking. Wrought 6xxx series aluminum base metal must be welded with filler alloys, such as Al4043 or Al4943, due to its susceptibility to solidification cracking (56).

Appropriate filler wire must be determined based on the desired weld strength. The heat supplied by the arc, softens the workpiece material adjacent to the weld, this is known as the heat affected zone (HAZ). Microstructurally, the workpiece is altered in the HAZ due to thermal effects. Varying stages of dissolution and precipitates are common and are based on peak temperature and exposure time (56). Heat input from preheating and the welding process parameters affect the width of the HAZ. Heat input over a distance traveled is found in equation 2.1 where the voltage, V, current, I (amps), and travel speed, S (mm/min), influence the heat input, H (kJ/mm) (57).

$$\mathrm{H} = \frac{60 \cdot V \cdot I}{S \cdot 1000} \tag{2.1}$$

Mechanical properties can degrade within the HAZ, jeopardizing the weld quality. Post weld heat treatment can improve the strength of the HAZ for heat treatable alloys such as Al6061 (15). Destructive testing of the weld enables verification of

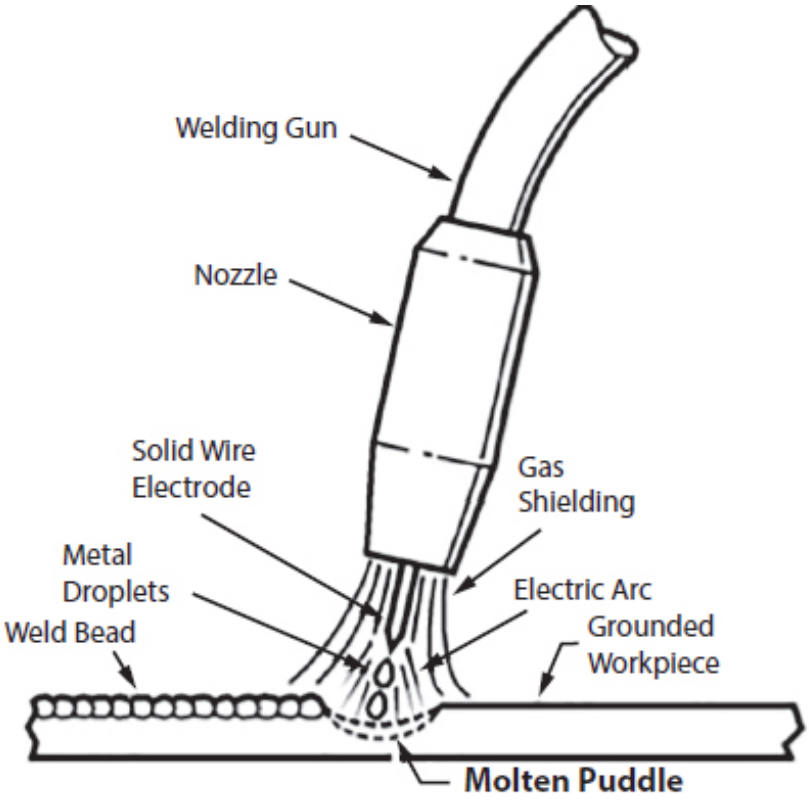


Figure 2.7: Schematic of the GMAW process (14).

satisfactory weld quality. Testing methods include hardness mapping and tensile testing across the weld material, HAZ and unaffected base metal.

2.5.3 Gas metal arc welding of aluminum 4043

Aluminum 4043 is the closest alloy to Al4943 and is used as a comparison in this thesis. Al4043 is not considered heat treatable on its own, but does respond to heat treated conditions when joined with Al6061 because of weld dilution. This filler wire is typically used to join Al6061, which can then be heat treated. The as-welded and PWHT variants consist of different mechanical and microstructural properties. This section focuses on GMAW of ER4043 to Al6061.

Guzman et al. (58) evaluated how changing the current affects the mechanical performance and microstructure of Al6061-T6 plates joined using ER4043 wire in a V-groove cut joint. The as-welded condition and PWHT T4 condition were compared. UTS for the as welded condition varied ranging from 64 to 153.583 MPa, and the PWHT T4 condition ranged from 104.453 to 153.932 MPa. Fracture of the tensile specimens occurred in the fusion zone, otherwise known as the weld material. A hardness profile across the joint was performed where the as-welded HV ranged from 50 to 80 HV and the PWHT T4 condition ranged from about 60 to 75 HV. The Al6061 base material in the as-welded condition had β" precipitates while the T4 PWHT condition had β precipitates. Overall, it was seen that T4 heat treatment improved weld strength.

Stathers et al. (59) established a relationship between hardness and tensile properties in the HAZ of 6061-T6 welded using GMAW with ER4043 wire. V-groove welds were performed with an energy input of 0.26 - 0.42 kJ/mm. Tensile profiles were created by measuring tensile properties at 2 mm intervals, perpendicular to the weld. Hardness was measured at the same positions of the tensile specimens. A minimum HV of about 53 at the weld centerline was measured while about 110 HV was measured at 25 mm away from the center of the weld. A Vickers hardness

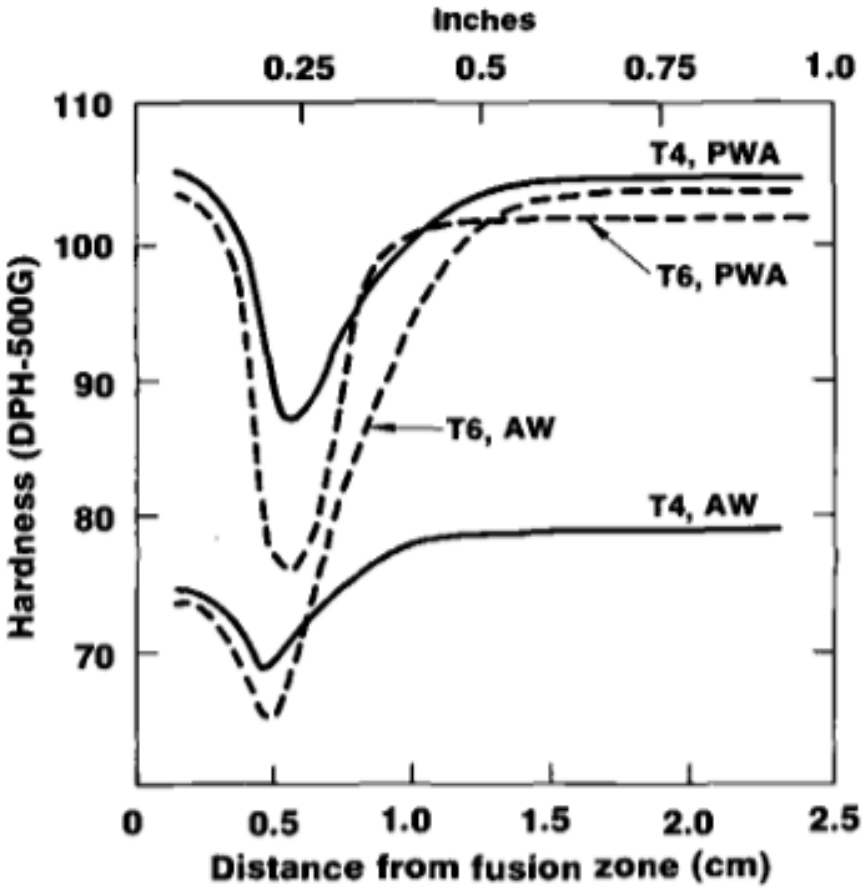


Figure 2.8: Hardness profile of the HAZ for Al6061-T4 and Al6061-T6 base materials in the as-welded (AW) and postweld aged (PWA) conditions (15).

equation relating HV to yield stress (YS) and tensile strength was established by Stathers et al. seen in equations 2.2 and 2.3.

$$0.2\%\ \text{Yield stress} = 2.9263 \cdot HV - 44.289 \tag{2.2}$$

$$\text{Tensile strength} = 2.4079 \cdot HV + 46.39 \tag{2.3}$$

Chikhale et al. (60) varied voltage and current to evaluate how heat input affected the mechanical properties and microstructure of ER4043 wire to Al6061-T6 base plate material in a V-groove joint. It was found that a heat input of 0.805 kJ/mm gave the best overall mechanical properties with a UTS of 196 MPa and HV of 68. Higher heat inputs resulted in larger HAZ widths with larger grain sizes and decreased hardness values.

Ahmed et al. (61) evaluated different Al-Si-Mg filler wires for aluminum welding. A butt joint between two Al6061-T6 plates was joined using ER4043 wire and the properties were evaluated for as-welded and PWHT conditions. UTS values increased after PWHT from 200 MPa in the as-welded condition to 325 MPa in the PWHT condition. Microindentation hardness values followed the same trend where HV decreased in the HAZ and increased in the base material and fusion zone. SEM images showed mostly α-Al phases, Fe rich phases and small amounts of β precipitates because of the small amount of Mg in the composition. Overall, it is seen that HAZ can compromise the mechanical integrity of a welded component where the hardness decreases and premature fractures occur.

2.5.4 Gas metal arc welding of aluminum 4943

Hobart Filler Metals created the ER4943 wire to supplement ER4043 wire enabling PWHT of welded Al4943 material. With the development of this wire and the first paper releasing in 2012, there is little welding research using this alloy. Anderson et al. (62) first discussed the development of the wire and showed that switching from

Al4043 to Al4943 wire is encouraged with increased strength due to the magnesium addition.

Ahmed et al. (16) studied different Al-Si-Mg wires for aluminum welding and included ER4943 wire. A butt joint configuration was used to weld two 2 mm thick Al6061-T6 together using a single pass weld. ER4043 and ER4943 wire are compared in the as-welded and T6 PWHT conditions. ER4043 as-welded shows α-Al, Si, β, α-Al(FeMn)Si, and β-AlFeSi present. Microindentation hardness profiles for both ER4043 and ER4943 showed that the base material exhibited the hardest material at 120 HV. The hardness decreased through the HAZ to a minimum of about 72 HV for ER4043 and 74 HV for ER4943 towards the center of the HAZ. It then increased in the fusion zone, reaching 95 HV for ER4043 and 100 HV for ER4943. Tensile strength was comparable between the alloys with ER4943 having a slightly higher UTS at 225.47 MPa as-welded. The PWHT condition showed significant improvement with Al4943 increasing the average base material hardness to 130 HV and 140 HV in the fusion zone hardness and the tensile strength increasing to 358.73 MPa. The HAZ was dissolved in the heat treatment process and a homogeneous material with fine β" precipitates was formed. Another study using ER4943 wire showed comparable results performed by Ahmed et al. (63).

2.6 Wire arc additive manufacturing

2.6.1 Overview of robotic wire arc additive manufacturing

WAAM is a metal AM process that uses a GMAW system to fuse material together, layer-by-layer (64). Utilization of a GMAW system and a robot mechanism enables robotic WAAM. A GMAW torch is applied to the end-effector of a robot and a commanded path is followed while material deposition is achieved through GMAW techniques. Robotic WAAM has multi-axis capabilities that enable complex geometries to be printed. Large scale components are achieved as build volume is

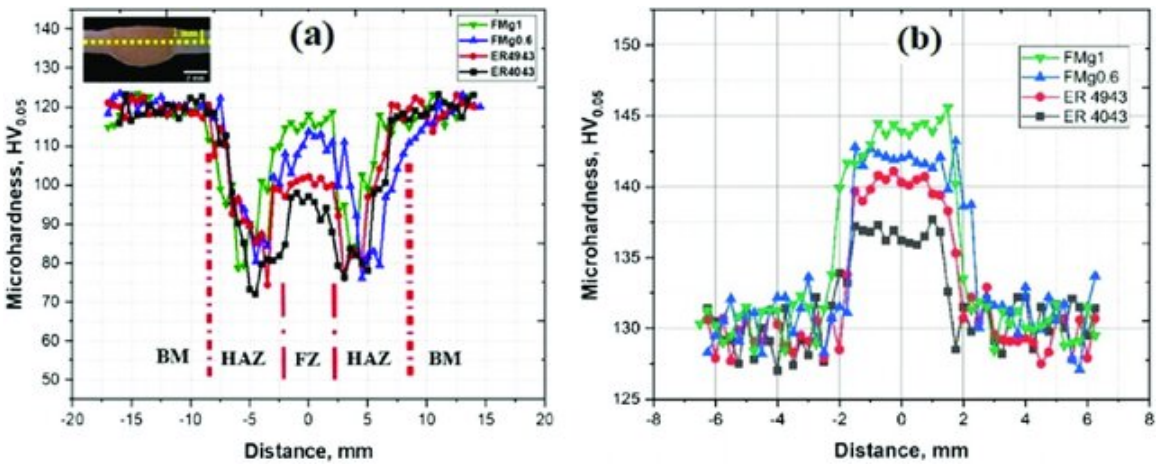


Figure 2.9: Microindentation hardness of Al4943 and other aluminum alloy welded joints (16).

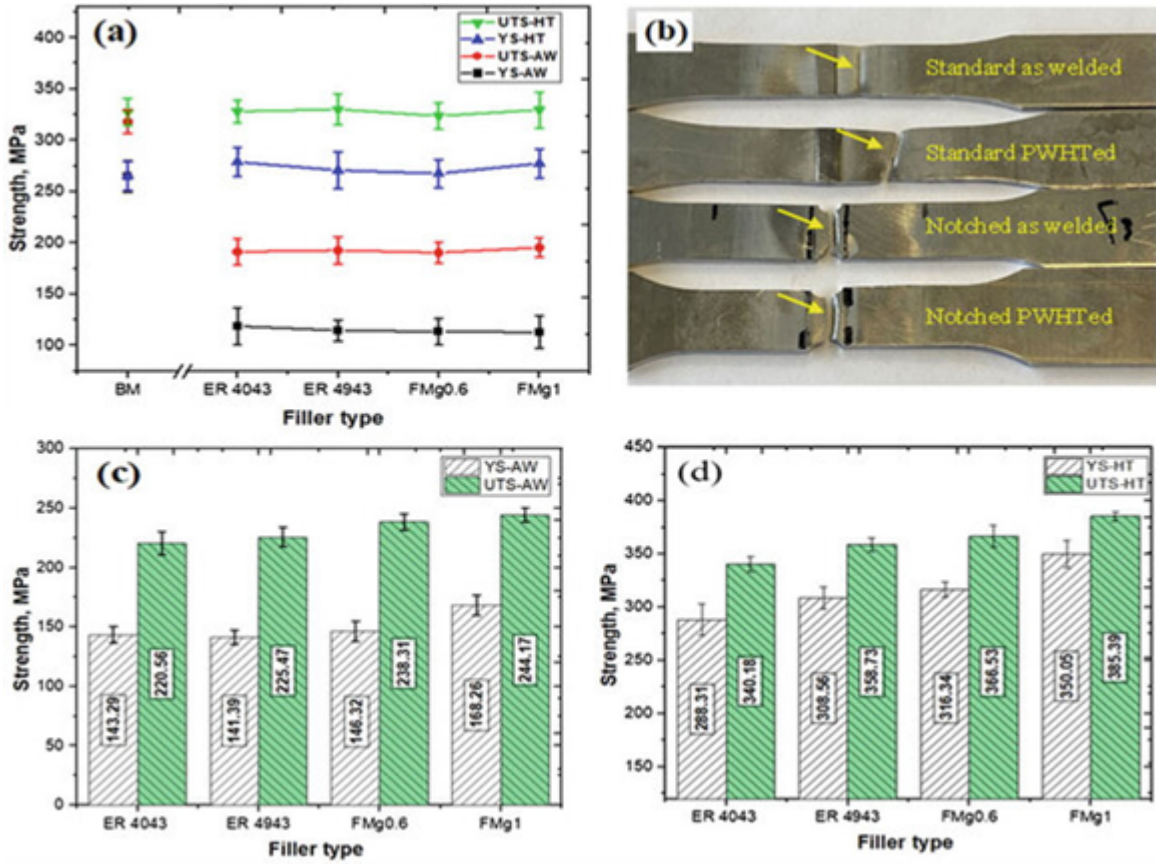


Figure 2.10: Tensile strength of Al4943 and other aluminum alloy welded joints (16).

controlled by the work envelope of the robot. External axes and linear rails increase the work envelope and degrees of freedom to achieve large scale complex geometries. Modular robotic WAAM systems have relatively low operating costs and WAAM has high deposition rates typically ranging from 1 to 4 kg/hr that make this AM method sought after (21).

2.6.2 Cold metal transfer

Cold metal transfer (CMT) is a modified form of a short circuit transfer GMAW process that Fronius developed to address the challenges of welding heat sensitive materials (65). It is a short circuit transfer mode that uses short circuit feedback for precise control of the weld wire feed system. The weld wire is fed forward until a short circuit is identified and is retracted simultaneously. An arc is briefly established and extinguished during wire retraction. This creates a droplet like intermittent melt pool, where the material is cyclically fused and solidified.

2.6.3 Wire arc additive manufacturing of aluminum 4943

There are few studies on the deposition of ER4943 using WAAM technology because of the ER4943 wire being relatively new. The few papers that involve ER4943 using WAAM are detailed.

Ouellet et al. (66) used WAAM to deposit two different single bead wall geometries with Al4943 and Al6061 wire. Mechanical properties in the AD and T6 heat treated condition were compared between the two different alloys. Al4943 performed lower than expected in both the AD and T6 HT condition. Tensile properties are shown in table 2.4. Haselhuhn et al. (67) used WAAM to deposit various aluminum alloy thick walls. A spiral path was used for odd layers while a raster path was used for even layers for all walls. An average porosity of 1.25% was measured in the Al4943 walls. A dendritic microstructure was seen where the secondary dendrite arm spacing (SDAS) increased through the build direction due to heat accumulation throughout

Table 2.4: Tensile properties of Al4043 and Al4943 in the expected as-welded and observed as-deposited conditions.

Reference	Aluminum Alloy	Post processing condition	UTS (MPa)	YS (MPa)	Elongation (%)
Hobart (13)	4043	As-welded	186	83	24
Haselhuhn et al. (67)	4043	As-deposited	141	61	17
Hobart (13)	4943	As-welded	228	124	16
Ouellet et al. (66)	4943	As-deposited	167	70	24
Haselhuhn et al. (67)	4943	As-deposited	193	85	15
Hobart (13)	4943	PWHT T6	338	283	13
Ouellet et al. (66)	4943	T6	227	160	16

the build. Overall, Al4943 had improved properties when compared to Al4043, as seen in table 2.4.

2.6.4 Wire arc additive manufacturing using 4XXX and 5XXX series aluminum

Al4043 is regularly used in WAAM. Many studies evaluate how the printed properties are affected by variables such as process parameters and path plans. Heat input is the most important factor that affects these properties. Various studies of Al4043 and their resulting properties are compared in table 2.5.

Al5356 is similar to 4043 and 4943 but has a slightly different composition. This is primarily an Al-Mg alloy with a minimal amount of Si. Magnesium content ranges between 4.5% to 5.5% while Silicon content is only 0.25%. The increase in Mg allows for a harder and stronger material but lacks the ability to be heat treated.

Al5356 walls have been printed and evaluated with varying process parameters. Typical UTS is around 270 MPa, YS is 135 MPa and hardness is 70 HV. The hardness tends to decrease as the build progresses due to thermal effects. The grain structure in the AD condition tend to have columnar like grains that grow in the build direction. As the heat input increases, the grains grow larger showing increase in grain size as the build progresses. While Al4043 and Al4943 are closer in composition they are still similar to Al5356. WAAM of these alloys are based on the same thermal foundations that influence the mechanical properties and microstructure (68; 69; 70; 71).

2.6.5 Aluminum WAAM and substrate interface

WAAM builds start by depositing the first layer on the substrate. Usually, the substrate is sacrificial as builds are removed during post processing. However, at times substrate integration is wanted and the path planning is modified to ensure the WAAM and substrate interface will not prematurely fail. Mechanical and

Table 2.5: As-deposited properties of Al4043 walls deposited via WAAM.

Reference	Aluminum Alloy	Wall type	UTS (MPa)	YS (MPa)	Elongation (%)	Hardness (HV)	Microstructure
Wang et al. (72)	4043	Thin	165	50	16.1	50	Dendritic structure; Al-Si eutectic at grain boundaries
Ortega et al. (73)	4043	Thin	-	-	-	-	Dendritic structure; Al-Si eutectic between dendrites
Liu et al. (17)	4043	Thin	-	-	-	44-50	Columnar dendrites
Liu et al. (17)	4043	Thick	160-178	-	-	43-58	Mix of coarse columnar and fine columnar grains
Campatelli et al. (74)	4043	Thin	110-130	-	-	40	Mostly dendritic structure

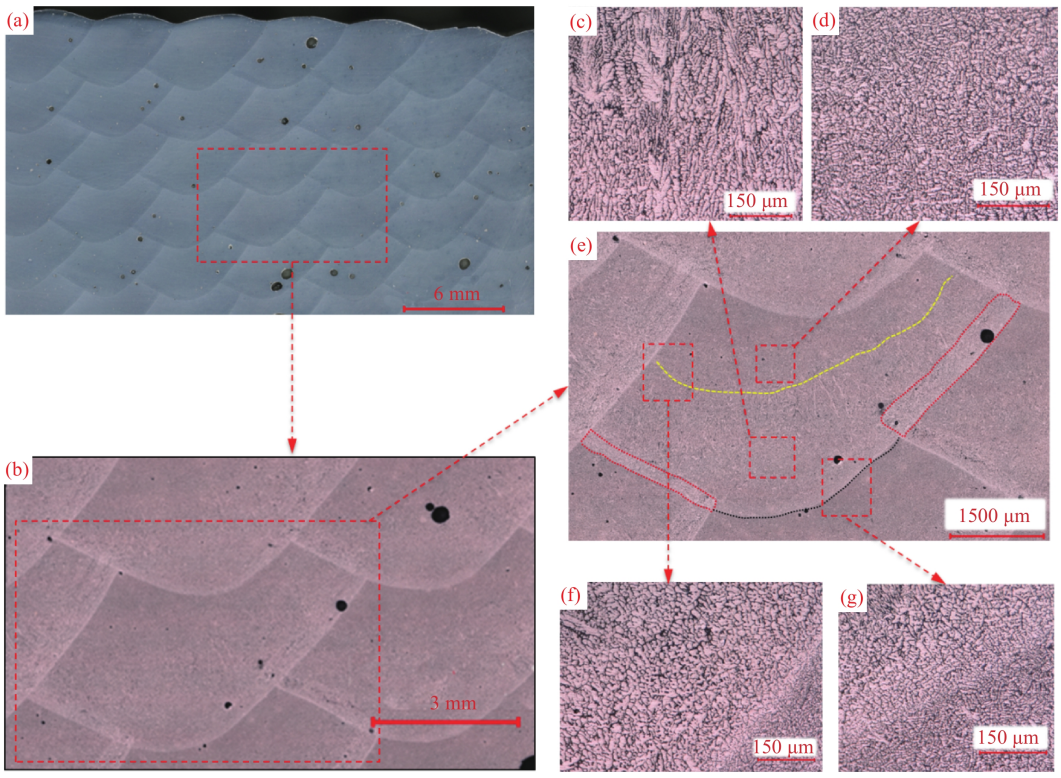


Figure 2.11: Grain structure of an Al4043 thick wall WAAM deposit. (17).

microstructural properties of the substrate can be altered, creating a HAZ within the substrate, due to thermal effects from the WAAM process.

Gu et al. (75) studied how altering the WAAM process parameters effects the interface when depositing Al2319 walls onto a 2219-T87 substrate. Results showed that process changes can affect the mechanical and microstructural properties in the WAAM material as well as the interface. However, post process heat treatment creates a homogeneous material with consistent properties.

Eimer et al. (76; 77) evaluated the mechanical properties of a WAAM and substrate interface to assess whether the substrate can be integrated into the final component. Various 2xxx series wire was deposited onto different substrates with varying mechanical and thermal conditions. It was found that similar wire and substrate material had the best resulting properties allowing for substrate integration. Heat treatment conditions improved the properties across the substrate, interface and WAAM material.

2.7 Metal-metal multi-materials

2.7.1 Overview of multi-materials

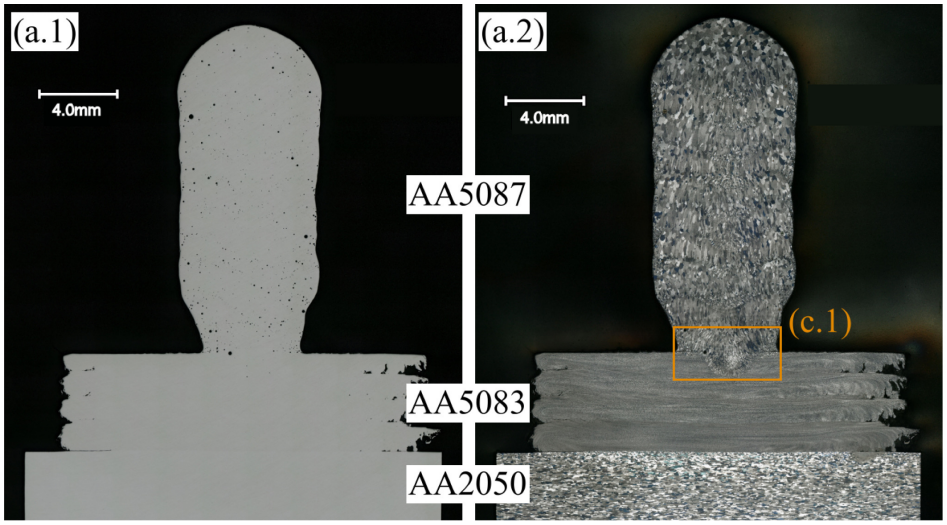
Multi-material additive manufacturing (MMAM) is the process of combining two or more materials within a single component while using additive processes. All multi-materials (MM) have an interface region between the two materials which may have a questionable integrity. At times the interface region can be the weak link in the component because of compositional variation and defects. To prevent weak areas, material compatibility is key or creating a functionally graded material may be needed.

2.7.2 WAAM of multi-materials

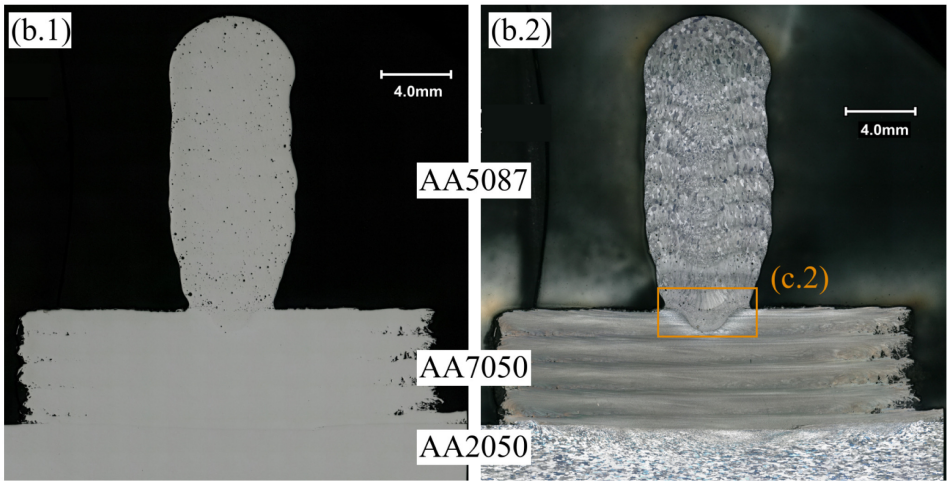
Currently, one paper exists that combines a solid state friction based additive technique and WAAM to create a MM. Kallien et al. (18) developed a MM using friction surfacing to deposit Al7050 and Al5083 onto an Al2050 substrate. Then using WAAM, Al5087 was deposited atop the FS deposits to create the MM. Interlayer rolling was performed during some builds and the properties of the varied builds were compared. A microindentation hardness profile was created showing a homogeneous hardness within the Al5083 while an increase in hardness through the Al7050. The maximum hardness existed at the top layer of the FS deposit, consistent with prior FS and AFSD hardness trends in precipitation hardening alloys. For the FS and WAAM MM, the peak hardness was located at the interface. A large decrease in hardness was present within the WAAM material. Interlayer rolling increased the hardness values in the WAAM. Tensile properties for the AD condition showed comparable values with a reduced UTS when compared to a wrought plate interface. Interlayer rolling did improve these properties.

Hauser et al. (78) developed an aluminum WAAM multi-material consisting of Al5087 and Al6060 with deposited layers alternating between the two materials. Nominal mechanical properties of the two materials deposited using WAAM were established and compared to the AD and HT conditions of the MM. Al6060 has the ability to be heat treated with about 0.6% Mg although Al5087 does not respond to heat treatment conditions with about 5% Mg content. It was found that the tensile strength of the MM was limited by the individual alloys, not the interface. The Al5087 deposit showed higher hardness due to the increased Mg content.

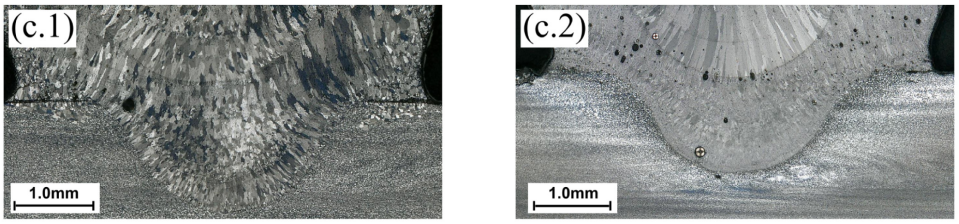
Liu et al. (19) analyzed the interface between a bi-metal consisting of mild steel and silicon bronze printed using WAAM. Visually, there was a distinct interface between the two alloys however, mixing between the alloys was present. Concentrations of iron were measured in the silicon bronze, indicating a slight gradient of material. A small intermixing zone was present as depicted in figure 2.14. Tensile



(a)



(b)



(c)

Figure 2.12: Cross sections of the WAAM and FS interface before and after etching (18).

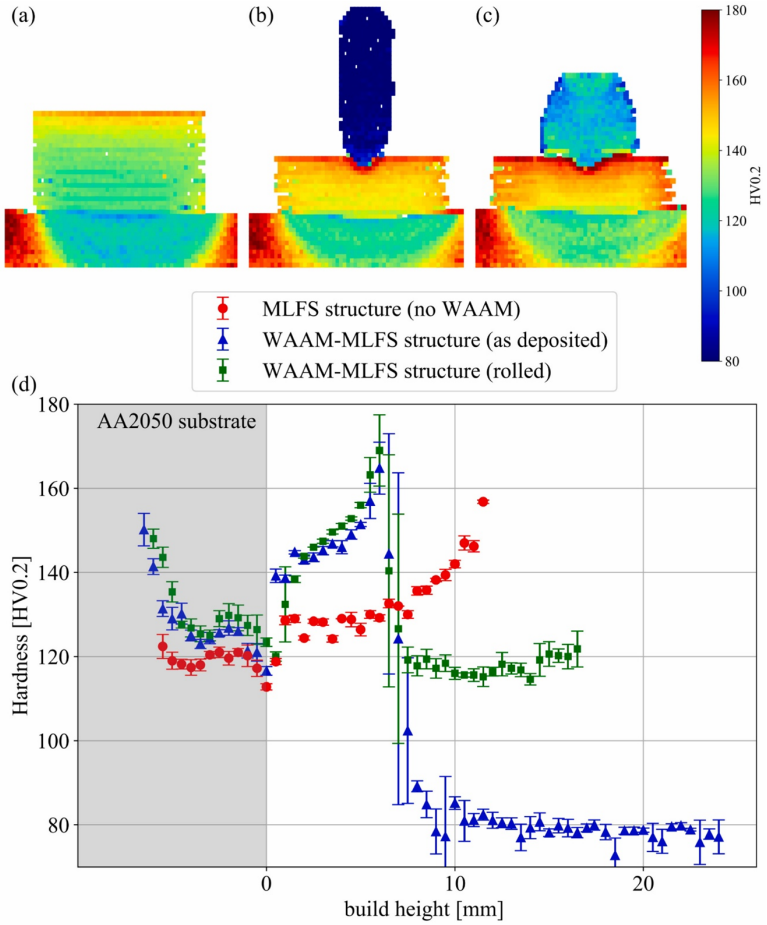


Figure 2.13: Hardness profile across the WAAM and FS interface (18).

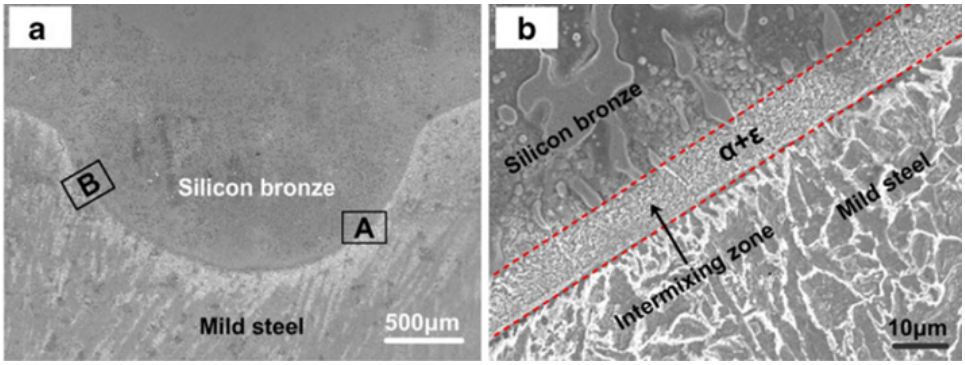


Figure 2.14: SEM images of the mild steel and silicon bronze WAAM interface (19).

tests across the interface fractured within the bronze, indicating that the bronze was the limiting material strength and that the bond at the interface was stronger than the bronze material.

Chapter 3

Materials and Methods

3.1 Overview of multi-material deposits

Various MM aluminum walls were sequentially deposited using AFSD and WAAM. A primary Al6061 wall was deposited using AFSD and an Al4943 secondary wall was deposited on either the top or side of the AD or machined AFSD surface using WAAM. A total of thirteen builds were printed with differing build orientations, surface roughness, and/or post-process heat treatment conditions. The various builds are shown in figure 3.1.

3.2 AFSD of aluminum 6061

3.2.1 AFSD process parameters

Using a MELD L3 discrete feed AFSD machine, as seen in figure 3.2, Al6061-T6 feedstock was deposited on a 12.7 mm thick Al6061-T6 substrate. The substrate surface was cleaned with isopropyl alcohol prior to deposition. The feedstock consisted of square rods that measured 12.7 mm square by 508 mm in length. Each rod was used until insufficient material remained, initiating the reload of a new rod. An H13 steel tool with four teardrop protrusions approximately 2.3 mm in depth was

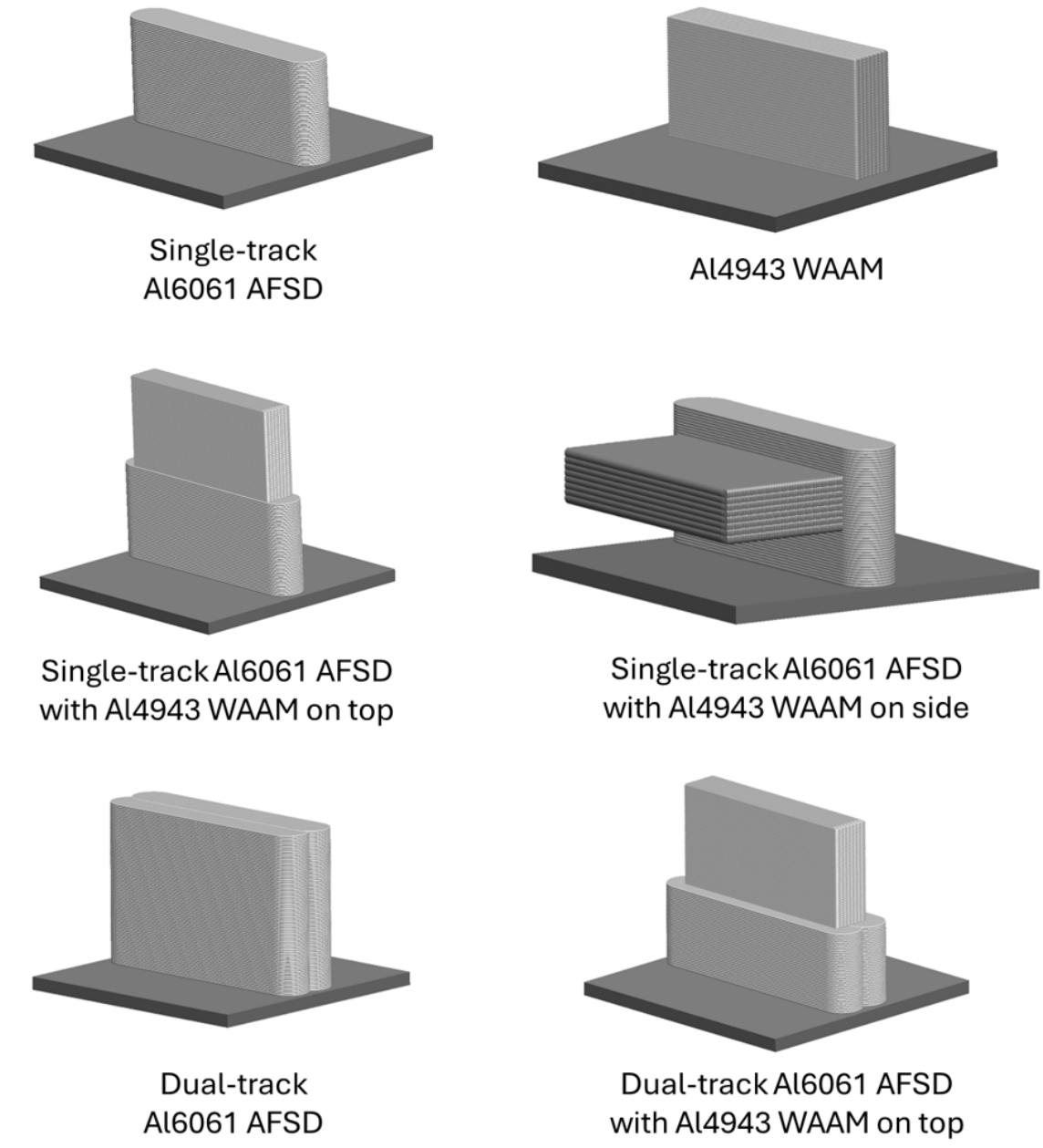


Figure 3.1: All printed build orientations.

used. Process parameters used during the AFSD deposits can be seen in table 3.1. A K-type thermocouple is embedded within the tool where closed-loop PID control enables deposition at the specified setpoint temperature of 380°C. This setpoint temperature is maintained throughout the deposition through feedback control that enables modulation of the spindle speed. The equipment and process parameters provided were used for all Al6061 AFSD walls. This study deposited single-track and dual-track builds. Single-track builds had a deposition rate of 2.12 kg/hr. All dual-track builds had an adjusted material feed rate for the overlapping track as seen in table 3.1.

3.2.2 Single-track Al6061 AFSD walls

A total of seven single-track Al6061 AFSD walls were deposited for this study. Each single-track wall geometry consisted of a 215.9 mm length, 48.6 mm width, and 96.84 mm height. The width of a single-track matches the total width of the deposit at 48.6 mm. The commanded tool path traversed solely in the Y-direction for 165.1 mm and alternated direction for each deposited layer. Subsequently, the advancing and retreating side of the build alternates as well. A commanded layer height of 2 mm was used. The same location was used for the start and reload point, where a reload was performed every four layers. This location was ignored, due to the uncertainty within it. A dimensioned graphical representation of a single-track Al6061 wall deposited using AFSD is shown in figure 3.3.

Of the seven single-track Al6061 walls, two remain solely in the Al6061 AFSD condition. Of these two walls, one remains in the AD condition and the other is HT to a T6 temper designation. These two walls provide baseline hardness properties that are then compared to the MM walls. The other five single-track walls are used to create the Al6061-Al4943 bimetallic.

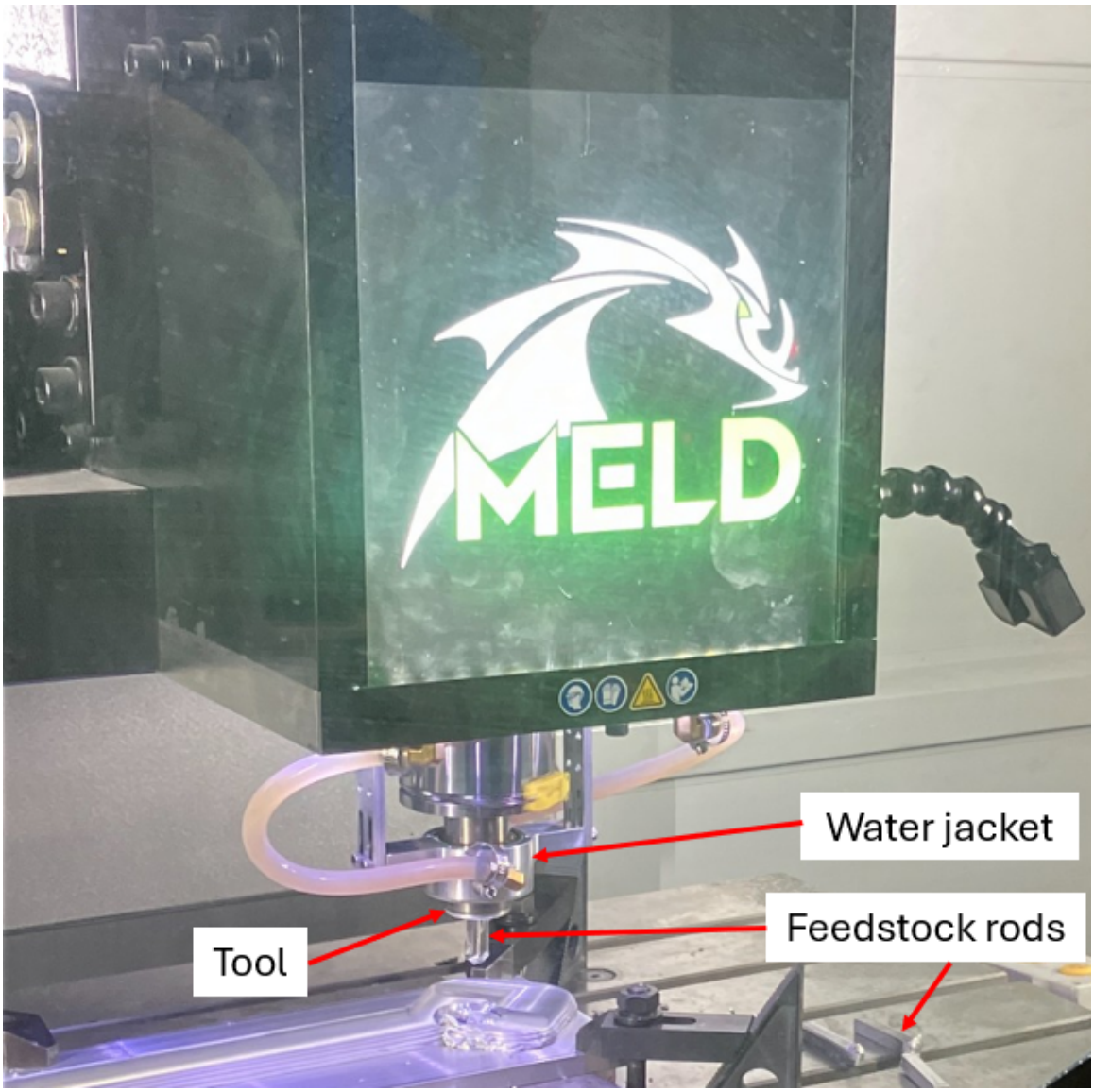


Figure 3.2: Schematic of the MELD L3 machine.

Table 3.1: Process parameters used during single-track and dual-track AFSD of Al6061.

Track type	**Temperature setpoint (°C)**	**Spindle speed (rpm)**	**Tool feed rate (mm/min)**	**Material feed rate (mm/min)**	**Layer height (mm)**
Single-track	380.0	220 - 320	254.0	152.4	2.0
Dual-track (overlap)	380.0	220 - 320	254.0	81.3	2.0

3.2.3 Dual-track AFSD walls

Four dual-track builds were printed for this study. A wall geometry was deposited that consisted of a 222.25 mm length, 73.03 mm width and 96.84 mm height for all dual-track builds. The commanded tool path traversed in the positive Y-direction for 165.1 mm and then 25.4 mm in the X-direction using an arc-like motion. Following the arc-like motion, the tool then traversed in the negative Y-direction where intermixing with the previous track was enabled. This created a track overlap of 25.4 mm as the distance between track center lines was 25.4 mm. A Z height adjustment of the specified layer height of 2 mm was achieved at the end of the second track. Another layer was deposited in the opposite directions for the two tracks. This alternates the printing direction as well as the advancing and retreating sides. The track overlap region intermixes the advancing and retreating sides every layer. The same location was used for the start and reload point, where a reload was performed every two layers. This location was ignored due to the uncertainty within it. The same process parameters used for the single-track builds were used again in the dual-track builds with one exception. The overlapping track had a modified material feed rate to prevent an excess of flash. A dimensioned graphical representation of a dual-track Al6061 wall deposited using AFSD is shown in figure 3.4.

Of the four dual-track Al6061 walls, two remain in the Al6061 AFSD condition. Of these two walls, one remains in the AD condition and the other is HT to a T6 temper designation. These two walls provide Al6061 dual-track baseline hardness properties that are then compared to the MM walls. The other two dual-track walls are used to create the Al6061-Al4943 bimetallic structure, where the track overlap region of the Al6061 deposit is studied.

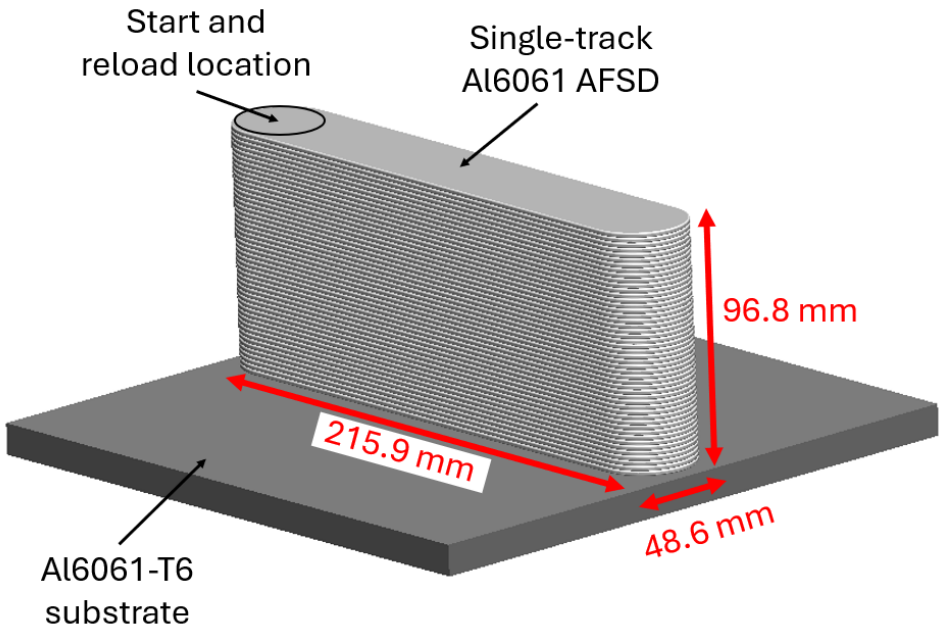


Figure 3.3: Graphical representation of a single-track Al6061 AFSD wall.

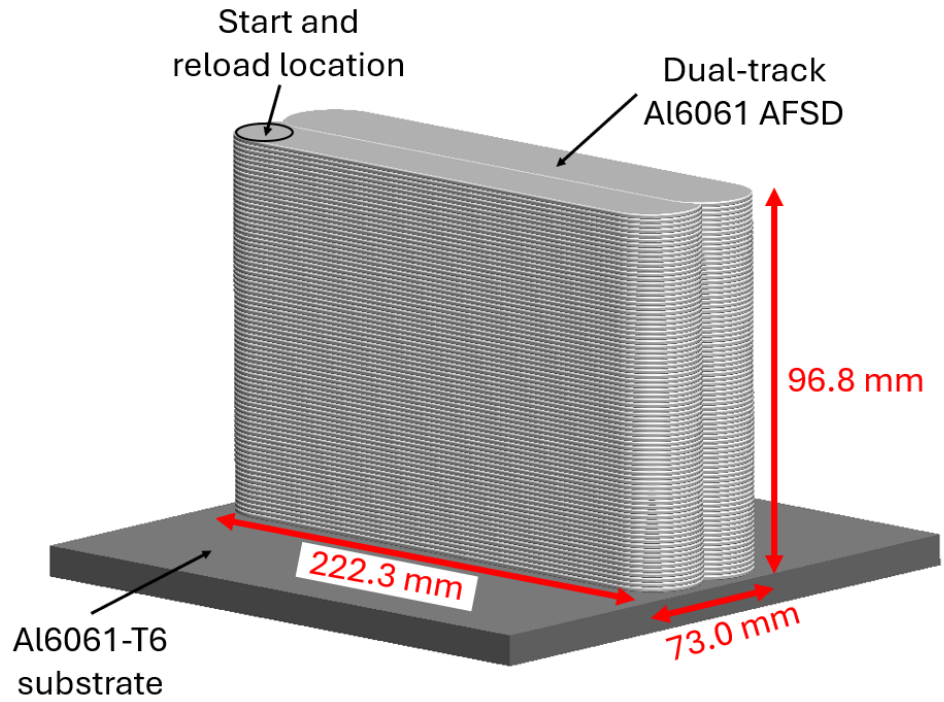


Figure 3.4: Graphical representation of a dual-track Al6061 AFSD wall.

3.3 WAAM of aluminum 4943

3.3.1 WAAM process parameters

Using an AML3D Arcemy WAAM cell, as seen in figure 3.5, Al4943 was deposited on an Al6061 AFSD deposit or an Al6061-T6 19.05 mm substrate. The Arcemy cell includes an ABB IRB 6700 robot with a Fronius TPS 500i power supply and a two-axis positioner. A 1.2 mm diameter ER4943 wire feedstock was used with 100% Argon shielding gas. Process parameters used during the WAAM deposits can be seen in table 3.2. A deposition rate of 1.46 kg/hr was achieved. A laser pyrometer was used to monitor the interpass temperature, which is the targeted temperature to initiate deposition of the next bead. An interpass temperature of 100°C was used. The equipment and process parameters discussed was used for all Al4943 WAAM walls.

3.3.2 WAAM walls

A total of ten multi-bead WAAM walls were used for this study. A wall geometry was deposited that consisted of a 177.8 mm length, 44.45 mm width and 100.01 mm height for all of them. WAMSoft is a path planning software provided with the Arcemy cell that was used to program the robot motions for deposition. A raster pattern was used for the internal region, followed by a contour bead that follows the outer wall border. A bead width of 7.0 mm with a bead offset of 3.9 mm and a layer height of 3 mm was used. The print direction alternates per layer for both the internal raster and outer contour. The strike location and crater zone, also known as the starting location and stop location in WAAM, alternate between two opposing corners for the internal raster. The outer contour bead starts and stops at the same location within a layer but increments around the contour, clockwise, by 50 mm on a per-layer basis. The outer contour beads tend to need multiple passes every 3 layers to counteract underbuild along the edges of the deposit. The first layer of the path plan used during

Table 3.2: Process parameters used during WAAM of Al4943.

Current (A)	**Voltage (V)**	**Wire feed rate (m/min)**	**Travel speed (mm/s)**	**Energy (kJ/mm)**
161.0	15.3	8.0	10.0	0.246

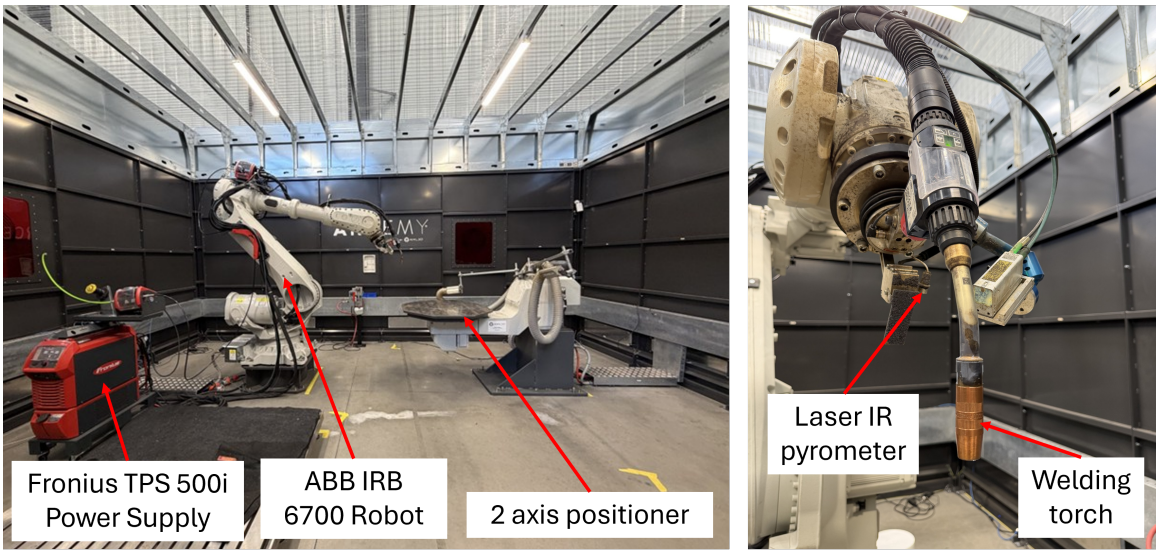


Figure 3.5: Schematic of the AML3D Arcemy WAAM cell.

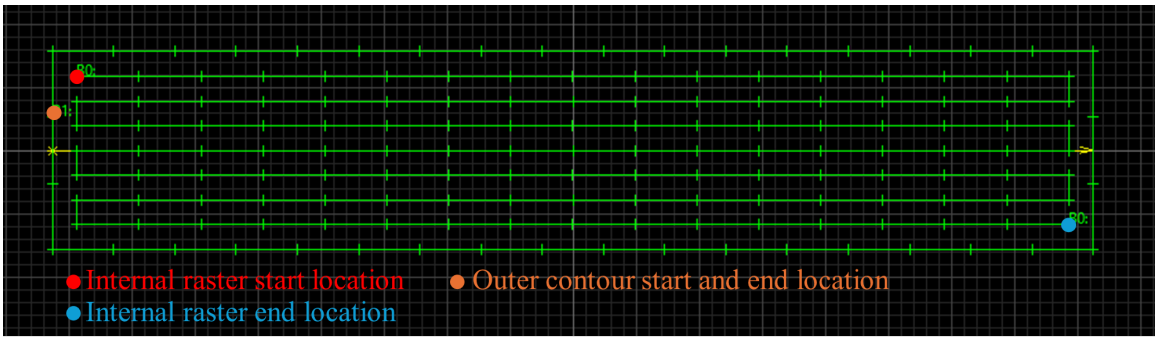


Figure 3.6: First layer path plan for an Al4943 WAAM wall using WAMsoft.

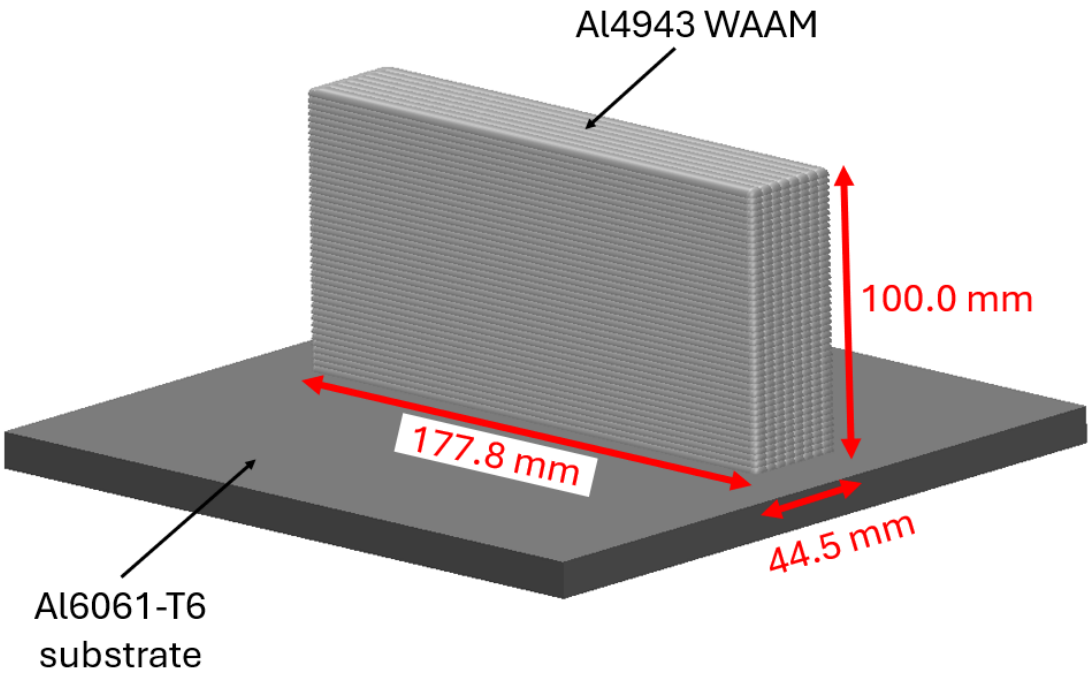


Figure 3.7: Graphical representation of an Al4943 wall deposited via WAAM.

deposition and a dimensioned graphical representation of an Al4943 build deposited via WAAM are provided in figures 3.6 and 3.7, respectively.

3.3.3 WAAM only build variations

Two baseline Al4943 WAAM walls were deposited on a 19.05 mm thick Al6061-T6 substrate. The substrate surface was ground with a flap disk and cleaned with isopropyl alcohol to remove any surface oxides. It was then preheated to 80°C prior to deposition. One of the baseline Al4943 walls were left in the AD condition and the other was heat treated following the same T6 heat treatment schedule as the Al6061 AFSD builds.

3.4 Al6061-Al4943 multi-material builds

3.4.1 Multi-material builds

An Al6061 single-track AFSD wall was deposited on a 12.7 mm Al6061-T6 substrate. An Al4943 WAAM wall was then deposited on the Al6061 AFSD deposit, where printing orientation of the Al4943 was varied among builds. A total of five Al6061 single-track AFSD and Al4943 WAAM MM walls were deposited. Among these, two different MM build orientations were used. Three builds consisted of Al6061 deposited first and then Al4943 deposited on the top surface of the Al6061 build. The other two builds had Al6061 deposited first and then Al4943 deposited on the machined side profile of the Al6061 deposit.

For the three builds that consisted of Al4943 deposited on the Al6061 AFSD top surface, one was left AD, and the other two had the top surface machined. An intermediate face milling operation of the Al6061 top surface was used on two of these three builds, to ensure a flat, smooth deposition surface for the Al4943 WAAM. A 63.5 mm diameter face mill was used to cut 3 mm from the top of the deposit, allowing WAAM of Al4943 to begin within the second AFSD layer from the top.

Surface roughness measurements were performed using a Mitutoyo SJ210 surface profilometer. All surfaces that acted as WAAM deposition surfaces, were measured. Of the two top surface machined builds, one was in the AD condition and the other was in the HT condition. The third build deposited Al4943 on the AD Al6061 AFSD top surface without an intermediate machining operation. The surface roughness affects on the Al6061-Al4943 interface were compared. This build was sectioned in half, leaving one side in the AD condition and the other HT.

The final two single-track Al6061 AFSD builds, deposited Al4943 along the side profile of the Al6061 deposit. An intermediate milling operation of the Al6061 AFSD surface was performed. A 19.05 mm diameter endmill with a 57.15 mm length of cut and a 19.05 mm diameter end mill with a 101.6 mm length of cut was used to remove 88.9 mm material axially and 9 mm of material radially from the deposit. This results in 3 mm of material removed from the side wall, with respect to the AFSD tool edge, as recommended (12). This ensured a smooth surface for WAAM deposition and removed any possible edge defects that are usually present within an AFSD build. These are again compared in the AD and HT conditions. A dimensioned graphical representation of the two different build orientations, Al4943 deposited on the top and Al4943 deposited on the side surface of the Al6061 AFSD builds, are shown in figures 3.8 and 3.9.

3.4.2 Dual-track multi-material build variations

Two of the four dual-track Al6061 AFSD walls were used to deposit Al4943 on the top surface after an intermediate face milling operation. The same cutting profile and parameters were used for the dual-track face milling as the single-track face milling. The dual-track AFSD deposit has an increased width that includes a track overlap region. The dual-track Al6061 with Al4943 deposited on the top surface is seen in figure 3.10.

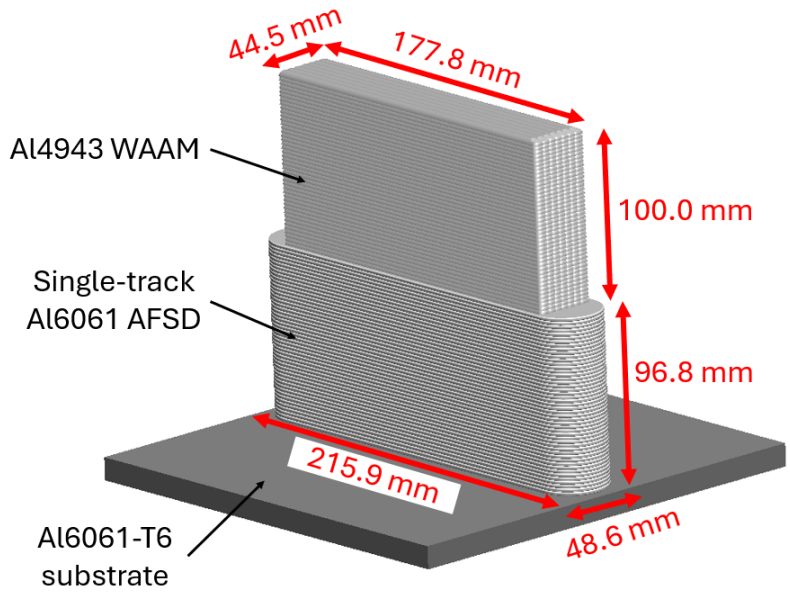


Figure 3.8: Graphical representation of an Al6061-Al4943 multi-material with Al4943 deposited on the top surface of a single-track Al6061 wall.

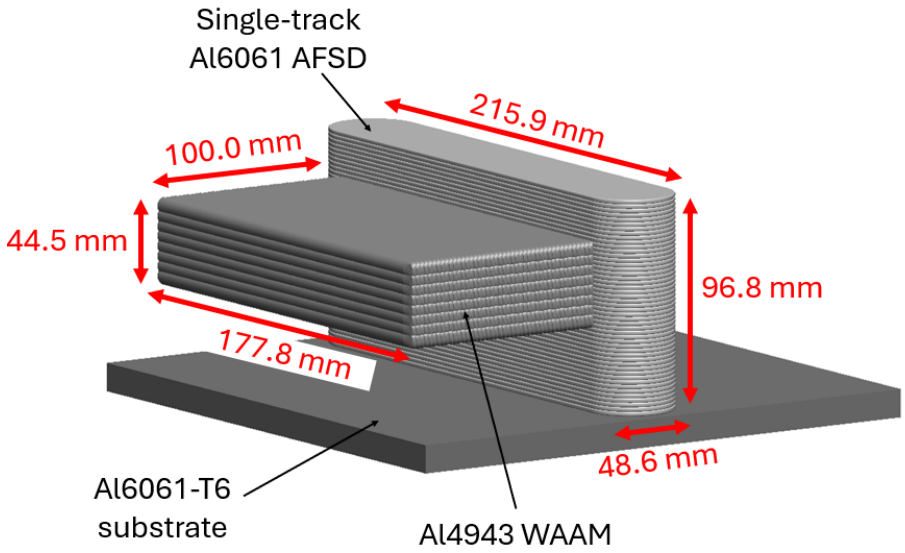


Figure 3.9: Graphical representation of an Al6061-Al4943 multi-material with Al4943 deposited on the side surface of a single-track Al6061 wall.

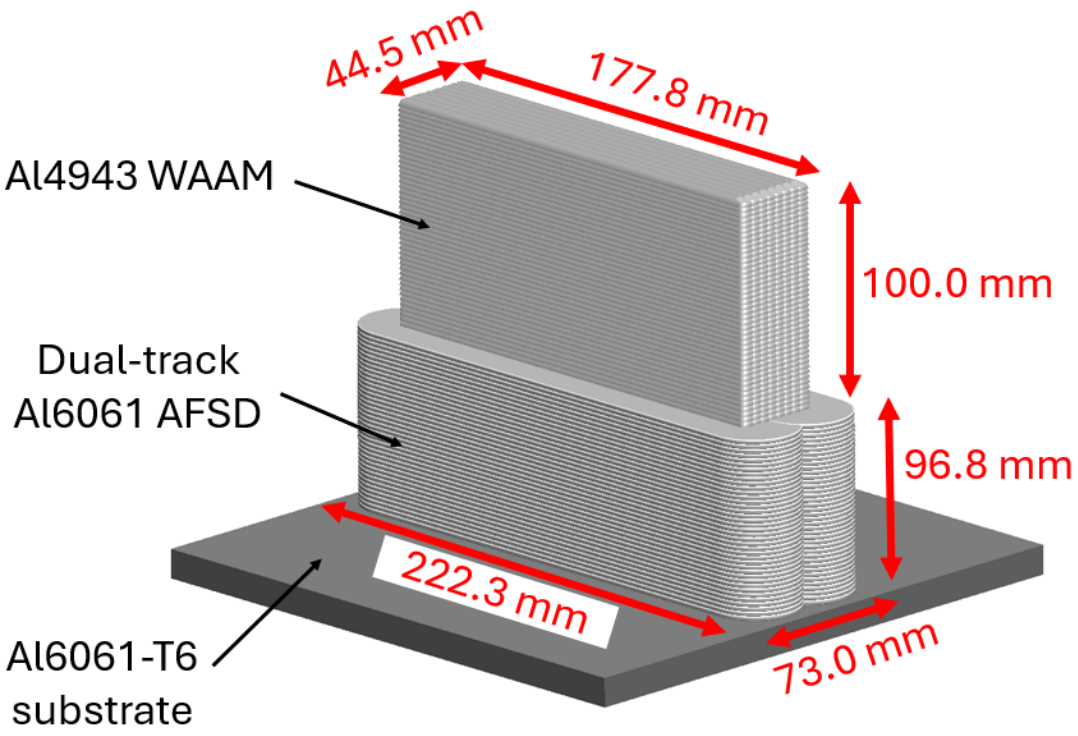


Figure 3.10: Graphical representation of an Al6061-Al4943 multi-material with Al4943 deposited on the top surface of a dual-track Al6061 wall.

3.5 Deposited builds

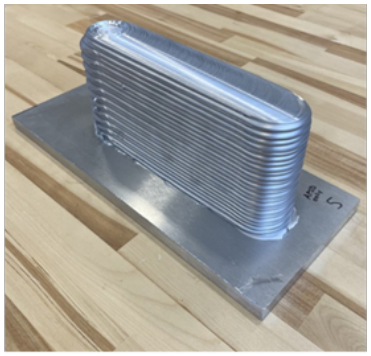
3.5.1 Overview of deposited builds

Each build was successfully deposited, enabling development of a MM that consisted of Al6061 deposited via AFSD and Al4943 deposited via WAAM. Each different orientation was deposited without any visual defects. Each deposit has an AD and HT version. The AD version of each build orientation can be seen in figures 3.11 and 3.12.

3.6 Heat treatment of deposits

3.6.1 T6 heat treatment

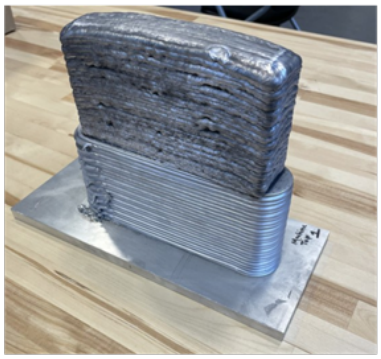
For all print variants, there exists an AD and a HT condition. The HT procedure follows ASTM B918/B918M-20 guidelines to achieve a T6 temper designation for Al6061-T6 (79). The HT was performed at Bodycote and the certifications can be found in appendix A.2 and A.3. The HT schedule included a solutionizing stage, where each build was subjected to an elevated temperature of 529°C ±6°C for 8 hours. They were then water quenched for a 10 minute duration with an 8 second quench delay. Next, a precipitation hardening stage consisted of subjecting the builds to a temperature of 177°C ±6°C for 8 hours. Lastly, all builds were air cooled to ambient temperature. Thus, a T6 temper designation was achieved so that a comparison of AD and HT conditions could be executed.



Single-track
Al6061 AFSD



Al4943 WAAM



Single-track Al6061 AFSD
with Al4943 WAAM on
machined top



Single-track Al6061 AFSD
with Al4943 WAAM on
machined side



Dual-track
Al6061 AFSD



Dual-track Al6061 AFSD
with Al4943 WAAM on
machined top

Figure 3.11: Different build orientations after deposition.

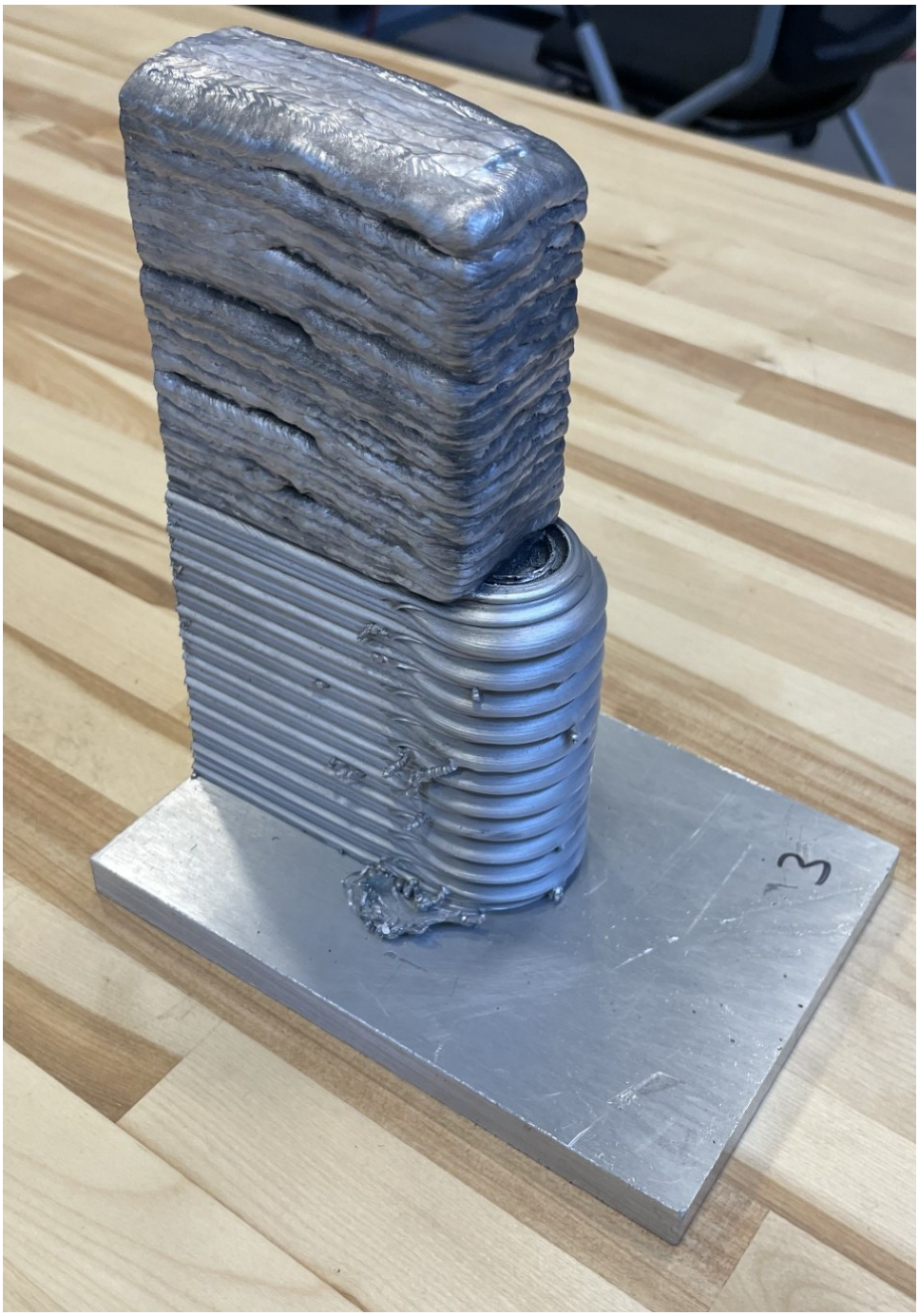


Figure 3.12: A halved multi-material build consisting of a single-track Al6061 AFSD with Al4943 deposited via WAAM on the top AD AFSD surface.

3.7 Sample Extraction

3.7.1 Single alloy microindentation hardness sample extraction

Each single alloy build, either Al6061 deposited via AFSD or Al4943 deposited via WAAM, in the AD and HT condition, followed the same sample extraction plan. This includes both single-track and dual-track Al6061 AFSD builds. All samples were extracted using a Mitsubishi MV2400 wire electric discharge machine (EDM). Microindenation hardness samples were centrally located at the top of the builds. These samples consisted of a 60 mm length, vary in width and have a 12.7 mm thickness. An example of a microindentation hardness sample extraction location from a single-track Al6061 AFSD build can be seen in figure 3.13. Sample extraction locations of other single alloy builds can be seen in appendix A.4 and A.5.

3.7.2 Single-track multi-material sample extraction

The single-track Al6061 build with Al4943 deposited on the AD AFSD top surface was used as a guideline for future sample extractions. Within this build, metallography samples, tensile specimens and microindentation hardness samples were extracted. Metallography samples were extracted from the Al6061, Al6061-Al4943 interface, and Al4943 regions of the builds, where the YZ surface was evaluated. Metallography samples were cut into 25.4 mm x 38.1 mm x 12.7 mm blocks. Metallography samples were not extracted from other builds as the metallurgy is expected to be repeatable. Nine vertical and three horizontal miniature tensile specimens in both the XZ and YZ planes were extracted from the middle of the build. These were prepared according to ASTM E8/E8M-20 (80). The specimen dimensions are in accordance with the dimensions of the miniature specimen 4 outlined in Table A1.2 of ASTM E8/8M-20. These include a square width and thickness of 1.524 mm and a gage length of 9.91 mm. These dimensions are shown in appendix A.19. Microindentation hardness

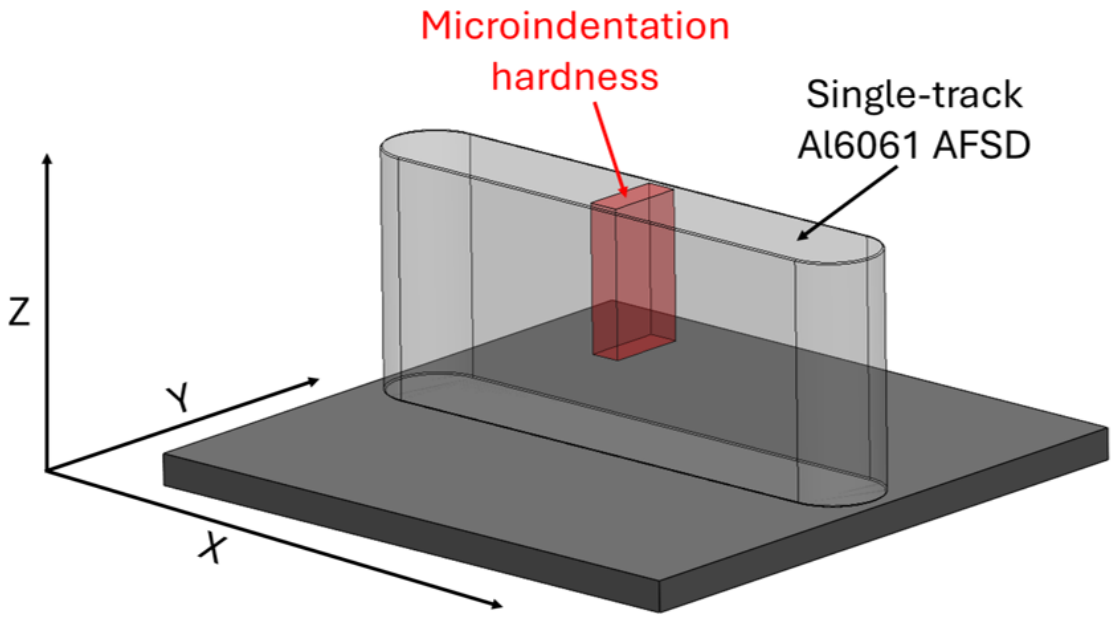


Figure 3.13: Extraction site of a microindentation hardness sample from an Al6061 AFSD single-track wall.

samples had a 38.1 mm length, a thickness of 12.7 mm and varied in width. Samples were extracted from the Al6061, Al6061-Al4943 interface, and Al4943 region of the builds where the YZ surface was evaluated. Sample extraction is replicated for the AD and HT condition of this build. After preliminary hardness testing from the AD condition, the HAZ was measured. The gap between samples in the AD condition was removed in the HT condition as it was deemed unnecessary. Sample extraction from the halved Al4943 deposited on the AD Al6061 AFSD surface can be seen in figure 3.14.

All other builds only evaluate the mechanical properties using tensile and/or hardness testing. Metallography is not evaluated in any other builds. All other single-track Al6061 AFSD walls with Al4943 deposited on the top surface had vertical miniature tensile specimens extracted across the interface in the XZ and YZ planes. Another tensile sample set, using a modified miniature specimen 4, was used to compare to the miniature tensile testing sample set. The modified tensile specimen, has an increased gage length to 70 mm. This captures the overaged zone in both alloys, when in the AD condition. This is solely examined for the Al4943 deposited on the machined AFSD top surface. The specimen dimensions are shown in appendix A.20. A single microindentation hardness sample that consisted of a 60 mm length, varied width, and a 12.7 mm thickness was cut, centered across the interface with 30 mm of length into each alloy for evaluation. Thus, the Al6061, Al6061-Al4943 interface and Al4943 regions are all captured within the one hardness sample. This is replicated for the AD and HT conditions. Sample extraction locations can be seen in figures 3.15 and 3.16.

3.7.3 Dual-track multi-material sample extraction

Microindentation hardness samples from the dual-track Al6061 walls with Al4943 deposited on the top machined surface were also extracted. The hardness in the track overlap region of the Al6061 and how it affects the Al6061-Al4943 interface was

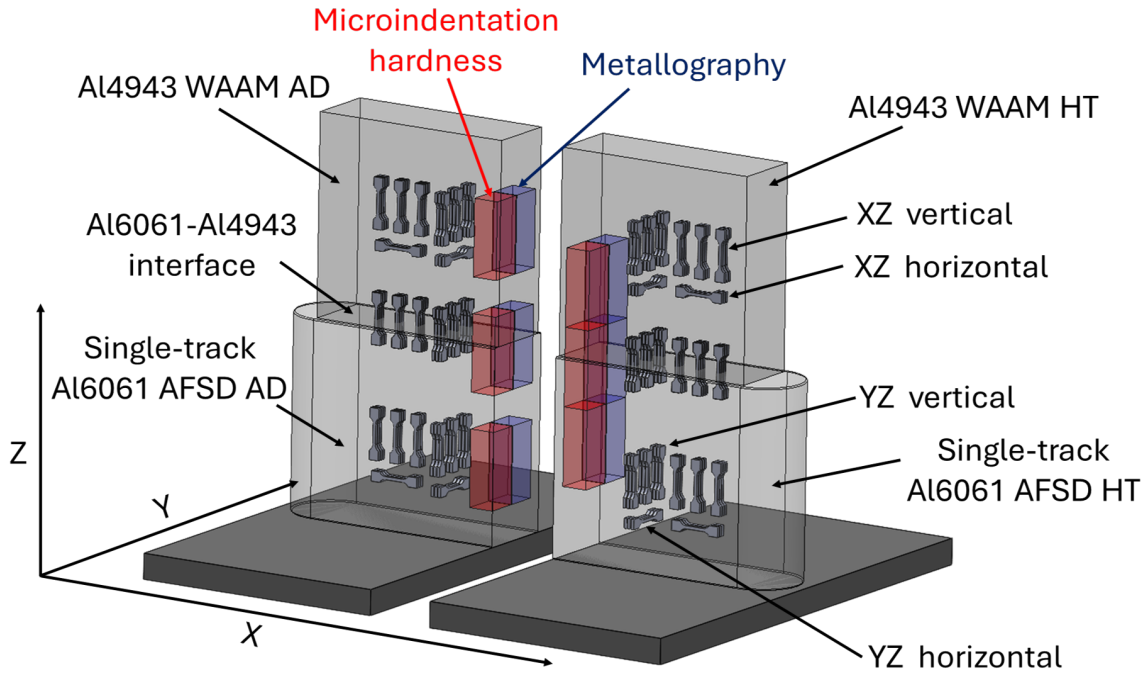


Figure 3.14: Sample extraction from the halved Al4943 deposited on the AD Al6061 AFSD surface wall.

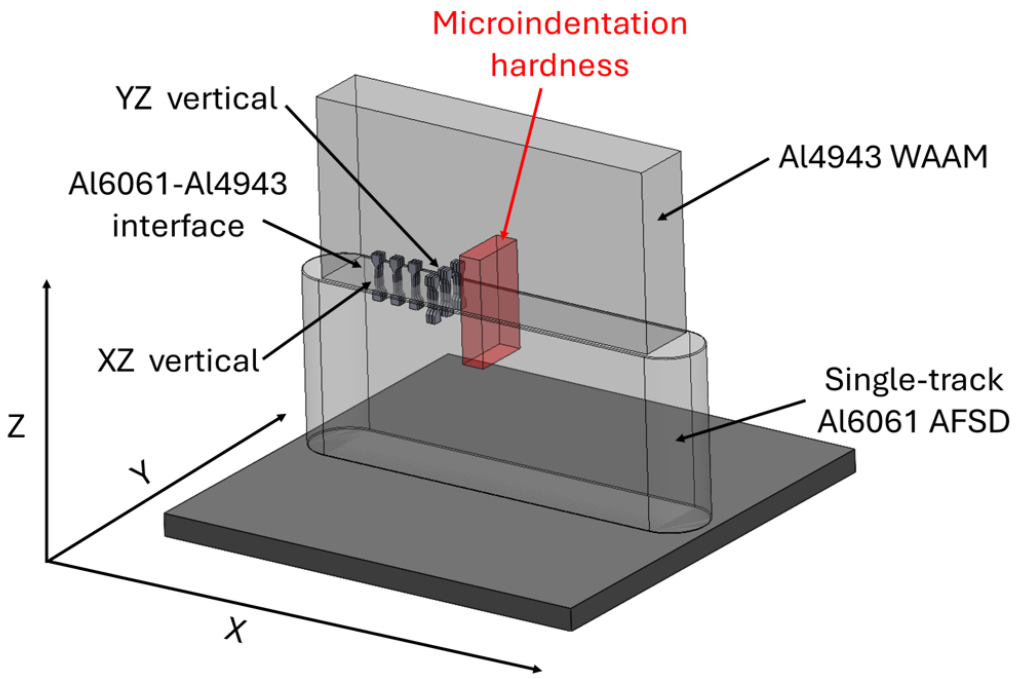


Figure 3.15: Sample extraction from Al4943 deposited on the Al6061 machined top surface wall.

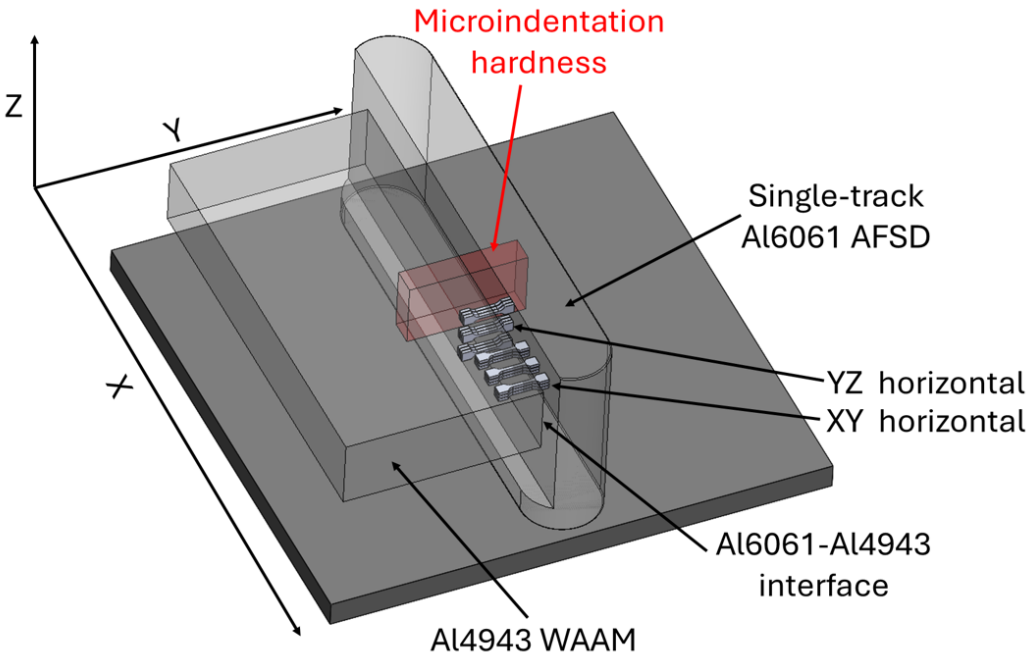


Figure 3.16: Sample extraction from the Al4943 deposited on the Al6061 machined side surface wall.

evaluated. The same microindentation hardness sample dimensions of 60 mm length, varied width, and a 12.7 mm thickness were used for both the AD and HT conditions. An example sample extraction location can be seen in figure 3.17.

3.8 Metallography

3.8.1 Metallography sample preparation

The single-track Al6061 build with Al4943 deposited on the AD AFSD top surface had metallography samples extracted in the AD and HT conditions. These were prepped according to ASTM E3-11 (81). Samples were cold mounted in an epoxy resin. Using SiC abrasive paper, the samples were ground progressively up to 1200 grit and followed by progressive polishing operations down to a 1 µm diamond suspension, providing a mirror-like finish. Polished samples were then etched with two different etchants. A pre-etch, that consisted of 1 wt% NaOH aqueous solution, was used by applying six 30 second immersions with 10 a second aeration between submersion intervals. Then Weck's color tint etch that is a mixture of potassium permanganate, NaOH and deionized water was used. This was applied with a 12 second immersion for the AD samples and a 9 second immersion for the HT samples. Etched samples in both the AD and HT conditions were evaluated using optical microscopy and SEM.

3.8.2 Optical microscopy

A Keyence VHX 7000x optical microscope was used to evaluate the grains of the metallography samples in the etched state. Images of the interface samples were stitched together to create a high resolution, high magnification mapping of the interface. Optical microscopy was used to measure the HAZ within the Al6061 material from the WAAM process. Grains in the Al6061, Al6061-Al4943 interface and Al4943 regions were captured in the AD and HT conditions from the halved MM wall that consisted of Al4943 deposited on the AD Al6061 AFSD top surface build.

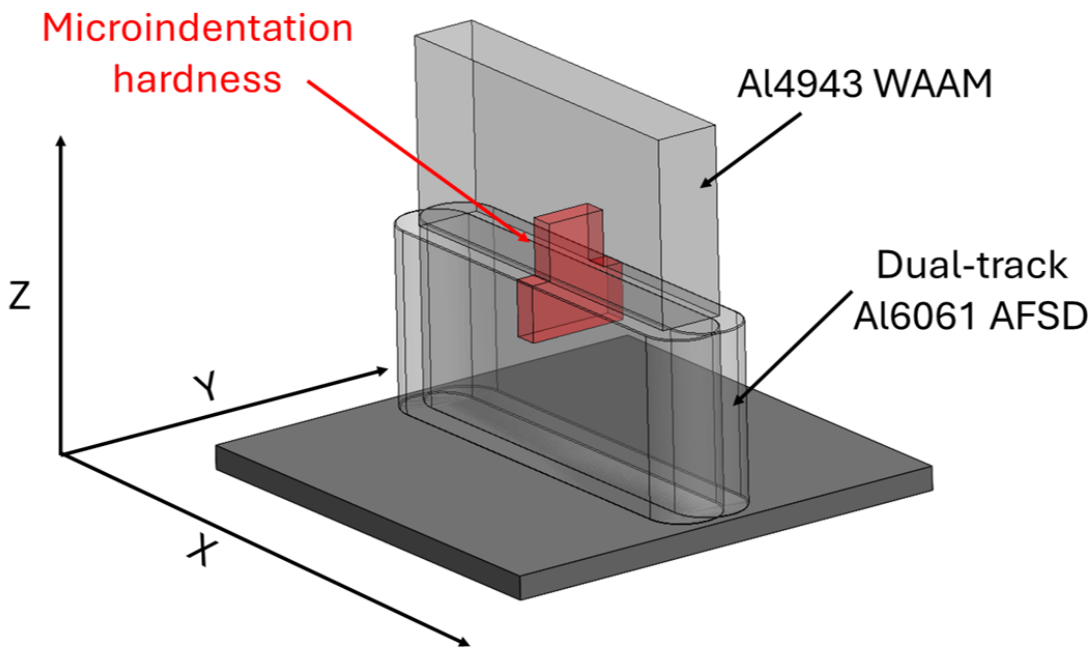


Figure 3.17: Extraction site of a microindentation hardness sample from an Al4943 deposited on the Al6061 AFSD dual-track wall.

3.8.3 Scanning electron microscopy

A Helios 5 Hydra CX SEM was used with EDS to capture the elemental composition present within the build. Metallography samples remained in the etched state, where the interface region was clearly defined to reveal the grain microstructure. The Al6061, Al6061-Al4943 interface and Al4943 regions were captured in the AD and HT conditions from the halved MM wall that consisted of WAAM Al4943 deposited onto the AD Al6061 AFSD top surface build.

3.9 Mechanical testing

3.9.1 Tensile testing

An MTS Criterion C45 with a calibrated 5 kN load cell was used for tensile testing. Each tensile specimen was placed in a shoulder grip fixture as seen in appendix A.21. A backing plate ensures that the tensile specimen was aligned along the axis of the load frame. The manufactured grips ensured consistent specimen mounting and effectively prevented slippage during tensile testing. When performing the tensile testing a crosshead speed of 1 mm/min was used, creating a strain rate of 0.00168 s^{-1}. When determining the yield properties, the strain rate does not comply with ASTM E8/E8M-20 as it is too high during measurement of the elastic regime. This makes all measured yield strength values approximate due to the higher strain rate used. In the plastic regime, the strain rate complies with ASTM E8/E8M-20 enabling true measured UTS values. The Al4943 deposited on the AD Al6061 AFSD top surface had the parent alloys' respective tensile properties measured.

3.9.2 Microindentation hardness mapping

A LECO LM248AT microindentation hardness machine was used to perform Vickers hardness testing. Sample preparation, HV microindentation hardness testing, and

HV calculations were performed according to ASTM E384-22 (82). Each sample was prepped using SiC abrasive paper. The samples were ground progressively up to 1200 grit and followed by progressive polishing using a diamond suspension down to 6 µm. A 500 gf load applied with a 10 second dwell was used to create the Vickers indentations. An optical microscope with a 10x objective was used to measure the diagonals of the indents. The HV values for microindentation hardness were then calculated from these diagonals.

Different build orientations used different mapping grid sizes. The single-track Al6061 build with Al4943 deposited on the AD AFSD top surface was measured first. This provided baseline hardness values and verified the measured HAZ found during optical microscopy. The hardness profile consisted of a 68 x 33 measurement grid with a 500 μm offset spacing between indents. The grid was centered within the sample width. Measurements were performed for the Al6061-Al4943 interface sample in the AD condition. The two other samples taken from the same build in the Al6061, and Al4943 parent alloy sections used a grid size of 75 x 5 with a 500 μm offset spacing between indents. The grid was also centered within the sample widths. The HT condition samples used a similar 82 x 5 grid and the same spacing sizes. All other single-track Al6061 samples, including the MM samples, used a 117 x 5 grid size. Hardness was mapped across the single 60 mm long sample with the same spacing and offset as seen in figure 3.18. This captured the Al6061, Al6061-Al4943 interface and Al4943 regions within the one sample. All dual-track Al6061 builds, used a single 60 mm long hardness sample. The hardness map consisted of a 60 x 13 grid size with a 3 mm spacing and 1 mm offset between indents as seen in figure 3.19. Again, the grid was centered within the sample width. For MM deposits, this captured the Al6061, Al6061-Al4943 interface and Al4943 regions within the one sample. The track overlap region within the Al6061 was also captured with the increase in grid size and spacing.

3.10 Fractography

3.10.1 Fracture analysis of tensile specimens

Fractured tensile specimens were examined using the Helios 5 Hydra CX SEM with EDS. Specimens were selected based on baseline properties and outliers found from the tensile testing data. AD and HT conditions of the Al4943 WAAM deposited on the AD Al6061 AFSD top surface MM build were evaluated within the Al6061, Al6061-Al4943 interface, and Al4943 regions. The parent alloys provide baseline properties to be compared to the interface. The interface samples were evaluated to determine failure modes and fracture morphology.

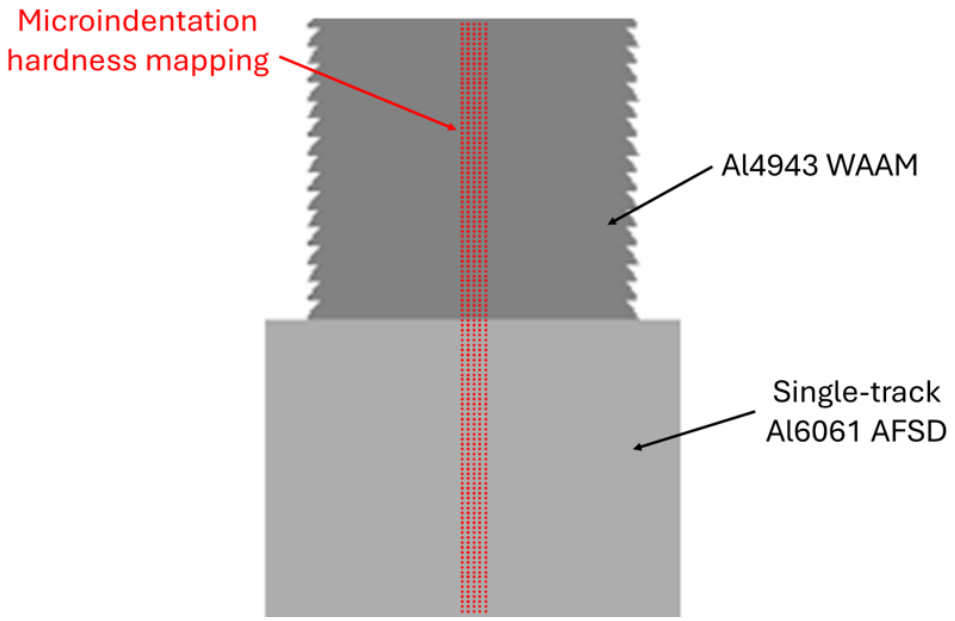


Figure 3.18: Hardness mapping across single-track AFSD 60 mm long samples using a 117 x 5 grid.

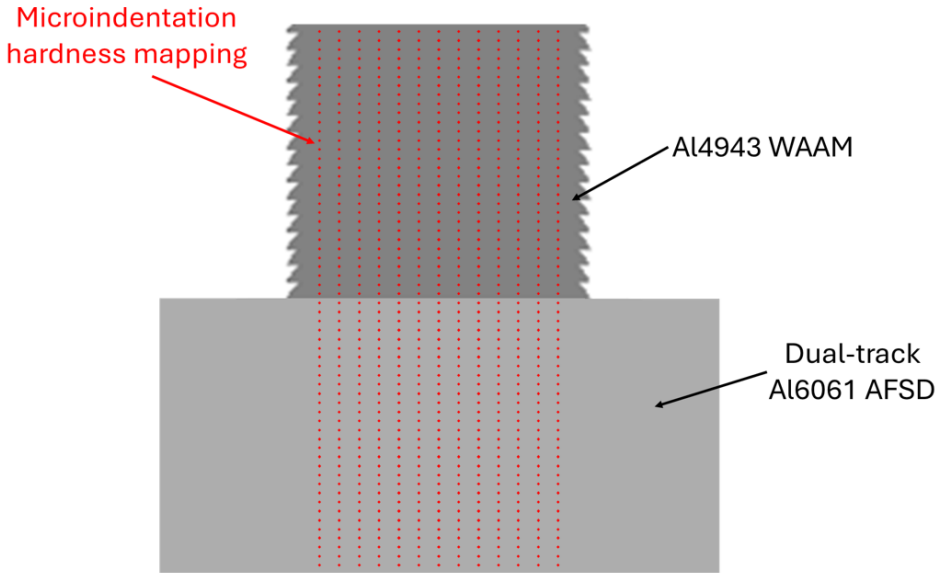


Figure 3.19: Hardness mapping across dual-track AFSD 60 mm long samples using a 60 x 13 grid.

Chapter 4

Results and Discussion

4.1 Surface roughness results

The Al6061 surface roughness was measured before Al4943 was deposited for all MM prints. Surface roughness values are provided in table 4.1 and shows that the machined surfaces have a much lower surface roughness than the top of the AD Al6061 AFSD top surface. The AFSD process creates small striations on the top surface that contribute to the rougher surface. The AD AFSD surface for Al6061 can be seen in appendix A.6, where the surface roughness is anisotropic. Striations are formed parallel to the print direction which creates surface waviness. The surface roughness is much higher in the print direction than perpendicular to it and the surface roughness for the AD AFSD surface is much higher than the machined surfaces. This is expected as the machining operations remove the striations and create a flat, smooth surface.

Surface roughness did not have a noticeable affect during Al4943 WAAM deposition. Due to the welding nature of the process, the Al6061 is intermixed in the melt pool with the Al4943 wire feedstock. The striations are turned into a liquid for a short amount of time, as the melt pool is deeper than the striation depth. The cleanliness of the surface has a greater effect as contaminants need to be removed

Table 4.1: Average surface roughness of each Al6061 surface before Al4943 deposition.

Print Condition	**Track type**	**Surface Roughness (Ra, μm)**	
		Parallel to Print Direction	**Perpendicular to Print Direction**
Al6061 AFSD AD top surface	Single-track	11.07 ± 4.91	4.41 ± 0.40
Al6061 AFSD machined top surface	Single-track	0.22 ± 0.08	–
Al6061 AFSD machined top surface	Single-track	0.21 ± 0.09	–
Al6061 AFSD machined side surface	Single-track	0.34 ± 0.16	–
Al6061 AFSD machined side surface	Single-track	0.43 ± 0.13	–
Al6061 AFSD machined top surface	Dual-track	0.22 ± 0.08	–
Al6061 AFSD machined top surface	Dual-track	0.30 ± 0.12	–

from the surface to prevent entrapment within the melt pool. The Al6061 AFSD material was cleaned appropriately and provided a fully fused interface.

4.2 Metallography results

4.2.1 Optical microscopy results

Optical microscopy of the Al4943 deposited on the Al6061 AFSD AD top surface, in the AD and HT conditions, were performed and compared. The Al6061, Al6061-Al4943 interface, and Al4943 regions were imaged to evaluate the grain structures.

In the AD condition, the Weck's etch produced good grain boundary contrast for most of the sample. However, the AFSD Al6061 region was over-etched, as contrast of the grains is lacking at various locations. This is depicted in figure 4.1, where only some grains in the different layers can be seen. A stitched image of the etched surface can be seen in appendix A.7, where the different regions within the Al6061 show the grain contrast or lack of it. Figure 4.2 shows the approximate grain size ranging from approximately 5 - 10 μm. These show fine equiaxed grains, which is expected from the AFSD process. The grain morphology is manipulated by the continuous dynamic recrystallization during the print. Fine equiaxed grains, tend to correlate with higher strength materials that have isotropic properties. However, from the AFSD process, a higher ductility deposit, is expected. The fine equiaxed grain structure captured here follows the same trends seen in other work of Al6061 deposited via AFSD (35).

The AD WAAM Al4943 grain structure can be seen in figures 4.3, 4.4 and appendix A.8. A stitched image of the Al4943 WAAM surface in the AD condition can be seen in appendix A.9. There are columnar-like grains in the build direction present throughout the bulk of the material. Reheated zones from the bead overlap regions have some grains directed towards the next bead in the planned path. However, most of the grains are directed towards the next layer that was deposited, enforcing the growth in the build direction. Dendrites are seen within each bead, and measure up

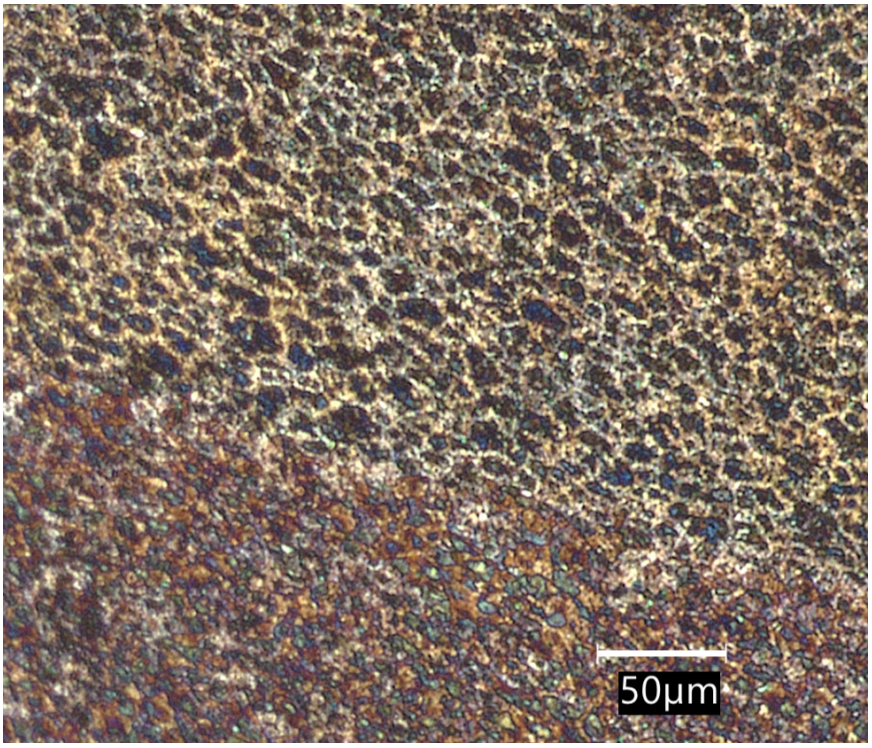


Figure 4.1: Etched Al6061 deposited via AFSD in the AD condition.

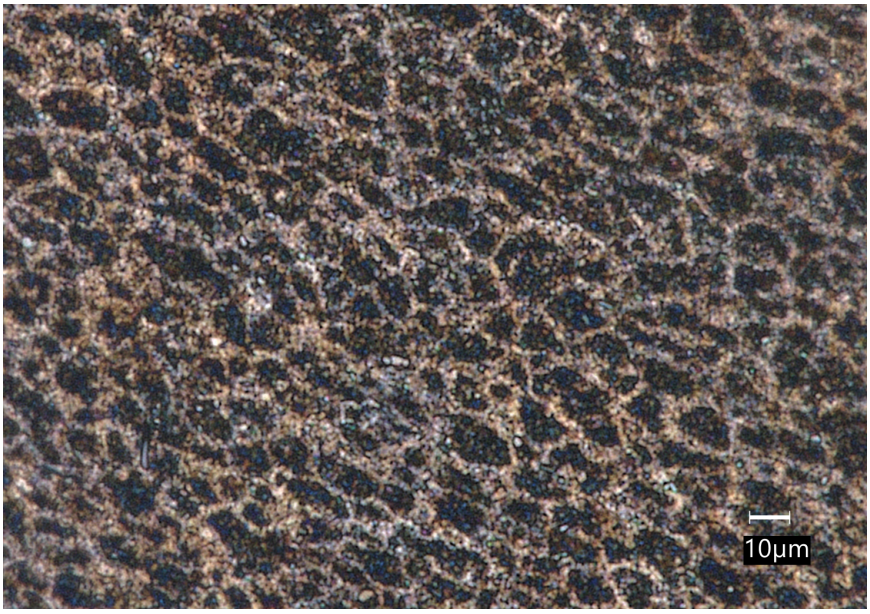


Figure 4.2: Grain size within the AD Al6061 deposited via AFSD, measuring approximately 5 - 10 μm.

to approximately 100 μm in length and vary in width. Grain growth in the build direction, usually creates anisotropic behavior. Fewer grain boundaries interrupt dislocation motion, creating a higher ductility, lower strength material in the build direction. The grain morphology seen here, follows trends found in Al4043 and Al4943 WAAM and welding literature. Specifically, where the dendritic formations are seen to be elongated towards the build direction (17; 67; 70; 73).

Porosity is present within the AD Al4943 region where the largest pores measured about 100 μm in diameter. They are present along the bead overlap regions as well as within individual beads and are scattered throughout the Al4943.

The Al6061-Al4943 interface in the AD condition was captured and the HAZ in the Al6061 region was measured. Micro-images at 300x magnification were stitched together to create a macro-image of the interface. This is shown in appendix A.10 where the bottom is Al6061 and the top is Al4943. The center Al4943 WAAM bead is evaluated in figure 4.5. It can be seen that the Al4943 region maintains columnar grain growth near the interface, and Al6061 maintains a relatively fine equiaxed grain growth. The Al6061 region is altered from the heat input during Al4943 deposition. This created a HAZ that allowed grain growth within the Al6061 near the interface. This is shown in figure 4.6, where the region near the interface has coarser grains than the region farther away.

The HAZ measures about 150 μm into the Al6061 region. The grains in the Al6061 region directly below the interface are seen to have maintained an equiaxed structure, but grew slightly from their initial AD structure. This was expected as the heat input from the WAAM process will enable grain growth, creating the HAZ. After 150 μm into the Al6061 the grains can be seen to become finer. The HAZ has grains measuring about 10 μm, while the finer grains are roughly half, at about 5 μm.

The Al4943 region along the interface shows dendritic formation where the grains are growing in the build direction. However, directly at the interface, larger equiaxed grains are present, where some dilution between the materials may also be present.

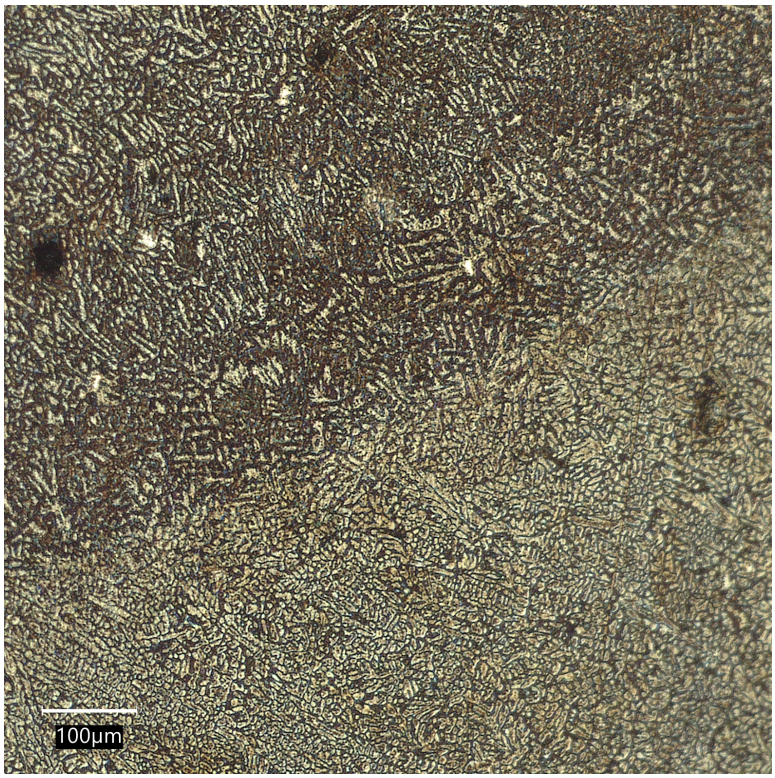


Figure 4.3: Grain structure of a bead overlap region from an Al4943 WAAM deposit in the AD condition.

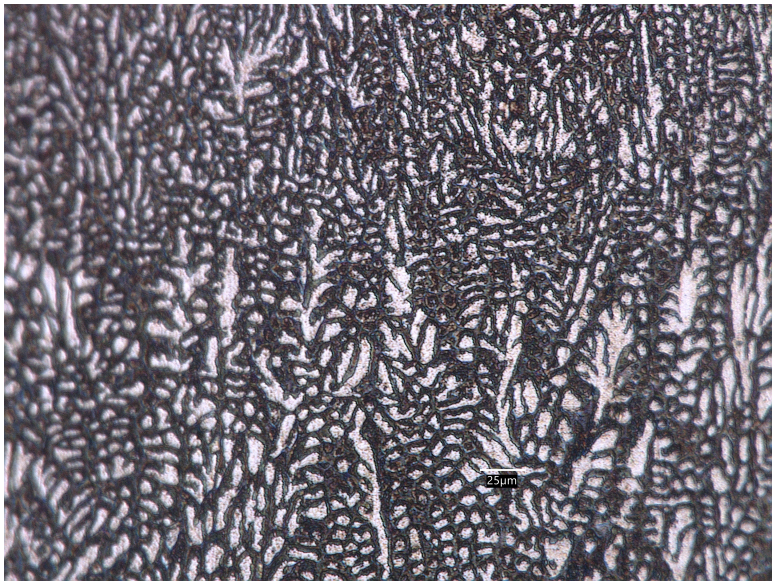


Figure 4.4: Higher magnification of the grain structure of Al4943 deposited via WAAM in the AD condition.

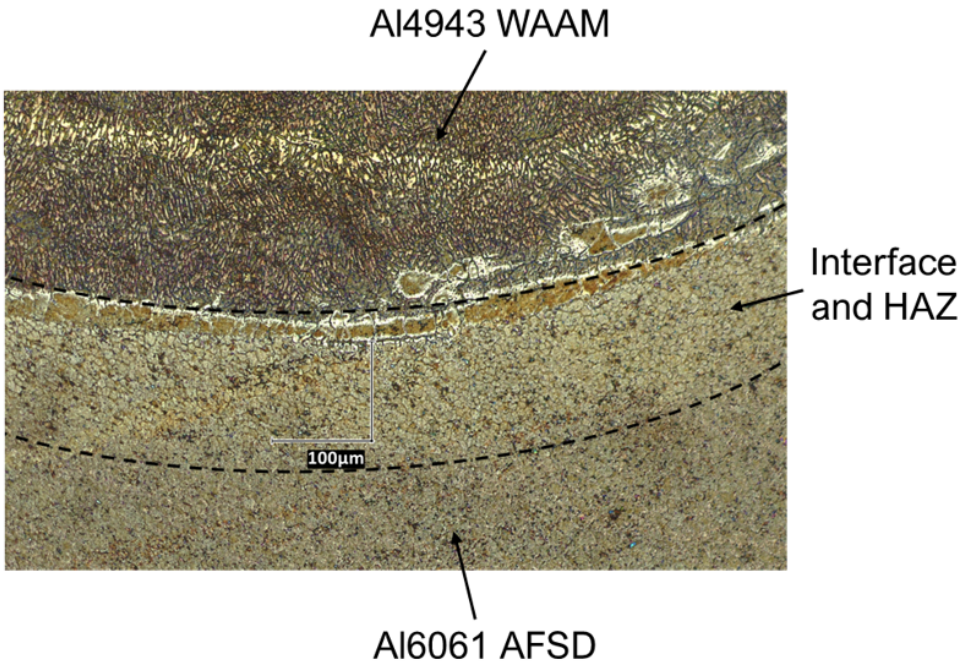


Figure 4.5: HAZ into the AD Al6061 AFSD from the Al4943 WAAM.

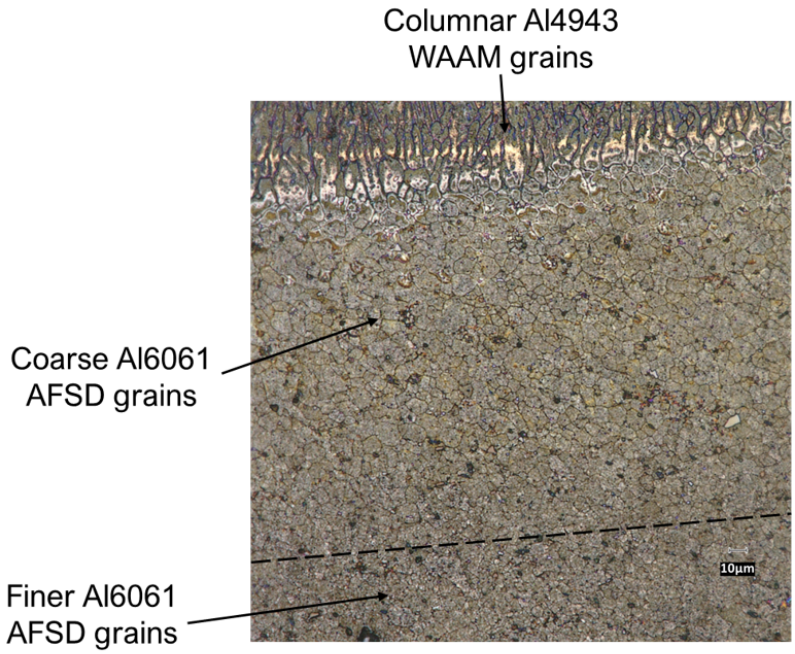


Figure 4.6: Grain structure near the Al6061-Al4943 interface in the AD condition.

The Al4943 columnar-like grains near the interface measure roughly 20 to 30 μm along the build direction but only about 5 - 10 μm in width.

In the AD condition, the Al6061 AFSD material was affected by the sequential WAAM process, creating a HAZ measuring about 150 μm into the Al6061. This seems to have encouraged grain growth with larger grains present in this area. Grains below the HAZ within the Al6061 were not seen to be affected. The grain structure within the Al4943, depict a dendritic structure that grew in the build direction. This is replicated at the interface as well. However, larger equiaxed grains are present directly at the interface, which may be due to dilution between the two materials or may be Al6061 with continued grain growth from the WAAM heat input. The HAZ should not affect the performance of the material, as this is an inherit characteristic of the WAAM process.

In the HT condition, the Weck's etch did not perform as well in the Al6061 region where only certain regions provided contrast at the grain boundaries. The stitched image in appendix A.11 shows how most of the sample lacks contrast. The interface sample provides better grain contrast in the Al6061 region, which is provided in figure 4.7. This region was captured well within the Al6061 bulk material. The grains can be seen to remain as a fine equiaxed structure. They measure roughly 10 μm and exhibit some grain growth compared to the AD condition.

In the HT Al4943, the grains are mostly dendritic, but some regions near the bead overlaps have a relatively equiaxed structure, figure 4.8. Where dendrites are present, they tend to grow in the build direction, following the trend in the AD condition. Porosity is still present in the HT condition and has sizes similar to those in the AD condition. The stitched image is shown in appendix A.12.

Along the Al6061-Al4943 interface, the grains in both materials and their interface are distinct and discernible. Figures 4.9 and 4.10 show the interface with Al6061 on bottom and Al4943 on top. Al6061 grains can be seen to maintain a fine equiaxed grain structure, whereas the Al4943 maintained a columnar-like grain structure

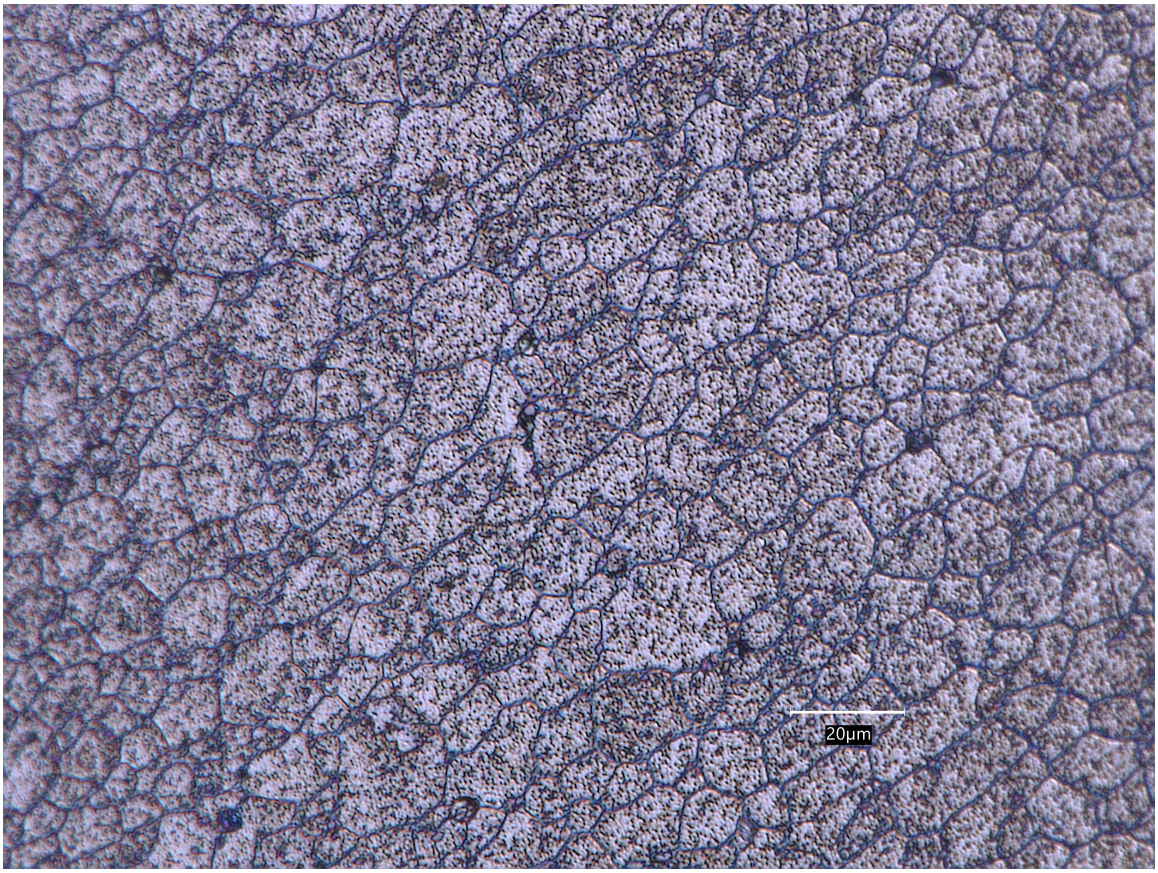


Figure 4.7: Grain structure of an Al6061 AFSD deposit in the HT condition.

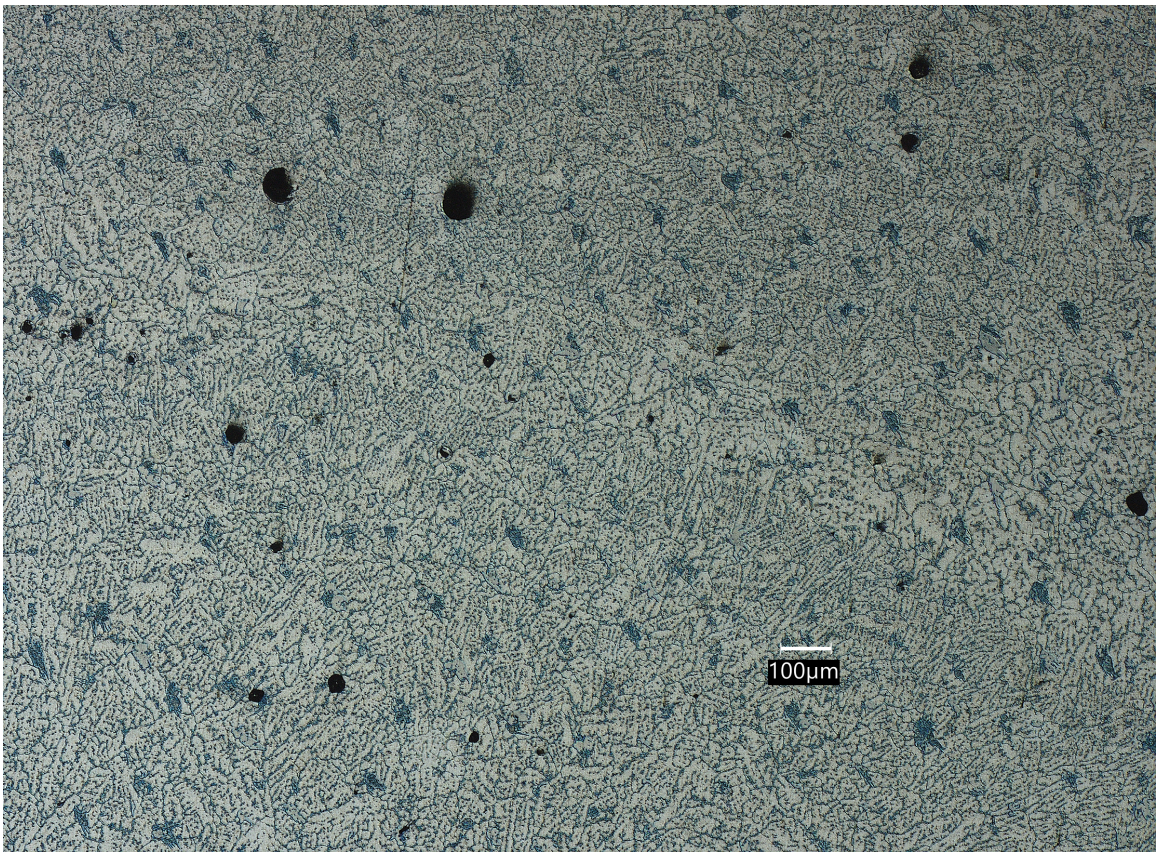


Figure 4.8: Grain structure of an Al4943 WAAM deposit in the HT condition.

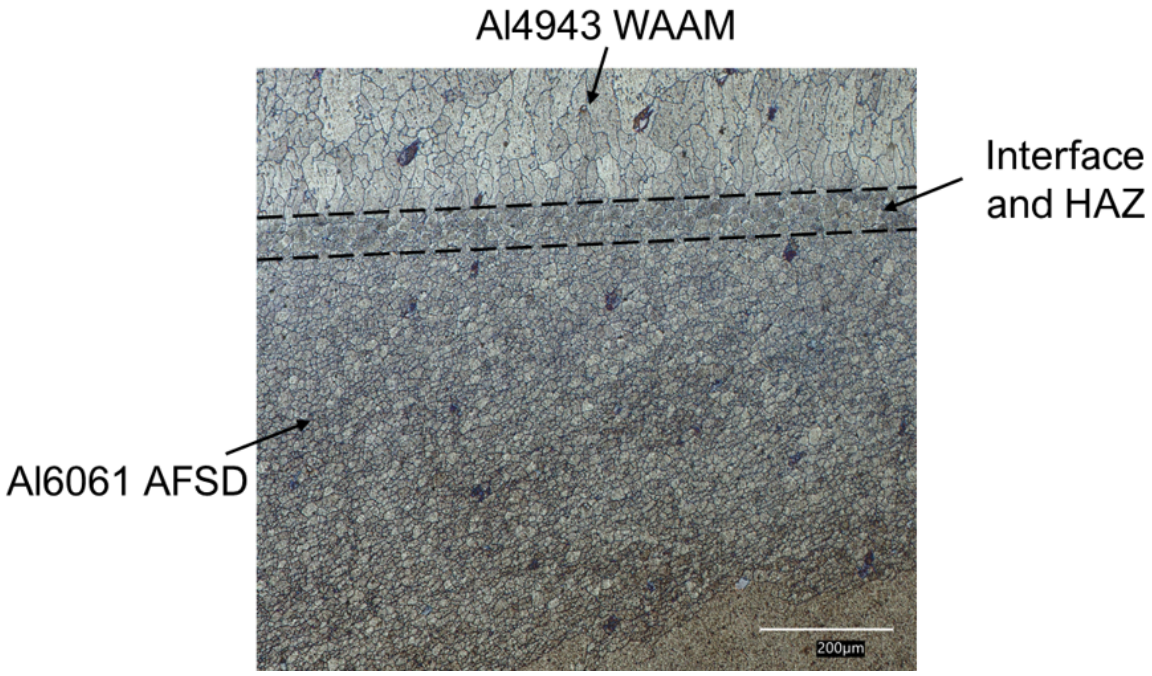


Figure 4.9: Grain structure near the Al6061-Al4943 interface in the HT condition.

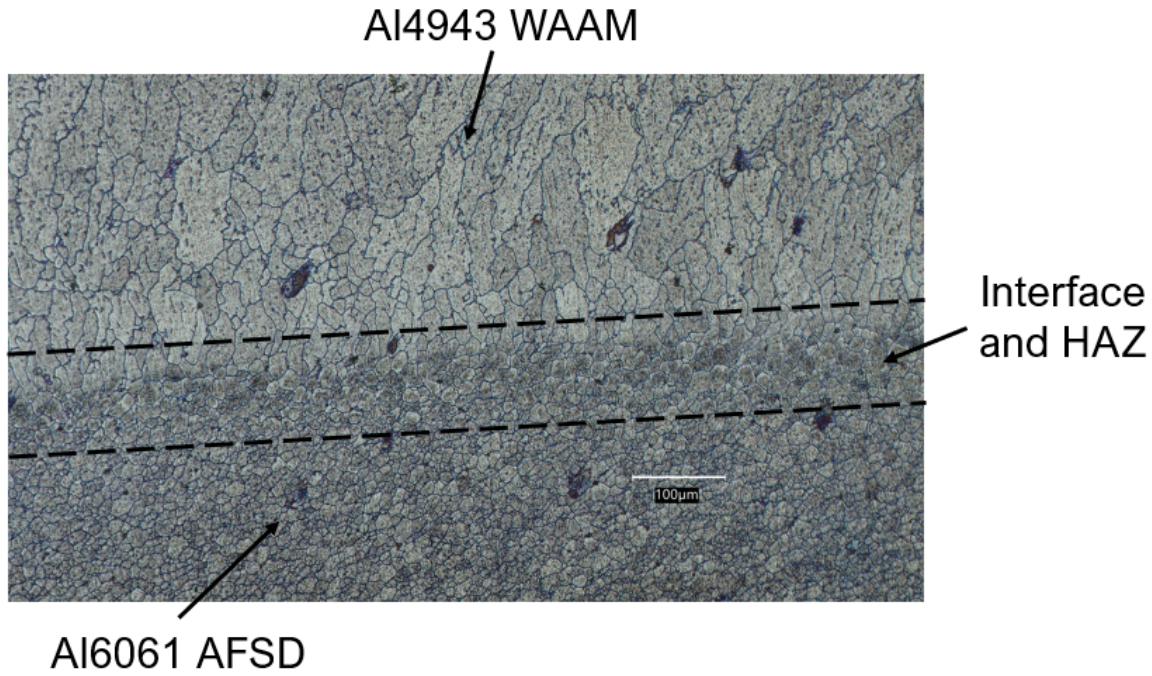


Figure 4.10: Grain structure near the Al6061-Al4943 interface in the HT condition at 300x magnification.

directed in the build direction. Larger grains are present directly at the interface where the two materials meet. These seem to have maintained grain growth in the HT condition, as they were in the AD condition. A dilution area appears to be present at the interface, where the two materials have intermixed, due to the WAAM process. The grains observed at the interface are not replicated in either of the parent Al6061 or Al4943 regions. Dilution could be affected by the partially melted zone (PMZ), created from fusion welding processes. This is displayed within welding literature, where the PMZ is present between the fusion zone and the unaffected base material. It is usually much smaller than the weld bead width and contains composition changes throughout (83). This is displayed at the Al6061–Al4943 interface, as compositional intermixing is illustrated. This was evidenced by the presence of porosity, from the WAAM process, within the transition zone. The transition of materials, along the build direction, is much smaller than the bead width, creating a relatively discrete interface between the two materials. The Al6061 has equiaxed grains and Al4943 has columnar-like grains due to their respective additive processes that were maintained in the HT condition.

4.2.2 Scanning electron microscopy results

Elemental composition of the parent alloys and the interface regions were examined through SEM equipped with EDS. A qualitative analysis was performed for the AD and HT condition for all three regions of the build. The Al6061 and Al4943 regions are compared to the Al6061-Al4943 interface regions in both conditions. Aluminum, silicon, magnesium, and iron are of elemental focus, as these contribute to strengthening and/or weakening of the material in both alloys. All samples were evaluated in the etched state to provide a distinct interface where the materials join.

In the AD condition, an Al6061 AFSD sample is evaluated. Figure 4.11 shows fine equiaxed grains in an α-Al microstructure. Constituents in the form of cluster and needle-like formations are scattered throughout the sample, near grain boundaries.

EDS shows that some of these intermetallics are heavily concentrated with iron and silicon. The iron rich intermetallics are mostly identified in the needle-like formation, indicating that the β-AlFeSi phase may be present. The presence of this intermetallic can promote brittle failure and reduce the mechanical strength of the material. Iron-rich intermetallics are found in other Al6061 AFSD studies, where mechanical properties did not reach desired values (36). Clusters of silicon and magnesium are also present within the Al6061, which may be attributed to coarse Mg_2Si intermetallics. These clusters are larger in the AD condition than in the HT condition due to the overaging effect during the AFSD process that enables precipitates to grow. The mechanical performance of the AD Al6061 is expected to be reduced relative to the feedstock, as precipitate coarsening and overaging diminish the strengthening mechanisms of the alloy. The fine equiaxed grains in the deposit are not coupled with the strengthening mechanisms, thus weakening the material. This effect was observed in other Al6061 AFSD studies (51). The β'' strengthening precipitate was not found within the AD condition of Al6061.

Evaluation of Al4943 in the AD condition showed a dendritic microstructure that was also observed in the optical microscopy. High concentrations of silicon with some magnesium are segregated to the grain boundaries. The solubility of the elements influences the segregation observed. Lower solubility elements tend to segregate more, due to the solidification trends in the WAAM process. The Al-Si eutectic is observed along the grain boundaries and is verified in the elemental mapping seen in figure 4.12. The α-Al eutectic is found in the interior of the grain boundaries. The segregation of silicon at the grain boundaries, tends to result in reduced tensile properties. Intergranular fracture can occur at the weakened grain boundaries. The microstructure observed is common in Al4043 WAAM, which is similar to Al4943 WAAM (17; 70).

The Al6061-Al4943 interface in the AD condition shows a fairly discrete boundary between the two materials, as seen in figure 4.13. The interface region has similar findings as the two parent alloys. Within the Al6061 region, a refined α-Al matrix

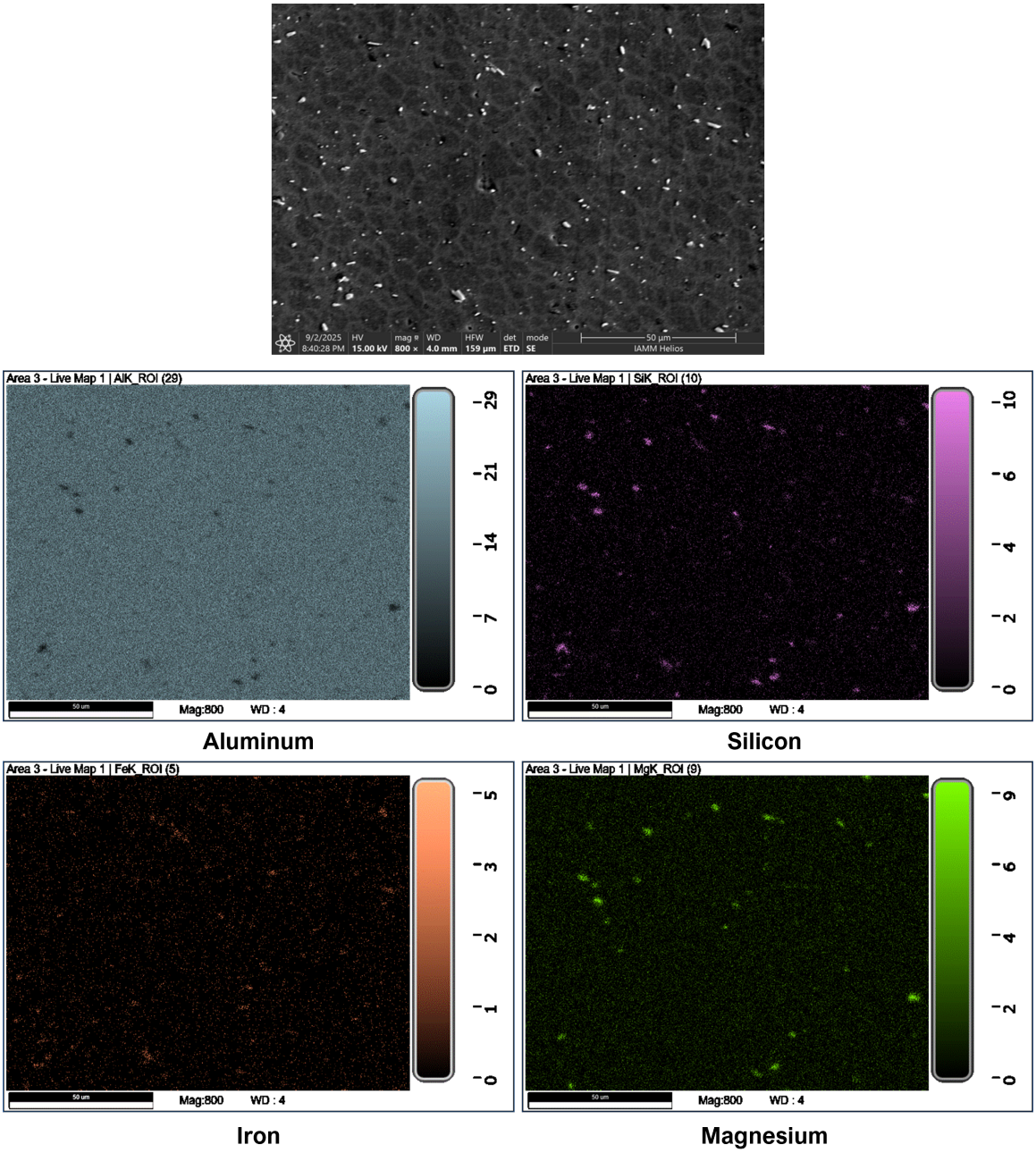


Figure 4.11: SEM with EDS images of Al6061 material deposited via AFSD where iron-rich intermetallics are present.

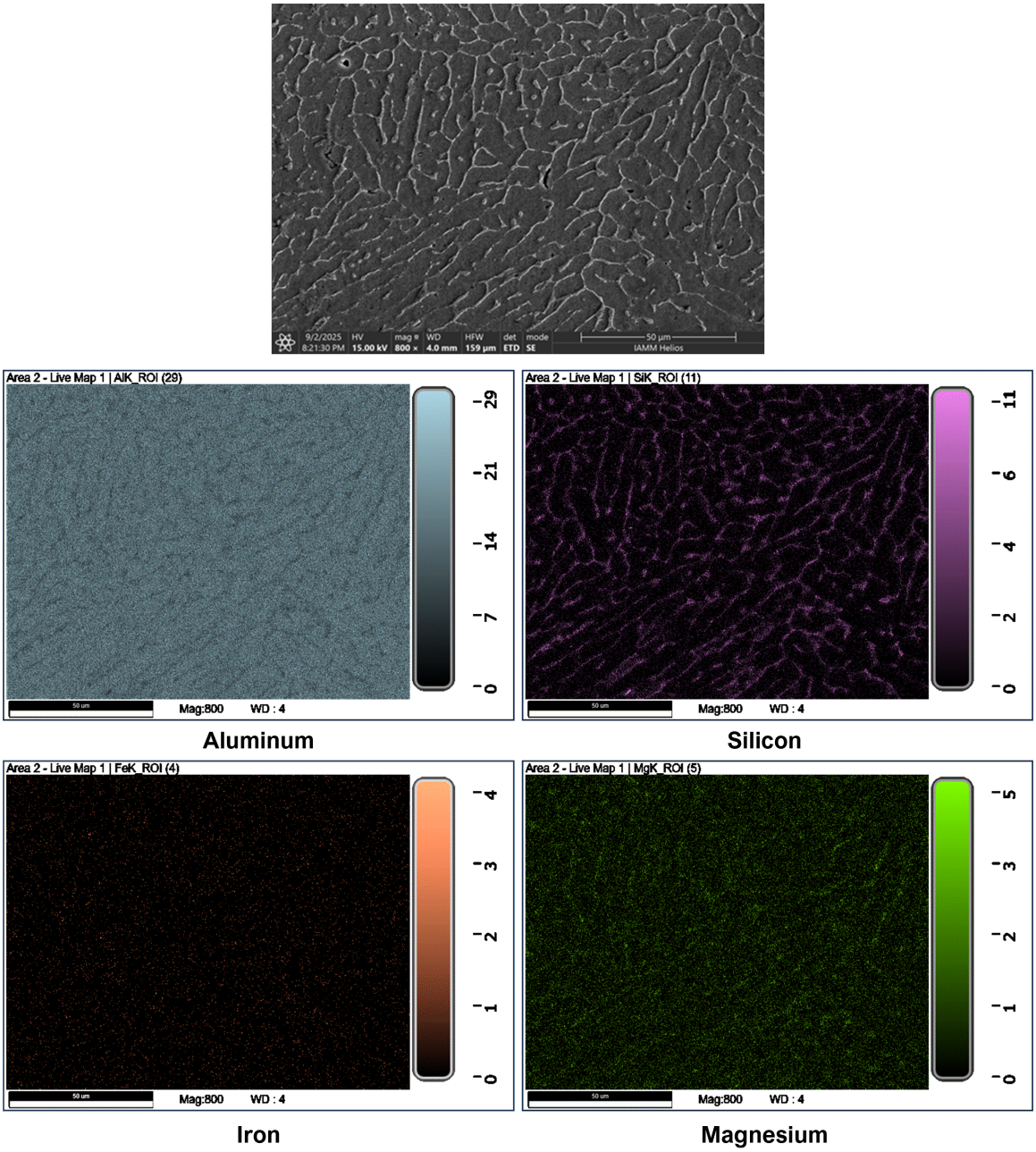


Figure 4.12: SEM with EDS images of Al4943 material deposited via WAAM where high concentrations of silicon are located at the grain boundaries.

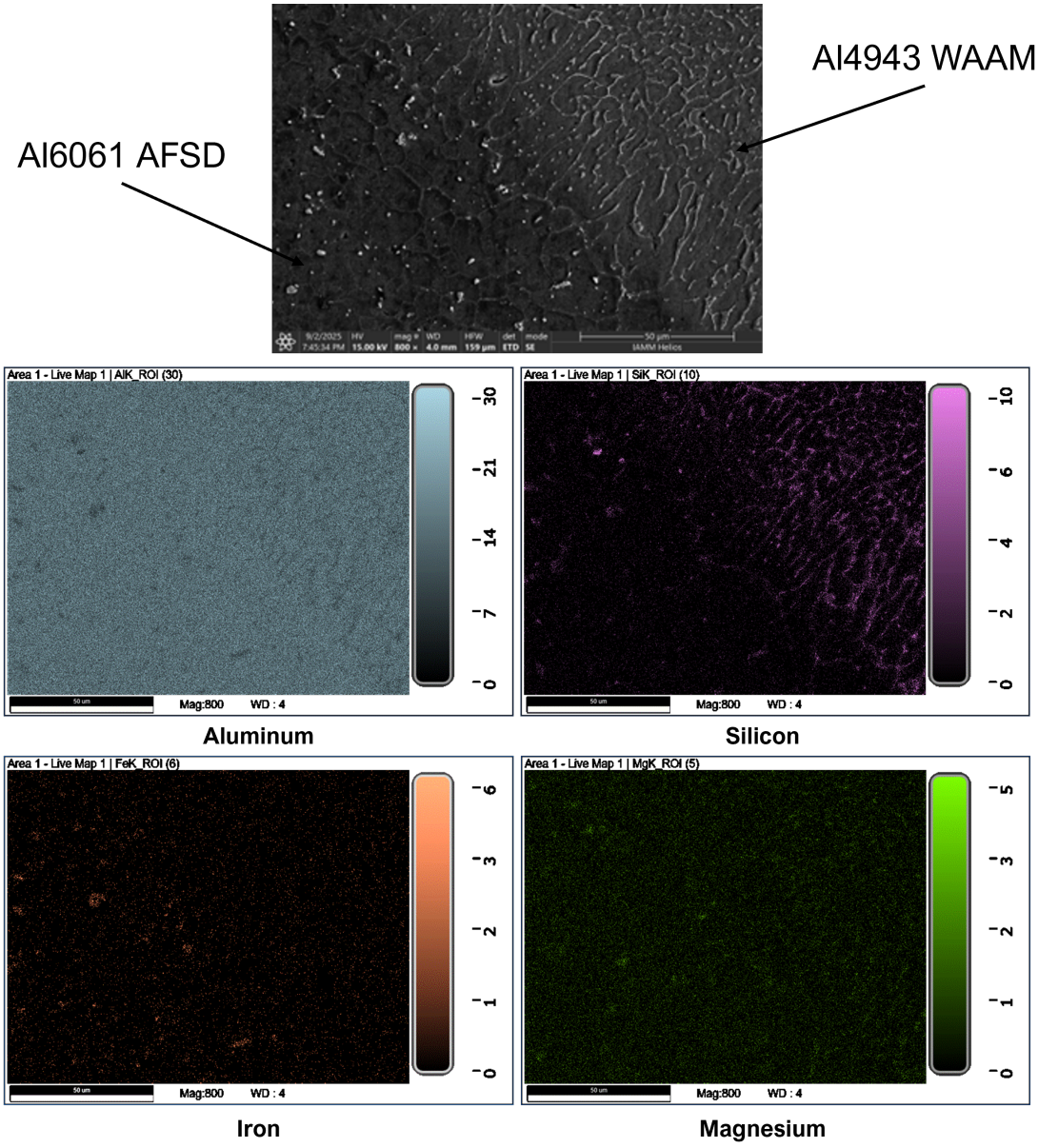


Figure 4.13: SEM with EDS images of Al6061-Al4943 interface deposited via AFSD and WAAM.

exists due to the dynamic recrystallization from the AFSD process. Iron-rich intermetallics are located near the grain boundaries along with Mg_2Si clusters. The Al4943 region continues to have high concentrations of silicon segregated out at the grain boundaries, indicating that the Al-Si eutectic is present. Magnesium is scattered throughout both materials with some segregation at grain boundaries. There is minimal dilution between the alloys as some of the silicon content from the Al4943 may be present in the Al6061 at the interface. A difference in microstructure exists between the Al6061 and Al4943. A concentrated α-Al matrix is present in the Al6061 and an Al-Si eutectic in the Al4943. These are characteristics of the solid-state and fusion-based processes used. The interface region presents minimal cause for concern, as no significant defects are present. The distinct compositional transition, indicates limited mixing of the alloys with a well fused interface.

In the HT condition all three regions are evaluated and seen in figures 4.14, 4.15 and 4.16. An etched Al6061 sample can be seen in figure 4.14. Grain boundaries are unable to be identified within the image as contrast is lacking due to the etchant. Silicon and magnesium clusters are present, but it is unknown whether they are segregated out of the grain boundaries. These clusters could be forms of Mg_2Si that were precipitated during the aging process from the HT schedule. A uniform α-Al matrix is depicted throughout with clear precipitates. Fine needle-like β" was not seen in either the HT or AD condition, that wrought Al6061-T6 tends to have. TEM techniques may need to be used, due to the nano-scale size of these precipitates. In other studies, a lack of β" was observed, where Al6061 AFSD in the AD and HT condition was evaluated (51). There are also iron-rich intermetallics present in the HT condition that are shown in appendix A.13. The intermetallic seems to be the same β-AlFeSi phases present in the AD condition. The HT condition provides a uniform α-Al matrix, that could have some strengthening precipitates, unlike the AD condition. The uniformity in the HT condition can provide mechanical benefit, by promoting isotropic behavior. It is expected that the HT condition improved the mechanical properties and the uniformity observed, indicates that as well.

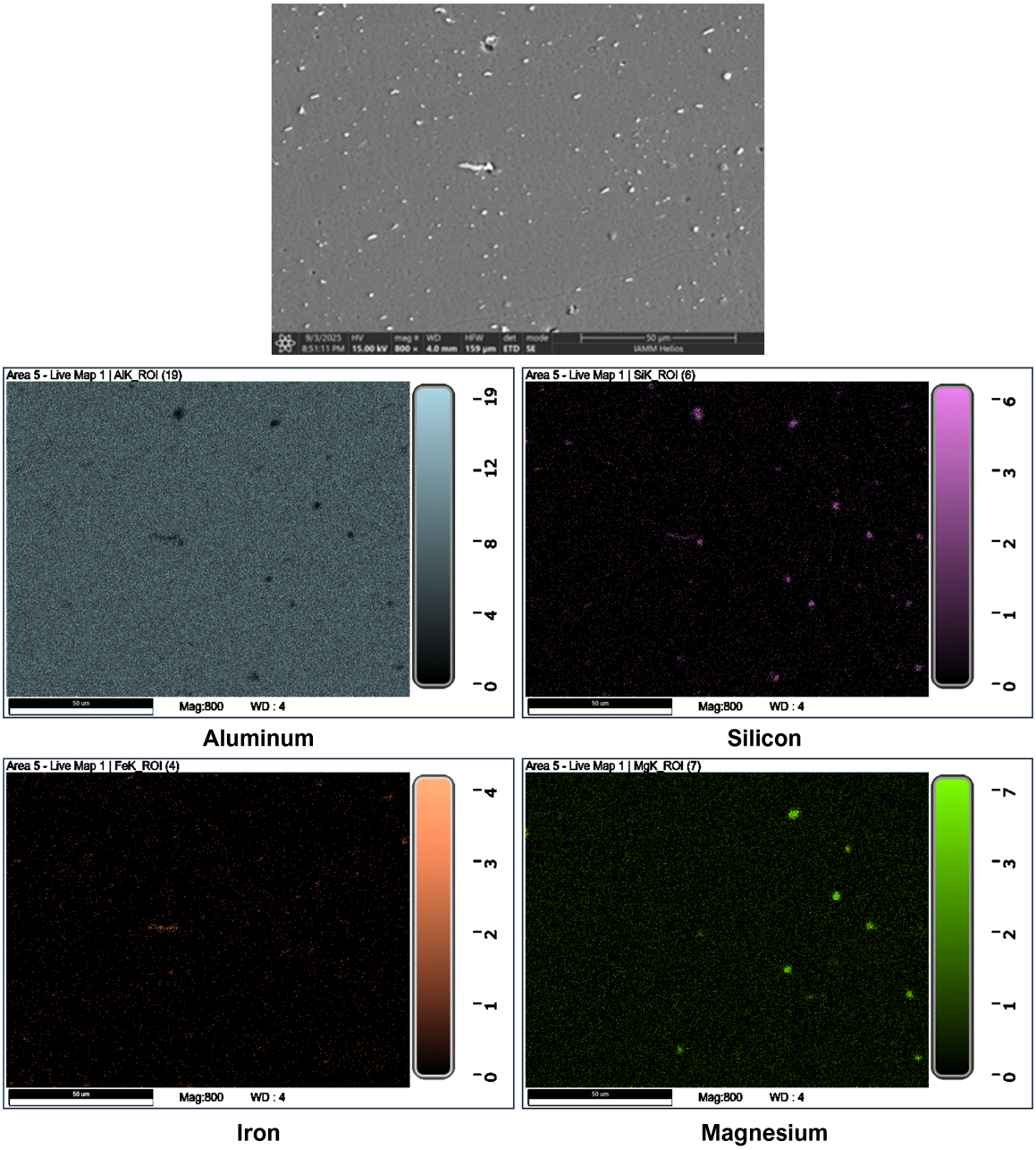


Figure 4.14: SEM with EDS images of Al6061 deposited via AFSD post HT process.

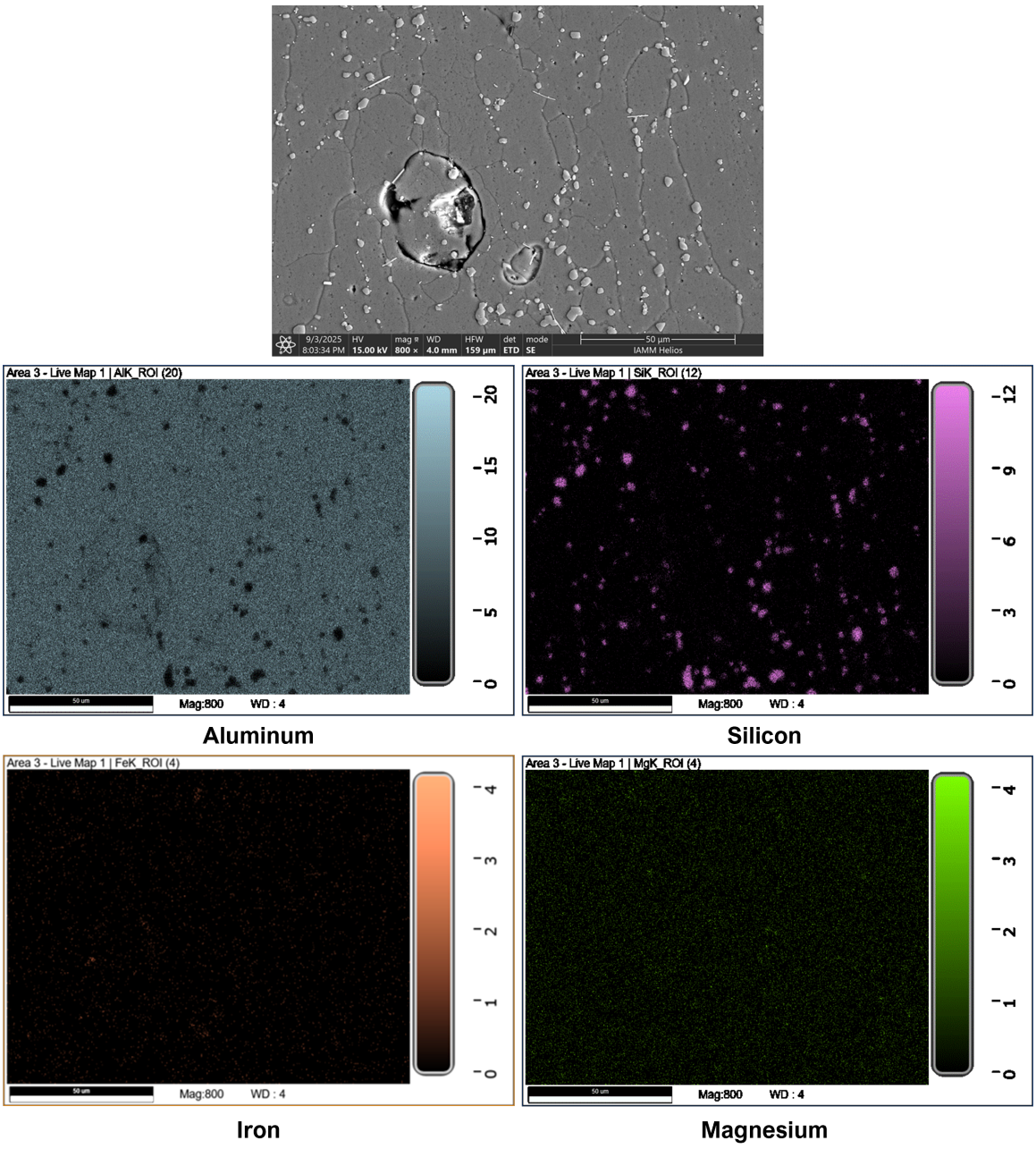


Figure 4.15: SEM with EDS images of Al4943 deposited via WAAM post HT process.

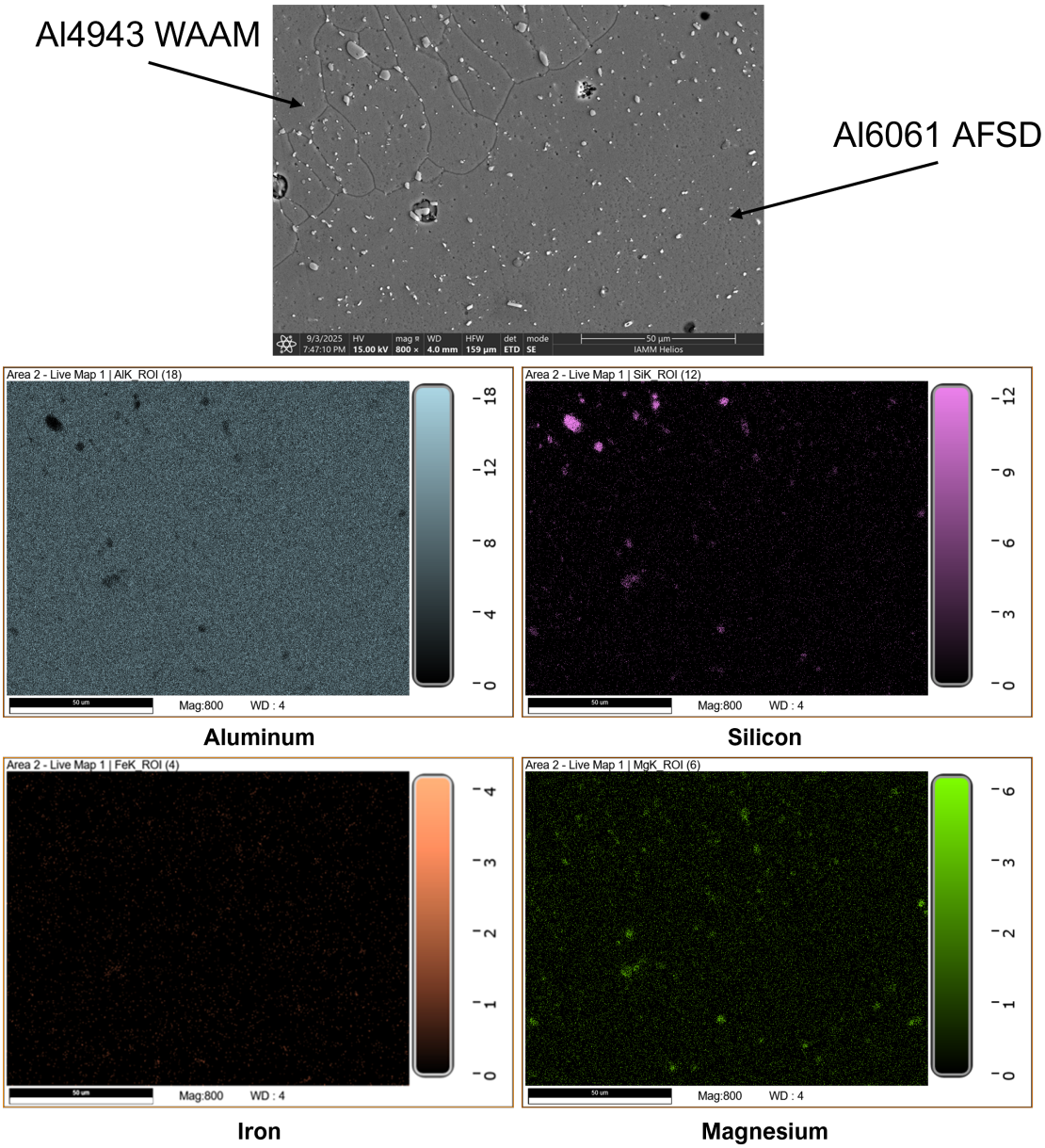


Figure 4.16: SEM with EDS images of Al6061-Al4943 interface deposited via AFSD and WAAM post HT process.

The Al4943 in the HT condition shows a high composition of aluminum, silicon and magnesium as seen in figure 4.15. Instead of a dendritic microstructure, that was observed in the AD condition, clusters of silicon are present along the grain boundaries. The spherical shape of silicon, instead of the Al-Si dendritic structure, helps improve mechanical properties (84). Magnesium content is uniformly distributed throughout the sample. Some iron-rich intermetallics remain in the deposit. A lack of β" was observed. Again, other metallography techniques such as TEM may be needed to observe nano-scale precipitates.

The Al6061-Al4943 interface in the HT condition can be seen in figure 4.16. The HT condition shows an evolution in microstructure compared to the AD condition for both parent alloys and at the interface. Compositional contrast is less severe in the HT condition as both alloys exhibit a uniform structure. The Al6061 region presents clusters that could be attributed to Mg_2Si precipitation. The Al4943 has spherical silicon particles instead of the dendritic microstructure. This creates a more uniform transition between the materials. There is some dilution present, as the porosity along the interface appears to be near the Al6061 region. However, the porosity content is attributed to the WAAM process. This exhibits a dilution zone or PMZ that was also seen in the optical microscopy of the HT samples. The two materials can be seen to have different compositions, that are more uniform in the HT condition than the AD condition. The interface is distinguished by the composition but is not as clear as it was in the AD condition. This is representative of a HT condition that improved mechanical properties across the deposit, including the interface.

4.3 Mechanical testing results

4.3.1 Microindentation hardness results

Microindentation hardness profiles were performed on each deposit. The parent alloys, deposited with their respective additive process, were measured to obtain

their nominal hardness values. These are compared to the hardness measured across the MM interfaces. Single-track and dual-track Al6061 AFSD deposits in the AD and HT condition are both measured. Al4943 WAAM deposits in the AD and HT condition are measured as well.

4.3.2 Parent alloy microindentation hardness results

The single-track and dual-track Al6061 AFSD hardness in the AD and HT condition can be seen in figure 4.17. For both track types, in the AD condition, the hardness can be seen to increase in the build direction. This trend is expected and has been noted in other studies of AFSD builds. It is found that the repeated thermal cycling during the AFSD process creates an overaging effect that decreases the hardness (35; 52). The top layers of the Al6061 AFSD region have an increased hardness as they are not subjected to the thermal cycling. The maximum hardness is measured within the top layer of the deposit. The bulk hardness is about 42 HV, increasing progressively from about 30 mm below the surface to approximately 53 HV at the top layer for both deposits. The single-track and dual-track follow the same trend in the AD condition.

In the HT condition, both deposits can be seen to have an overall increase in hardness. A decrease in hardness can be seen near the bottom edge for the single-track HT deposit, however this is due to inadequate polishing at the edge of a relatively large sample. This creates bias when measuring the indents as a distinct indent edge is not identified during hardness testing. This is seen in other samples as well and can be neglected from the data. The hardness is relatively uniform throughout the sample which aligns with expected trends after HT (36). The average hardness for the single-track and dual-track HT deposits are approximately 110 ± 10.5 HV and 115 ± 4.8 HV. The edge effects due to polishing are neglected and average values are measured from -50 mm to -10 mm from the top of the deposit. The variability in the single-track deposit is higher, however there is no significant difference observed

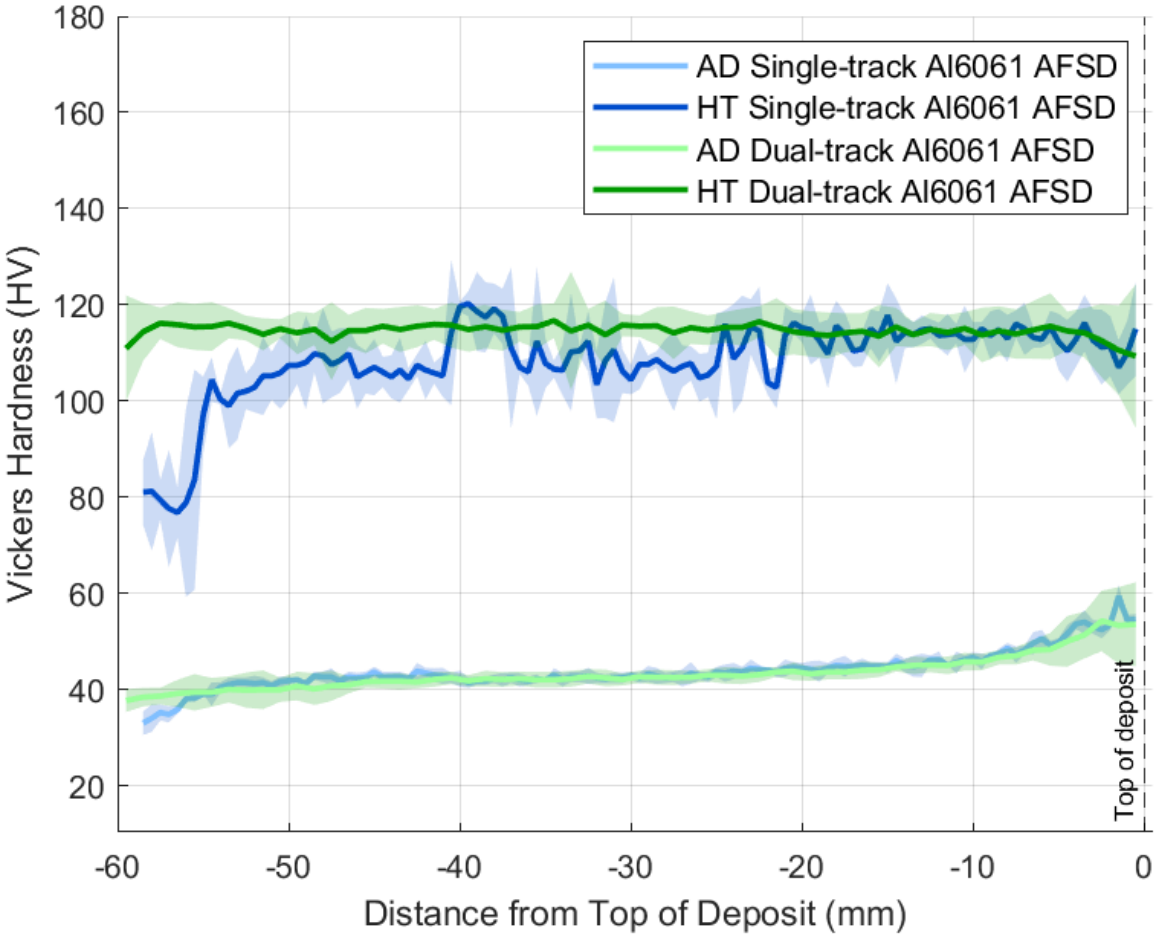


Figure 4.17: Microindentation hardness across single-track and dual-track AD and HT Al6061 AFSD samples.

between the single-track and dual-track hardness. Both conditions follow the same trends at about the same value, enabling multi-track deposition using AFSD.

The hardness measured throughout the Al4943 WAAM deposition follows the same trend as the Al6061 deposited via AFSD for both the AD and HT conditions. This can be seen in figure 4.18. In the AD condition, the bulk hardness is about 50 HV, increasing progressively from about 30 mm below the surface to approximately 75 HV at the top layer for both deposits. This trend aligns with findings in the Al6061 deposited via AFSD because they are both age hardening alloys. They both endure thermal cycling, due to their respective processes. An overaging effect seen from the AFSD process is replicated in the Al4943 WAAM. Native to the Al4943 WAAM, a decrease in hardness is present along the bead overlap regions as seen in figure A.14. In the HT condition, the average hardness is relatively uniform throughout the build. The decrease in hardness at the ends of the sample are due to the inadequate polishing at the edges. Disregarding the edge effects, the average hardness measured with two standard deviation, within the stable region of -50 mm to -10 mm from the top of the deposit, is about 105 ± 5.8 HV. The uniform increase in hardness is expected as the HT condition artificially ages the material, potentially enabling strengthening mechanisms and depleting the overaging effects. Similar results were seen in Al4943 welding studies, where the HT condition increased hardness uniformly (61). Both the Al4943 and Al6061 follow the same trends where the hardness in the AD condition increase in the build direction and a T6 HT condition creates a homogeneous material with increased hardness. Appendix A.1 compares the hardness between the parent alloys in the AD and HT condition.

4.3.3 Multi-material microindentation hardness results

For the Al6061-Al4943 MM an understanding of the HAZ through microindentation hardness testing was established. This included testing of the sample that printed Al4943 on the AD Al6061 AFSD surface. The microindentation hardness was mapped

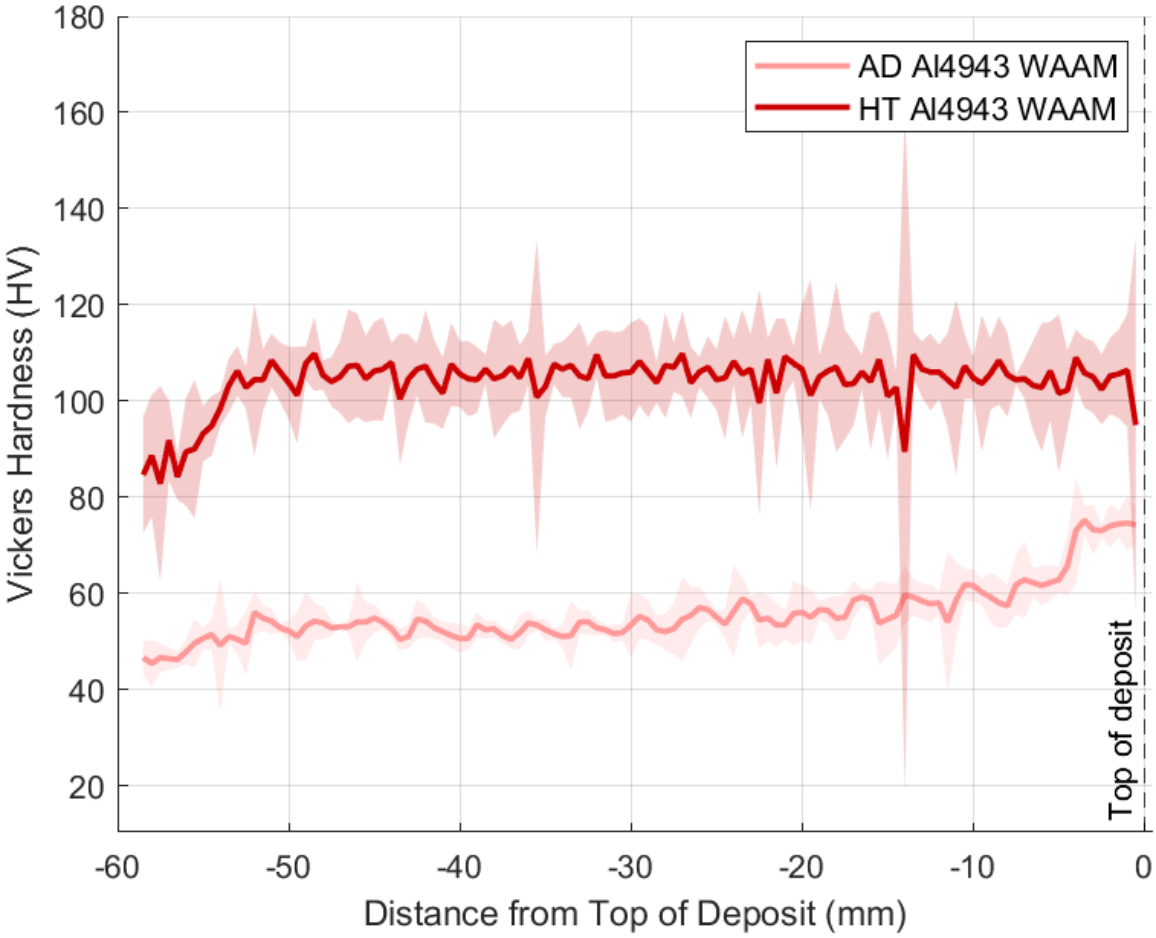


Figure 4.18: Microindentation hardness across an AD and HT Al4943 WAAM sample.

on the sample and can be seen in figure 4.19. Figure 4.20 shows the HV values measured throughout the deposit where the bulk printed material of each region was compared to the interface region.

The average hardness of each alloy was measured in the interface sample and compared to the parent alloy samples. The Al6061 region had an average hardness of about 40±1.5 and the Al4943 WAAM region was about 52±5.4 HV. This is consistent with the hardness measured in each parent alloy sample and provides clarity that the HAZ within the Al6061 resides within 40 mm of the top of the AFSD deposit. At the interface, the maximum hardness is found where the two materials are joined together. The overaging effect from the AFSD process allows for the peak hardness to be located at the top layer of the deposit, where the first layer of the WAAM process is deposited. The increasing hardness in the build direction, seen in the Al6061, is replicated in the MM. This indicates that the HAZ is minimal which correlates with the optical microscopy results.

In the HT condition, the Al6061-Al4943 interface is distinct as the hardness decreases directly across the interface as seen in figure 4.21. In the HT Al6061 region, the average hardness is approximately 113 ± 11.2 HV and the HT Al4943 region is 103 ± 12.3 HV. These average hardness values are consistent with the HT parent alloy samples. A decrease in hardness is seen in the Al4943 region, located at 22 mm from the interface. This is due to edge effects from the sectioning of samples from the set. The edge effects are omitted in the averaging of the hardness. The hardness across the interface correlates with the hardness of the respective alloys, creating a distinct hardness boundary where the two materials are joined.

The average hardness across all the MM deposits that utilized a single-track Al6061 AFSD deposit are plotted against one another in figure 4.22. The average of the measurements along with their associated variability, expressed as two standard deviation can be seen in appendix A.15. The trends seen previously, in the AD and HT conditions, are seen again here. For all deposits, in the AD condition, the Al6061 can be seen to have an increase in hardness in the build direction. This

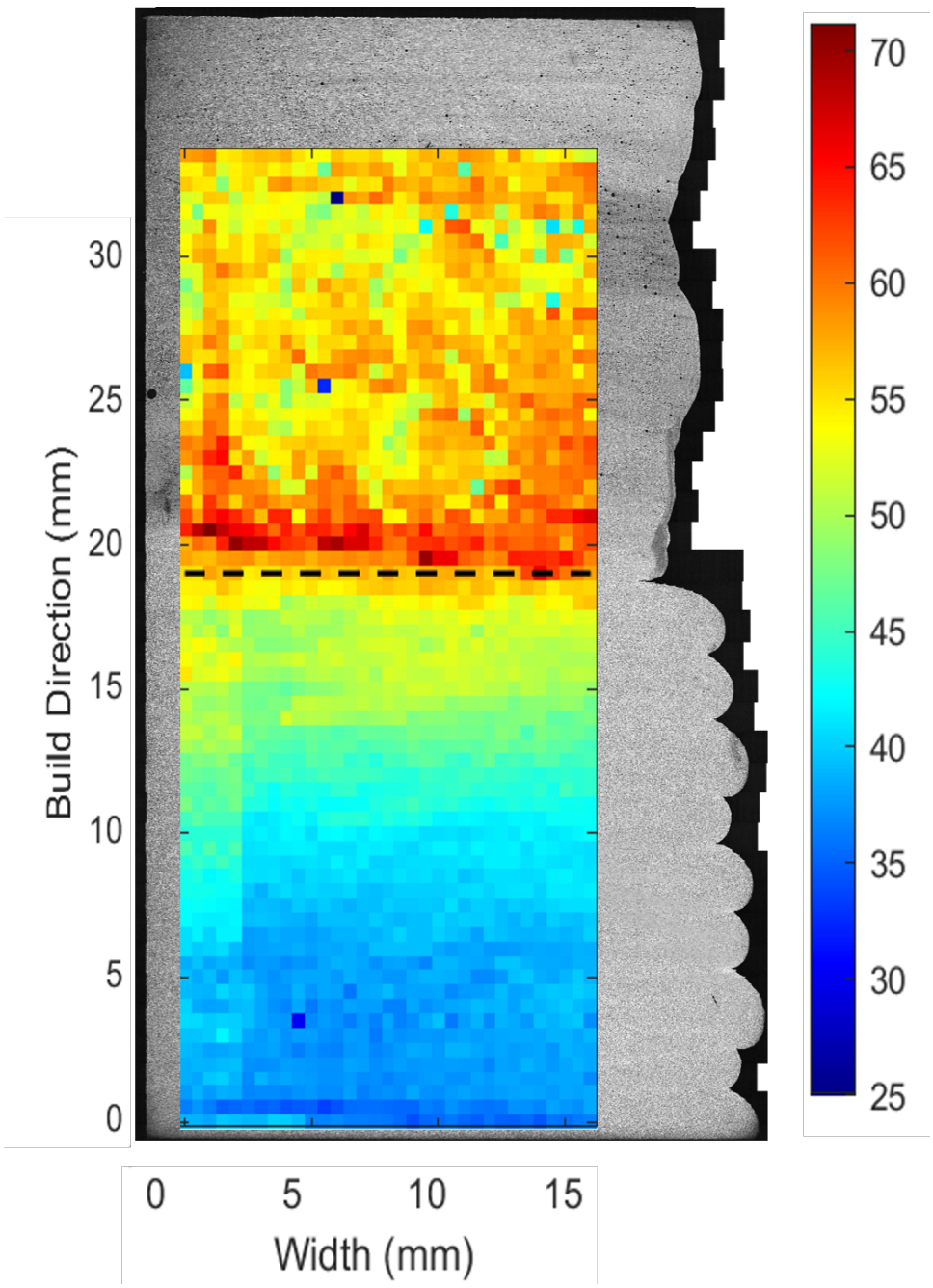


Figure 4.19: Microindentation hardness profile across the AD Al6061-Al4943 interface.

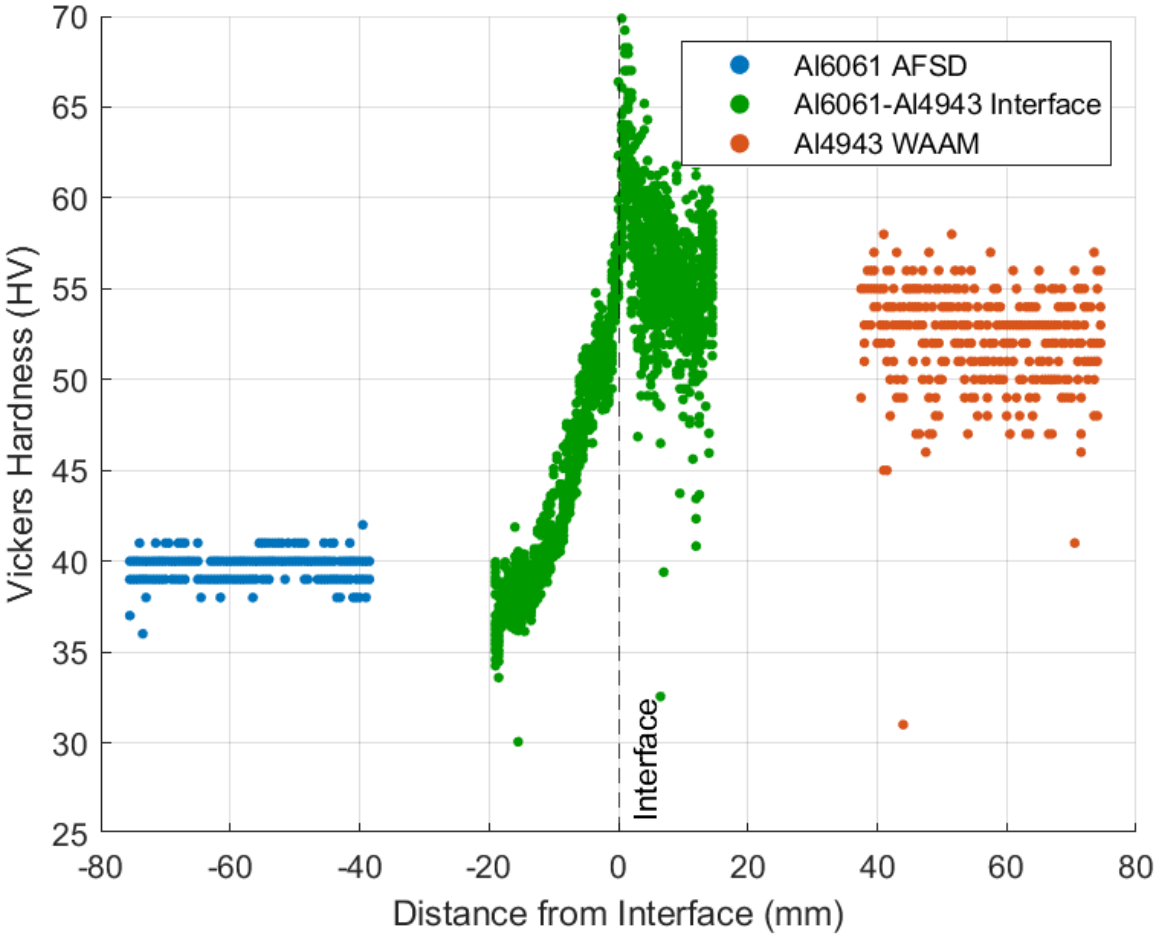


Figure 4.20: Microindentation hardness within the AD Al6061 AFSD, Al6061-Al4943 interface and Al4943 WAAM samples.

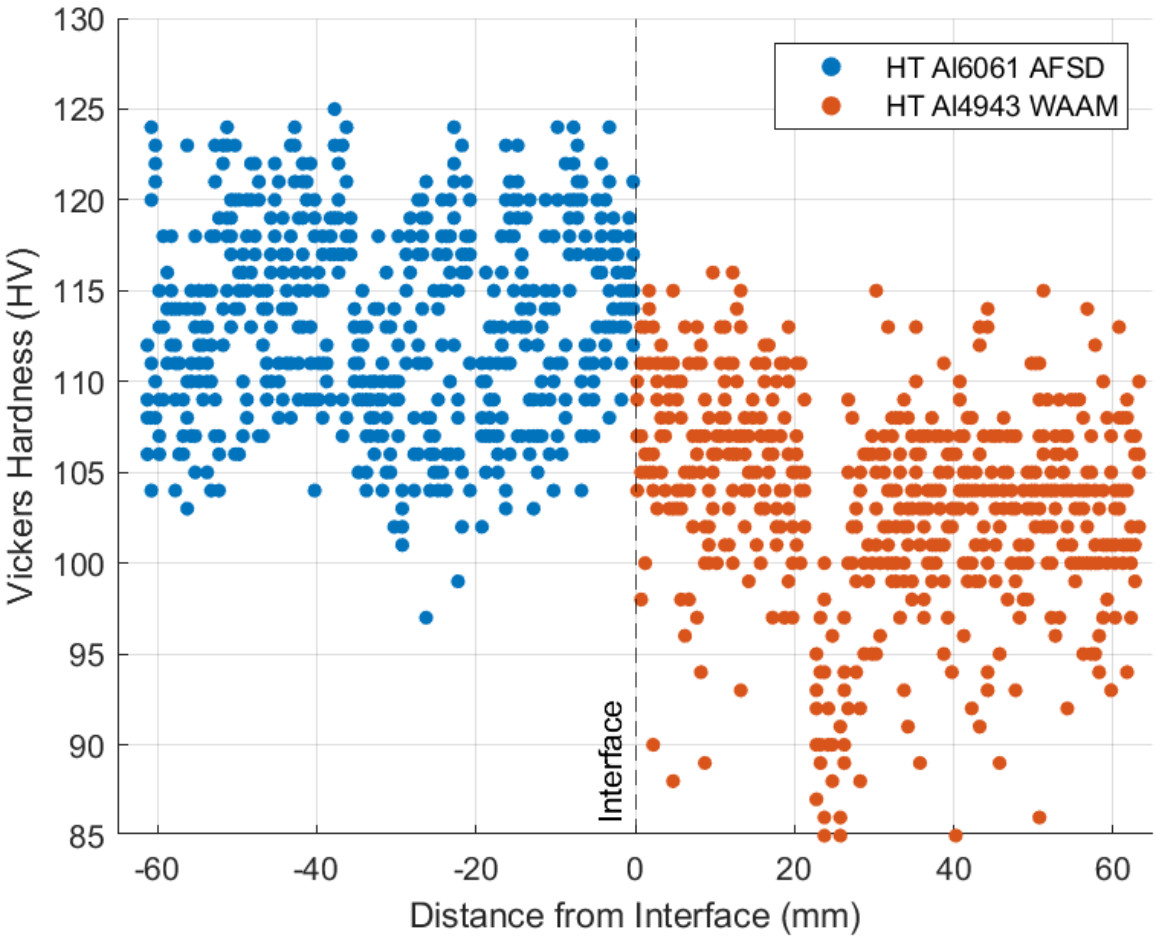


Figure 4.21: Microindentation hardness within the HT Al6061 AFSD, Al6061-Al4943 interface and Al4943 WAAM samples.

creates a maximum hardness at the Al6061-Al4943 interface regardless of the surface roughness of the AFSD process. The Al6061 AFSD is softer than the Al4943 in the AD condition which is consistently seen throughout all builds. The hardness peaks at the interface and reaches a steady like state within the Al4943 WAAM. The AD Al4943 deposited on the machined Al6061 AFSD top surface can be seen to have a lower hardness value than the Al6061 AFSD AD top surface. This is because of the 3 mm machined off the top surface. The AD Al4943 deposited on the machined Al6061 AFSD side surface, shows a greater rate of change for the hardness values along the interface. The Al4943 was deposited within the overaged bulk material of the Al6061. This area lacks the increase in hardness from the Al6061 AFSD top layers, which creates a more abrupt change in hardness across the interface.

In the HT condition, all deposits follow the same trend where the Al6061 region retains the HT Al6061 hardness and the Al4943 region retains the HT Al4943 hardness. An abrupt difference is seen at the interface for both top deposits of Al4943. For the Al4943 deposited along the machined Al6061 side surface there is a gradual decline to the nominal HT Al4943 hardness. This could be due to a greater dilution zone along the side surface.

For the MM that utilizes a dual-track Al6061 base, the same trend is observed as seen in figure 4.23 and appendices A.16, A.17 and A.18. The AD and HT conditions follow the same trend that the single-track MM did. This is expected as both track types for the Al6061 AFSD hardness samples were previously seen to follow the same trends. The track overlap region in the dual-track deposits show no obvious change in hardness.

The hardness of the MM deposits follow the same trends of the parent alloy deposits in both the AD and HT conditions. An increase in hardness in the AD samples in the positive build direction was observed starting roughly 30 mm from the top of the deposit. The same trend was observed for both the Al6061 and Al4943 due to overaging. The HT for both alloys increase the hardness, while also establishing a more homogeneous hardness throughout the deposit. The HT Al6061 is consistently

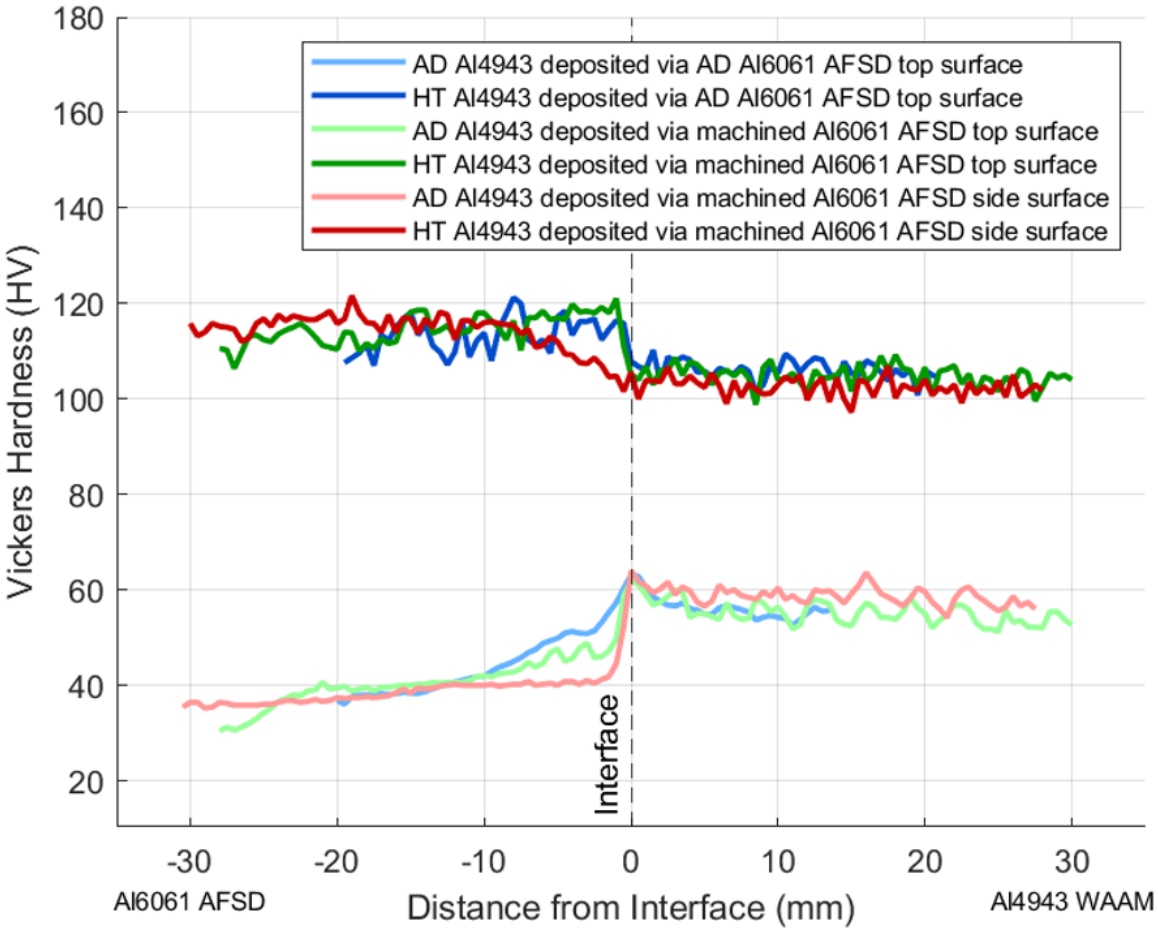


Figure 4.22: Average microindentation hardness across all single-track MM deposits with various conditions.

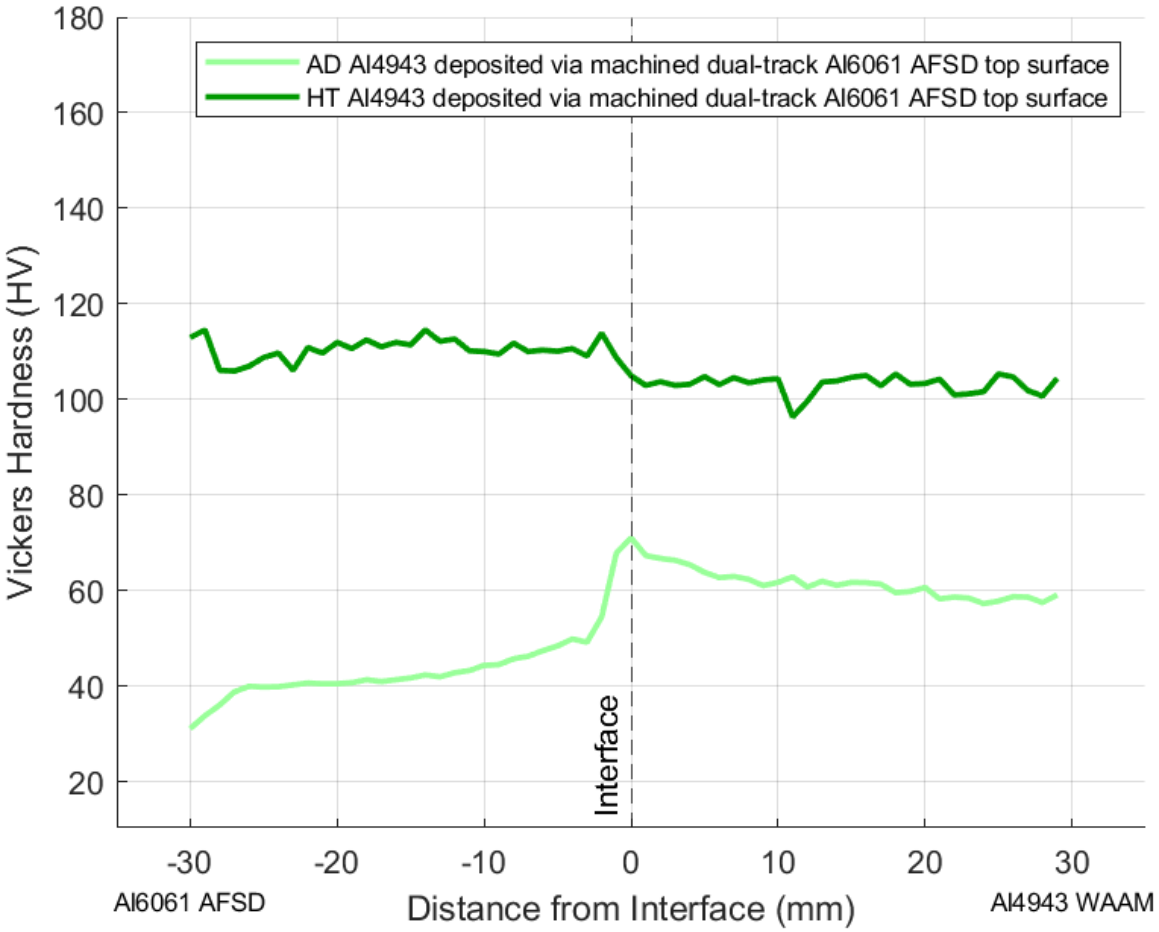


Figure 4.23: Average microindentation hardness across all dual-track MM deposits with various conditions.

harder than the HT Al4943, by about 10 HV. For all MM deposits the same trends were observed. For the AD condition the hardness in the Al6061 increases through the build direction, reaching a maximum at the Al6061-Al4943 interface. Within the Al4943 region, the hardness is steady state until roughly 30 mm from the top of that deposit, where an increase in hardness is observed again. For each MM deposit, in the HT condition, each alloy retained their respective HT hardness. An abrupt change in hardness was observed at the interface, where the hardness changed from the HT Al6061 hardness to the HT Al4943 hardness. The abrupt change in hardness at the interface was not repeated for the Al4943 deposited on the machined side Al6061 surface. Instead, a gradual change was present.

4.3.4 Tensile testing results

The tensile properties of the parent alloys as well as the interface for each condition was evaluated. The YS, UTS and total elongation for the parent alloys are compared to the interface.

4.3.5 Parent alloy tensile testing results

The tensile data for both alloys in the AD and HT condition are shown in tables 4.2, 4.3, and 4.4. Figure 4.24 shows the tensile properties of the Al6061 AFSD in the AD and HT conditions. Appendix A.22 shows the tensile data containing an outlier in the AD condition that was omitted. In the AD condition of the Al6061, the horizontal samples are observed to have a higher UTS and total elongation than the vertical samples. These samples were aligned with the printing direction, which correlate with the higher ductility (35). The severe plastic deformation that enables dynamic recrystallization, forms fine equiaxed grains, that usually align with the tool motion. The vertical samples were extracted in the build direction, across the bonded layers, which can promote crack initiation. The 0.2% offset YS between all samples was relatively repeatable. The tensile properties of the AD Al6061 AFSD

samples verify that a dissolution of the strengthening precipitates from the feedstock occurred, resulting in the low tensile strength. The HT condition improved the tensile properties with an increase in YS and UTS but a decrease in elongation. Alike in the AD condition, the vertical samples tend to have a lower YS and UTS than the horizontal samples. The decrease in ductility and increase in tensile strength can be attributed to the precipitation strengthening formed during the HT process.

The tensile properties in the AD and HT condition of Al4943 deposited via WAAM are shown in figure 4.25. In the AD condition, the horizontal samples tend to have a higher total elongation. The grains were observed to grow in the build direction, increasing the number of grain boundaries to overcome when pulling in the horizontal direction. In the HT condition, there was an increase in YS and UTS but a decrease in ductility. This is similar to the Al6061, where the HT causes the total elongation to decrease and the strength of the material to increase. Precipitate particles formed during the HT process, enable precipitation strengthening of the material. This improved the tensile strength of the material, as seen in table 4.3. Previous research of Al4943 WAAM has similar findings, where in the AD condition, a measured YS of 70 MPa and UTS of 167 MPa were improved to 160 MPa and 227 MPa, in the HT condition (66).

Equations 2.2 and 2.3 allow for an approximation of YS and UTS values of aluminum welds, from the hardness. Utilizing this formula, the measured YS and UTS of the Al4943 WAAM material are compared to the calculated values. This is also done for the Al6061 AFSD, but these equations were not developed for this process. The calculated and measured values can be seen in table 4.5. For most of the print conditions, the percent difference between the measured and calculated values are within 15%. The UTS values for the Al4943 are well represented by this equation, as the percent difference lies within 5%. For all of the print conditions, these equations enable an approximation of the YS and UTS within 16.4% of the average measured values.

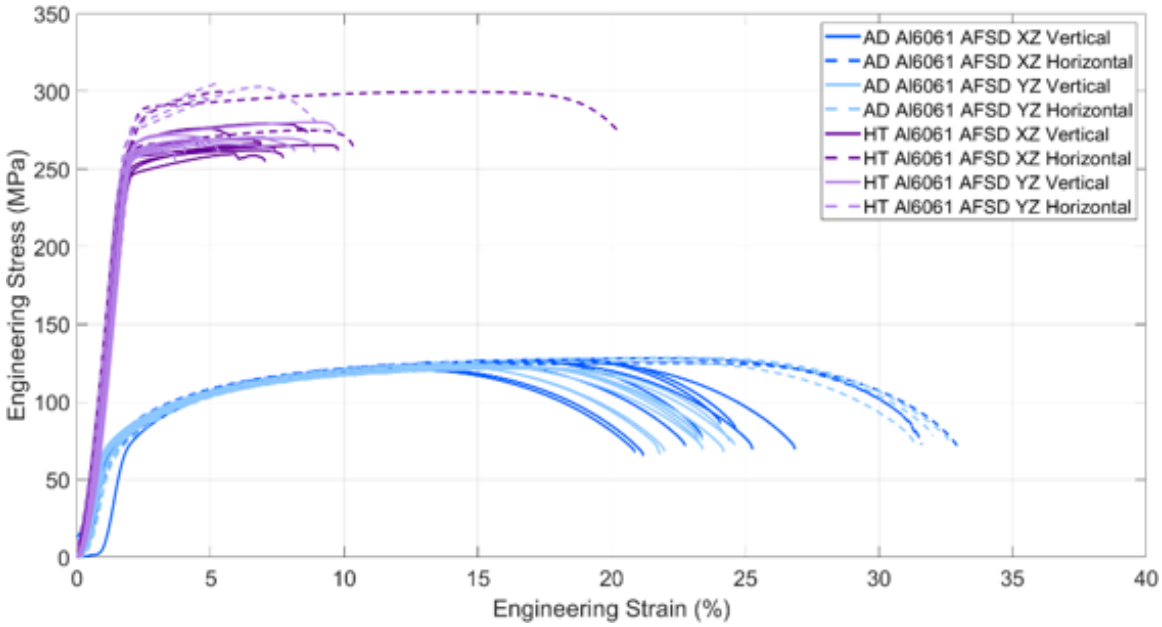


Figure 4.24: Engineering stress-strain curves for the AD and HT condition of Al6061 deposited via AFSD.

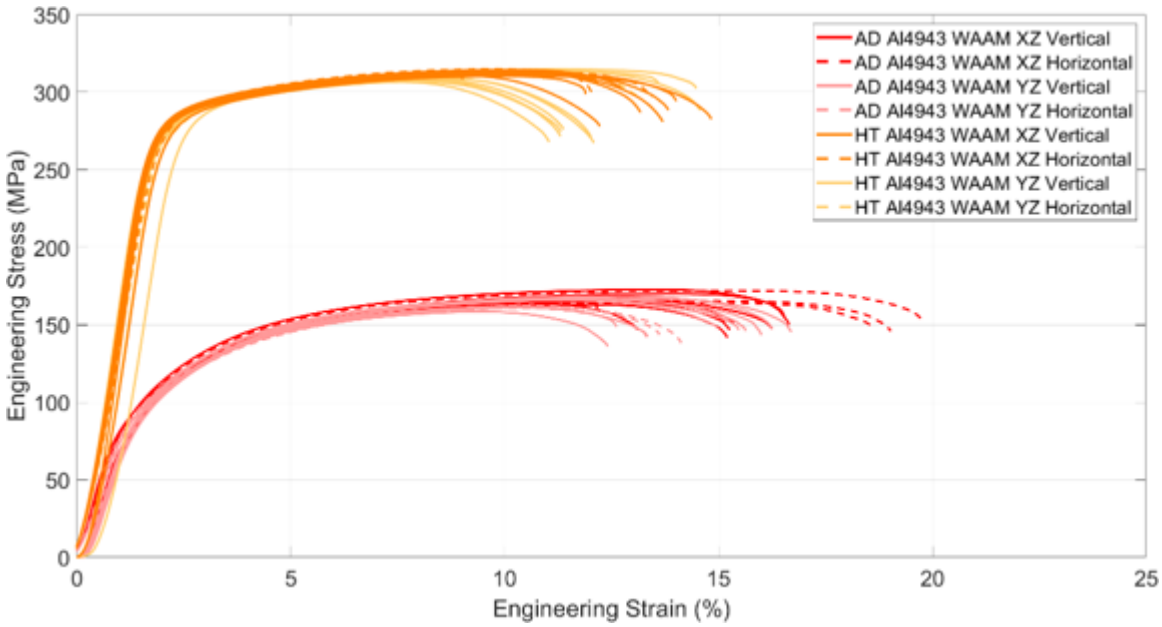


Figure 4.25: Engineering stress-strain curves for the AD and HT condition of Al4943 deposited via WAAM.

Table 4.2: Yield Strength of Al6061 AFSD and Al4943 WAAM under AD and HT conditions.

Print Condition	**Vertical YS (MPa)**		**Horizontal YS (MPa)**	
	XZ	**YZ**	**XZ**	**YZ**
AD Al6061 AFSD	73.3 ± 4.8	71.1 ± 3.7	73.2 ± 9.1	72.2 ± 7.8
HT Al6061 AFSD	259.4 ± 13.5	263.8 ± 8.7	281.3 ± 28.1	281.7 ± 10.8
AD Al4943 WAAM	89.1 ± 6.3	91.6 ± 4.7	91.1 ± 6.0	90.8 ± 1.8
HT Al4943 WAAM	283.2 ± 5.9	281.2 ± 7.3	285.1 ± 2.2	281.4 ± 1.7
Wrought Al6061-T6	276	276	276	276

Table 4.3: Ultimate Tensile Strength of Al6061 AFSD and Al4943 WAAM under AD and HT conditions.

Print Condition	**Vertical UTS (MPa)**		**Horizontal UTS (MPa)**	
	XZ	**YZ**	**XZ**	**YZ**
AD Al6061 AFSD	125.1 ± 5.1	123.3 ± 2.0	127.1 ± 3.3	127.7 ± 2.7
HT Al6061 AFSD	267.8 ± 12.6	269.3 ± 10.7	291.5 ± 28.6	301.3 ± 8.6
AD Al4943 WAAM	167.3 ± 5.9	164.8 ± 6.8	167.3 ± 8.4	161.5 ± 1.7
HT Al4943 WAAM	312.5 ± 3.1	310.1 ± 6.5	313.6 ± 2.6	313.4 ± 1.9
Wrought Al6061-T6	310	310	310	310

Table 4.4: Total elongation at fracture of Al6061 AFSD and Al4943 WAAM under AD and HT conditions.

Print Condition	**Vertical Elongation (%)**		**Horizontal Elongation (%)**	
	XZ	**YZ**	**XZ**	**YZ**
AD Al6061 AFSD	23.63 ± 4.05	23.37 ± 1.96	31.95 ± 1.71	31.98 ± 1.26
HT Al6061 AFSD	7.18 ± 3.02	6.55 ± 4.35	12.07 ± 14.97	6.41 ± 4.68
AD Al4943 WAAM	19.14 ± 1.22	14.82 ± 3.24	19.14 ± 1.22	13.7 ± 0.8
HT Al4943 WAAM	13.18 ± 1.99	12.42 ± 2.83	11.53 ± 4.43	11.45 ± 2.94
Wrought Al6061-T6	12	12	12	12

Table 4.5: Comparison of the calculated YS and UTS values derived from the hardness data and the measured YS and UTS.

Print Condition	**Calculated**		**Measured**		**Percent Difference**	
	YS (MPa)	**UTS (MPa)**	**YS (MPa)**	**UTS (MPa)**	**YS (%)**	**UTS (%)**
AD Al6061 AFSD	78.6	147.5	71.1	123.3	9.6	16.4
HT Al6061 AFSD	277.6	311.3	263.8	269.3	5.0	13.5
AD Al4943 WAAM	102.03	166.8	91.6	164.8	10.2	1.2
HT Al4943 WAAM	263.0	299.2	281.2	310.1	6.9	3.6

The properties of both alloys in the AD condition fall well short of meeting the wrought Al6061-T6 properties. This is expected, as other studies have shown that the thermal cycling during the additive processes, creates an overaging effect (51; 47). This causes a partial solutionizing of the material in the AD condition, which weakens the mechanical properties from the feedstock material. Anisotropy is present in both alloys, due to the additive techniques. However, after T6 HT of both alloys, the tensile properties are significantly improved. The anisotropy is minimized, especially in the HT Al4943 WAAM material. The HT Al6061 AFSD is still below wrought Al6061-T6 properties, wheras the HT Al4943 WAAM is comparable. The variability within the material causes for the possibility of lower properties than the wrought Al6061-T6, but is still in good agreement with it.

4.3.6 Multi-material tensile testing results

Each MM deposit that used a single-track Al6061 AFSD deposit had the tensile properties across the interface measured. They are compared to the properties of the parent alloys. For the sample that deposited Al4943 on the Al6061 AFSD AD top surface, the tensile properties across the interface are evaluated in figure 4.26. Only the vertical samples for the individual alloys are represented. This allows for a direct comparison to the interface. In the AD condition, the interface exhibits comparable YS, UTS, and ductility to the AD Al493 WAAM. However, the interface samples prematurely reach uniform elongation and sustain necking for a longer duration than the Al4943 WAAM parent alloy. The necking response more closely resembles the necking region of the Al6061 AFSD. This could be due to a localized fracture initiation, associated with a debonding at the bimetallic interface. The dilution at the interface produces a mechanical response that reflects a combination of both alloys, with the interface tensile properties in the AD condition residing between those of Al6061 AFSD and Al4943 WAAM.

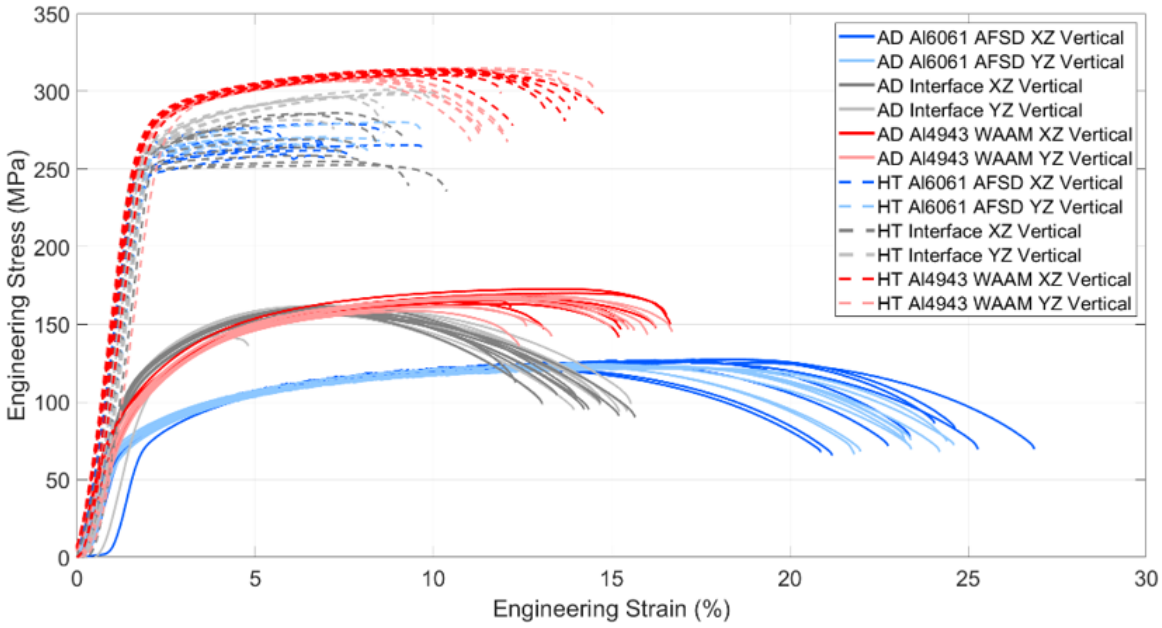


Figure 4.26: Engineering stress-strain curves for the AD and HT condition of the Al6061-Al4943 interface for Al4943 deposited on the Al6061 AFSD AD top surface.

The interface region has trends similar to those of the parent alloys in the HT condition. The YS, UTS and elongation of the interface region are representative of the parents alloys. The YS and UTS increased substantially from the AD condition, but the ductility decreased. The HT XZ vertical and YZ vertical have a noticeable difference that was not as distinct in the AD condition. The YZ vertical has a higher YS and UTS but the ductility is relatively the same for both sample orientations. The HT promotes a more uniform transition of material composition at the interface. A partial dilution zone is present, thus creating an intermixed alloy at the interface. The interface mechanical properties are limited by the weaker material but the dilution zone has an effect. This is represented as the mechanical properties reside between the two parent alloys, similar to the AD condition. Hauser et al. (78) found that an Al5087 and Al6060 MM wall was limited by the weaker material. Larger tensile specimens with a 25 mm gage length were used, as the weak point of the material is included in the longer gage length.

The gage length of the miniature tensile specimen encompasses approximately 5 mm of each alloy, when measuring across the interface. In the Al6061 region, hardness peaks at the interface and gradually decreases over a distance of about 30 mm before reaching a steady-state value. As a result, fracture occurs in the region of lowest hardness, typically near the end of the gage length. The interface specimens appear to fail in a dilution zone, within the Al6061. The AD condition sample exhibited properties representative of each parent alloy, while the HT condition sample is representative of the Al6061 HT condition. This provides evidence that failure occurred within a dilution zone in the Al6061, as the HT creates a uniform material. Hardness and tensile properties are not affected by the the overaging effects that impact samples in the AD condition. A longer gage length that fully captures the change in hardness would provide a better representation of the true failure mechanisms in the AD condition.

When depositing Al4943 on the top of the Al6061 AFSD deposit, two different versions were performed. One version used WAAM to deposit Al4943 on the AD

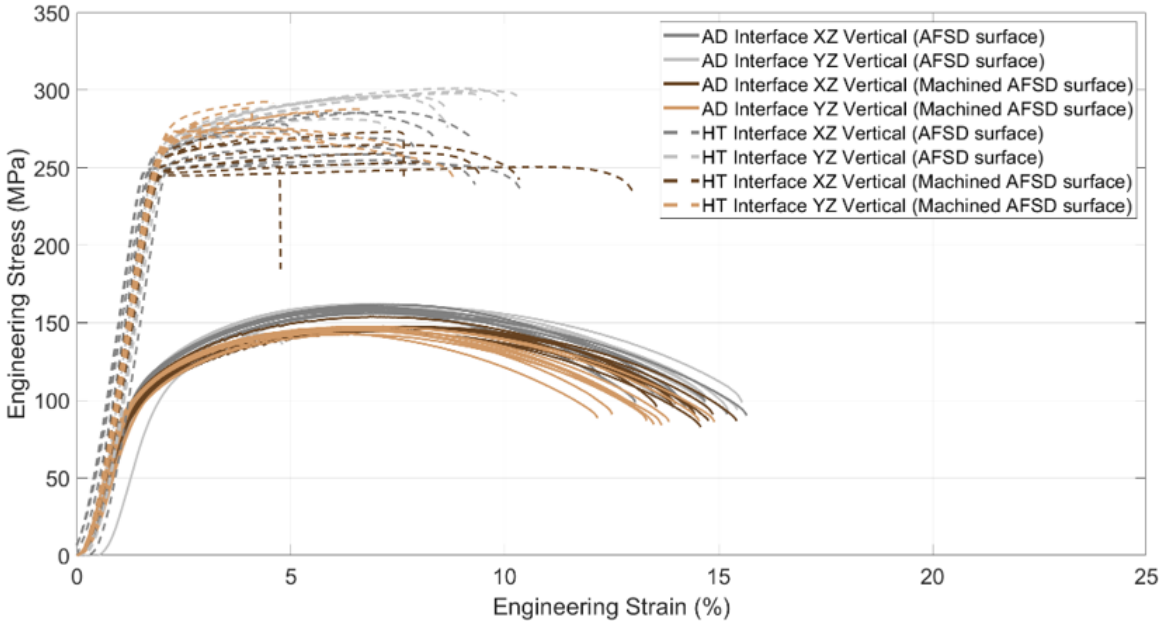


Figure 4.27: Engineering stress-strain curves for the AD and HT condition of the AD and machined Al6061-Al4943 interface.

Al6061 AFSD top surface and the other version had an intermediate machining operation of the Al6061 AFSD top surface. These two versions are compared to evaluate whether the surface of the AD AFSD top surface needs to be machined. The stress-strain curves for both version in the AD and HT condition can be seen in figure 4.27. In the AD and HT condition, both sample sets follow the same trend and have great agreement between one another. The interface for the AD AFSD top surface has slightly higher YS and UTS values in the AD condition, but the HT condition has no noticeable difference between the conditions. The surface roughness on the AD AFSD top surface does not seem to impact the joining of the Al4943 as the properties align with the interface that utilized a machined top surface. The striations on the top AFSD surface produced from the AFSD process do not seem to hinder fusion from the WAAM process. This enables deposition without needing to modify the AFSD top surface.

Lastly, Al4943 was deposited on the side of an Al6061 AFSD deposit after an intermediate machining operation. Tensile specimens were extracted along the interface, which would mimic extracting specimens in the horizontal orientation of the Al6061 AFSD region and the vertical direction of the Al4943 WAAM region. The corresponding tensile properties are plotted in figure 4.28, to compare to the interface. In the AD condition, the interface samples have a similar YS and UTS to the Al6061 samples but the elongation is lower. There is not a clear trend as to how the parent alloys are affecting the properties but it seems as if there is an effect due to dilution. In the HT condition, the interface samples follow the trends of the HT parent alloys but have a decreased YS and UTS in some samples. The HT condition has a closer representation to the parent alloys, which could be due to the more uniform interface transition. This testing provided insight into how depositing material along the side profile of an AFSD deposit affects the MM. These findings, enable one to machine away the edge effects from the AFSD process and ensure full fusion at the interface. The interface does not seem to be a limiting factor for this printing orientation and

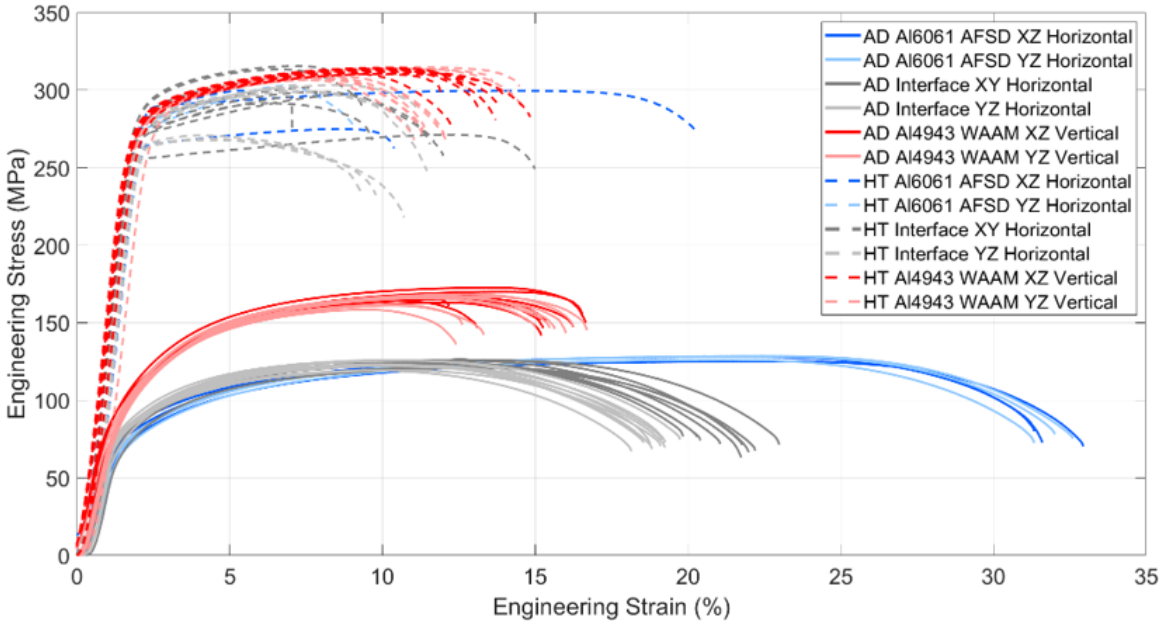


Figure 4.28: Engineering stress-strain curves for the AD and HT condition of the Al6061-Al4943 interface along the machcined side of the Al6061 AFSD deposit.

allows for additive processes with multi-axis deposition to be utilized with 3-axis AFSD deposition.

The overaging effects in the AD condition are different for this print orientation. Instead of a hardness gradient through the build direction, the hardness within the Al6061 AFSD, is relatively steady state. The Al4943 WAAM was deposited within the overaged Al6061. When Al4943 WAAM is on top of the Al6061 AFSD, it is affected by the increasing hardness trend near the top of the Al6061. The Al4943 deposited on the side profile of the Al6061 does not follow the same failure trends, as expected.

The YS, UTS and elongation at break can be seen for each tensile tested deposit. These are seen in figures 4.29, 4.30, and 4.31. Comparing the parent alloys, the Al6061 has a lower YS and UTS than the Al4943 in both the AD and HT conditions. The Al4943 in the HT condition, is closely representative of wrought Al6061-T6. Most of the average values meet the wrought Al6061-T6 properties but variability within the deposit can cause it to fall below the wrought benchmark. In both parent alloys, anisotropic behavior is observed. Al4943 is more representative of an isotropic behavior, especially in the HT condition. The ductility in all deposits have high variation, which could be due to the miniature tensile specimens.

When Al4943 was deposited on the AD top or top machined AFSD surface, a major difference was not observed in the tensile data. This again provides assurance that depositing on the AD AFSD top surface is sufficient. When depositing Al4943 on the side profile of a machined AFSD deposit, there is a slight difference when comparing to the other interfaces. The samples were taken in the XY and YZ horizontal directions. This combines the print direction of the AFSD deposit and the build direction of the WAAM deposit. In the AD condition, the YS and UTS have lower values, compared to the other interfaces. This is due to the overaging of the Al6061 effecting the hardness within the bulk material compared to the top of the deposit. The interface properties when Al4943 is deposited on top of the

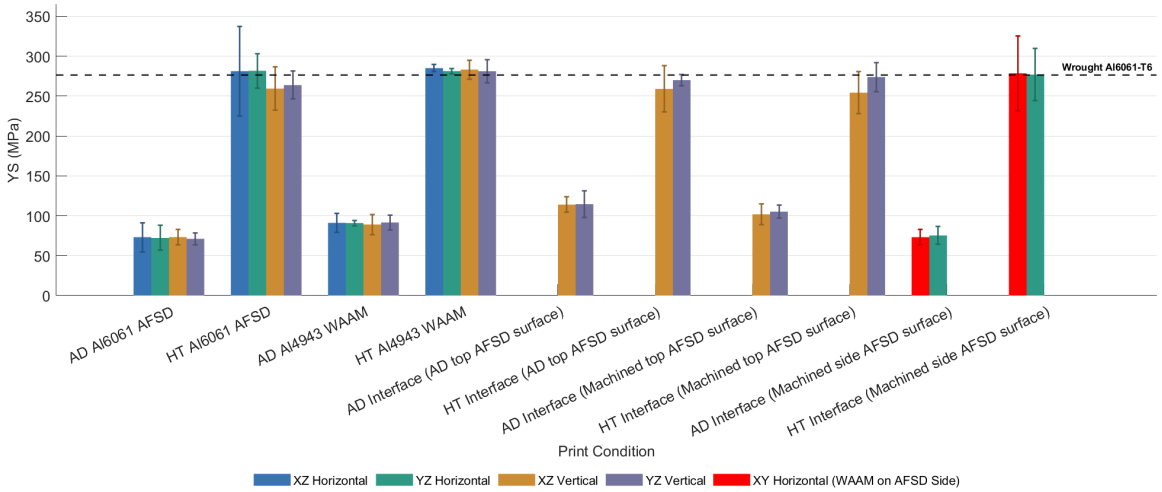


Figure 4.29: Yield strength of each print orientation in the AD and HT condition.

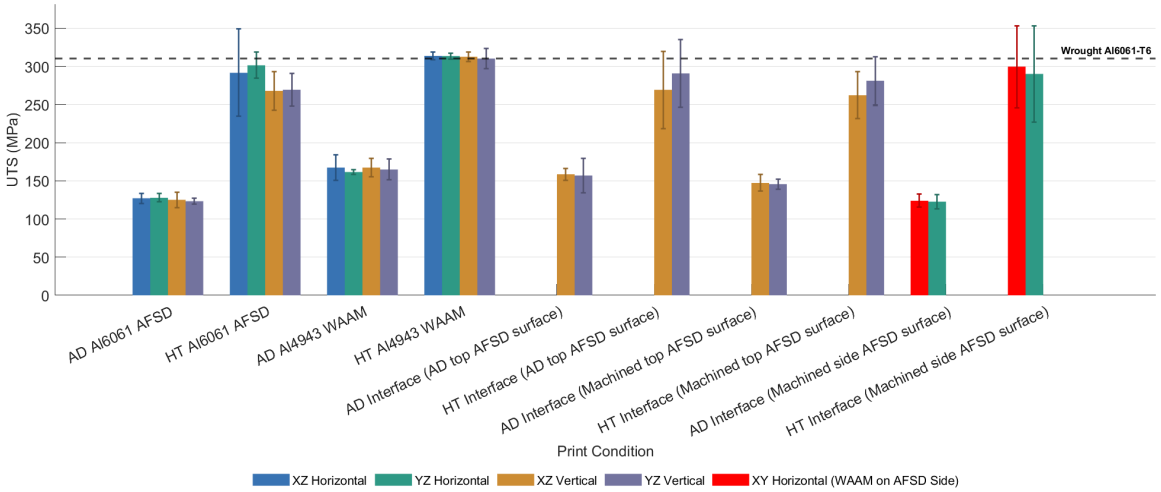


Figure 4.30: Ultimate tensile strength of each print orientation in the AD and HT condition.

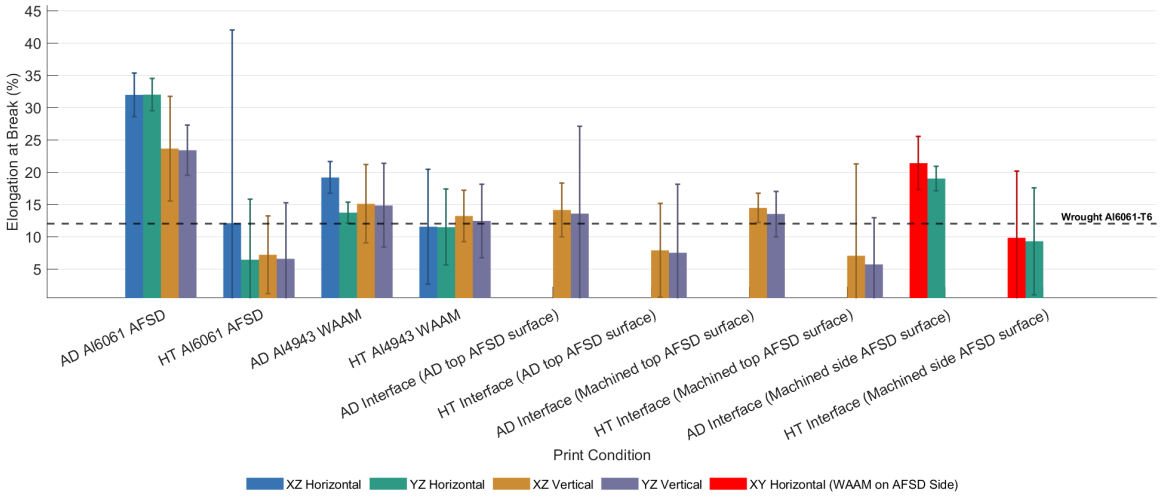


Figure 4.31: Total elongation of each print orientation in the AD and HT condition.

Al6061 are higher than when deposited on the side. The HT condition removed these effects, creating a more uniform material. Overall, the tensile properties are fairly repeatable throughout each print orientation. The Al6061 AFSD has inferior mechanical properties that seems to be responsible for the interface properties having lower measured values than the Al4943 properties. The miniature tensile specimens do not capture both unaffected regions of each alloy within the gage length. Failure is occurring within the minimum strength region.

Aluminum literature shows that when welding a joint, the fusion zone of a weld is stronger than the base metal or HAZ. To enable fracture in the fusion zone of Al4043 and Al4943 welded joints, Ahmed et al. (16) had to use notched tensile specimens. The notch was located within the FZ to ensure fracture occurred there. Other specimens that lacked the notch, fractured in the base metal or the HAZ every time. This is comparable to the observations at the interface in this study. Due to the miniature tensile specimens, the dilution zone was captured in the gage length but the unaffected Al6061 AFSD region was not. A larger tensile specimen that fully captured all three regions, the Al6061, Al6061-Al4943 interface and the Al4943 would be expected to fracture within the Al6061 as this region has the lowest tensile strength.

4.3.7 Modified tensile testing results

A modified tensile specimen with an increased gage length was developed based on the ASTM E8 miniature tensile specimen. The gage length captured the entire overaged Al6061 AFSD material that the miniature tensile specimens did not. The interface was evaluated on the print variant that deposited Al4943 on the machined Al6061 AFSD top surface. The tensile data from the AD and HT conditions can be seen in figure 4.32. The strain data is inconsistent due to the aspect ratio of the modified samples. This shows a severe decrease in elongation, when compared to the parent alloys. However, the mechanical strength is representative of the Al6061 AFSD

mechanical strength in the AD and HT conditions. This verifies the hypothesis, that the weaker of the two parent alloys will initiate failure. It also verifies that the interface is not the weakest region of the MM, which indicates that failure will occur in the Al6061 AFSD. This is observed in both the AD and HT conditions. In table 4.6 and appendices A.23 and A.24, the modified tensile specimens mechanical strength is compared to the parent alloys. This clearly shows that the failure of these specimens is representative of the Al6061 AFSD parent alloy.

4.3.8 Fractography results

Fracture analysis was performed on the tensile specimens to help identify how the interface fractures compared to the parent alloy fractures. Figures 4.33 and 4.34 show the Al6061 AFSD fractured tensile specimens in the AD and HT condition. These are XZ vertical samples that had repeatable results. In the AD condition, the fracture location can be seen at 120x magnification in appendix A.25, where the dimples are quite coarse and the fracture morphology is rough. This corresponds with a ductile failure, which is verified in the stress-strain curves. The AD condition is very soft, as seen in the hardness testing and verified as the shear lips are pronounced at the edges of the failure location. The necking region in the tensile data, is verified with the decreased cross section observed at fracture. In the HT condition, the dimple morphology is finer and the fracture is not as rough. The shear lips are not as pronounced, due to the material being stronger but less ductile. This also corresponds with a decrease in the necking region seen in the strain-stress curve.

The fracture surfaces for the XZ vertical samples from the Al4943 WAAM in the AD and HT conditions can be seen in figures 4.35 and 4.36 respectively. In the AD condition, porosity is observed on the fracture surface. Dimples are also seen with smooth regions. The shear lips are minimal along the edges, indicating that necking occurred for a short period time. In the HT condition, porosity is still observed, with no noticeable difference in porosity concentration from the AD condition. The shear

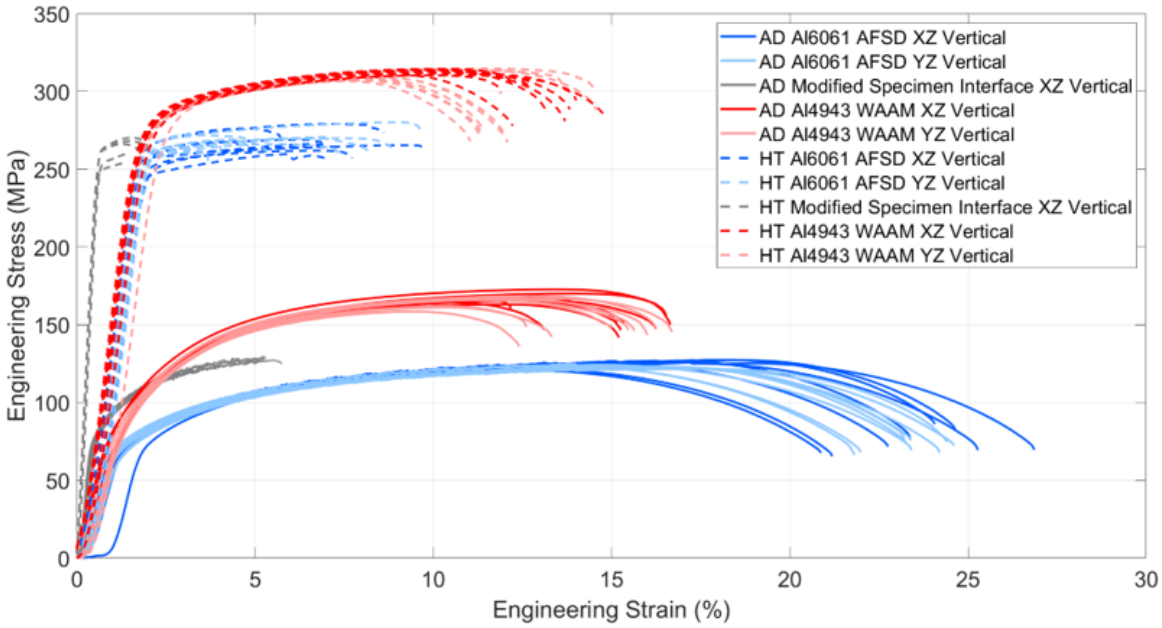


Figure 4.32: Engineering stress-strain curves for the AD and HT conditions of the modified tensile specimens.

Table 4.6: Mechanical strength of the modified tensile specimens compared to the parent alloys.

Print Condition	**Vertical YS (MPa)**		**Vertical UTS (MPa)**	
	XZ	**YZ**	**XZ**	**YZ**
AD Al6061 AFSD	73.3 ± 4.8	71.1 ± 3.7	125.1 ± 5.1	123.3 ± 2.0
HT Al6061 AFSD	259.4 ± 13.5	263.8 ± 8.7	267.8 ± 12.6	269.3 ± 10.7
AD Al4943 WAAM	89.1 ± 6.3	91.6 ± 4.7	167.3 ± 5.9	164.8 ± 6.8
HT Al4943 WAAM	283.2 ± 5.9	281.2 ± 7.3	312.5 ± 3.1	310.1 ± 6.5
AD Modified Specimen Interface	85.3 ± 8.8	-	127.2 ± 5.4	-
HT Modified Specimen Interface	259.0 ± 12.6	-	263.8 ± 13.0	-

lips are less pronounced along all edges, showing a decrease in ductility. Dimple size appears to be relatively constant. This would correlate with a stronger material that is less ductile, which corresponds with the findings in the stress-strain curves. In appendix A.26, an XZ horizontal sample in the HT condition was evaluated. Large porosity content was found within the sample, affecting the cross sectional area where fracture occurred. The porosity content within the Al4943 can effect the results.

The fracture surfaces from the XZ vertical tensile specimens of the Al4943 deposited on the AD AFSD top surface were evaluated in the AD and HT conditions. These are seen in figures 4.37 and 4.38. In the AD condition, the fracture is observed to be similar to the AD Al6061 AFSD fracture surface. The necking region produced a smaller cross sectional area and has steep shear lips along the edges that align with the Al6061 fracture. However, it is not as drastic as the Al6061 but it is more prevalent than in the Al4943. Coarse dimples are found throughout the fracture indicating a highly ductile material. Comparing to the stress-strain curves in the AD condition, the sample has strength and elongation comparable to the Al4943 WAAM, however the ductility corresponds with the Al6061 AFSD. This would encourage the belief that the sample fractured near the interface where dilution from the parent alloys occurred. The fracture locations of the tensile specimens in the AD condition, can be seen in appendix A.27. This shows fracture located in the Al6061 AFSD side of the interface. The location is repeated throughout each sample as the hardness decreased through the gage length. This would result in fracture occurring towards the bottom of the gage length, as was observed. In the HT condition, a rough fracture surface is identified. Irregular dimples are seen throughout the deposit and the shear lips are not as distinct as in the AD condition. The fracture locations of the tensile specimens in the HT condition, can be seen in appendix A.28. Fracture is repeatedly seen near the interface. This could be due to failure occurring at a dilution zone or directly within the Al6061 AFSD region. The HT condition establishes a relatively uniform material that breaks within the weaker region. The Al6061 AFSD is weaker than the Al4943 WAAM, indicating that failure should occur there. The stress-strain curve

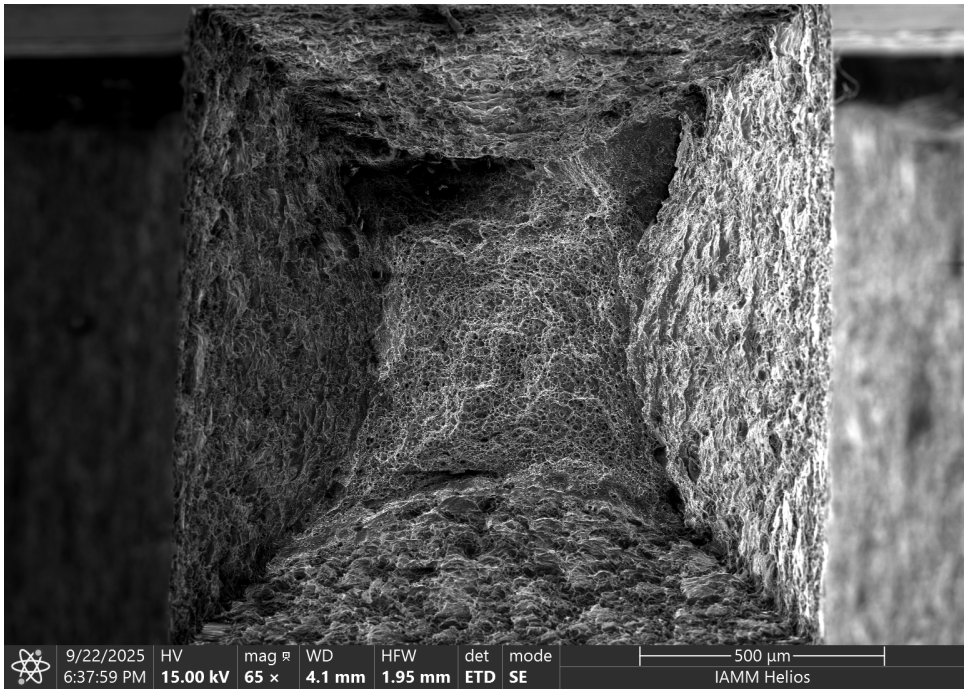


Figure 4.33: Fracture surface in the AD condition of Al6061 deposited via AFSD.

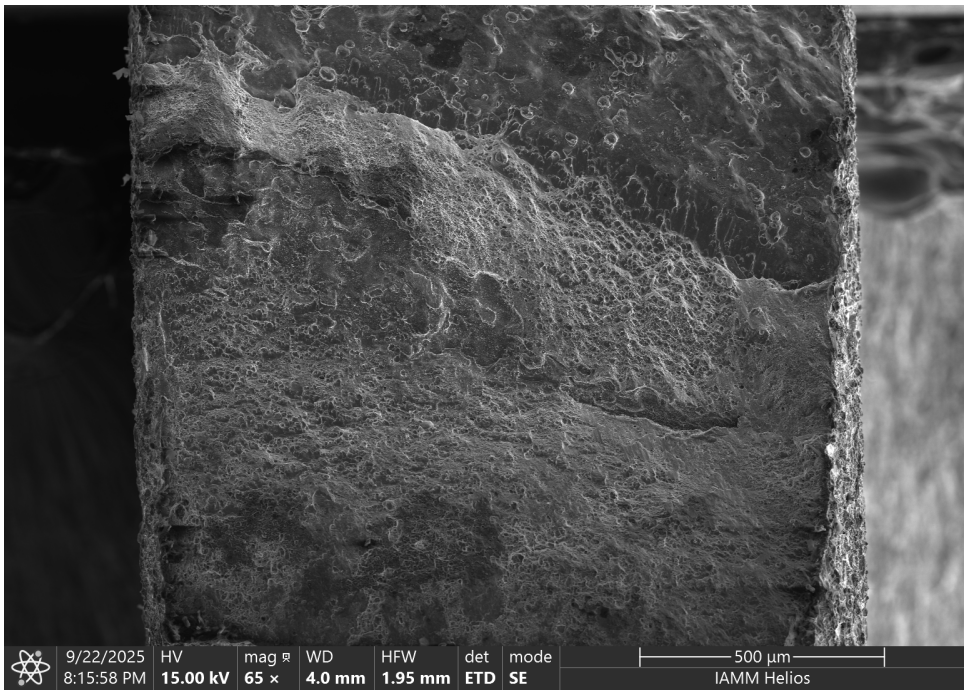


Figure 4.34: Fracture surface in the HT condition of Al6061 deposited via AFSD.

closely resembles that of the Al6061 AFSD in the HT condition, however the failure location could be located at the dilution zone. This is also observed in the stress-strain curve as the properties can lie between the two parent alloys and the failure location is near the interface each time. In both the AD and HT conditions, porosity is not identified, indicating that the failure occurred in the Al6061 region. Some dilution from the WAAM process, could be changing the microstructure near the interface into the Al6061 AFSD region. This would affect the mechanical properties, which is why we have a mix of properties as seen in the stress-strain curves and fracture surfaces of the MM samples.

The fracture surfaces from the Al4943 deposited on the machined AFSD side surface in the AD and HT conditions are seen in figures 4.39 and 4.40. In the AD condition, the failure mechanisms are representative of what was observed in the AD Al6061 AFSD region. The specimen can be seen to have large shear lips with a decreased cross sectional area. Coarse dimples are throughout the fracture surface and these are all representative of a ductile failure. This is verified in the stress-strain curves, where the ductility and strength closely matches the Al6061 samples. However, the elongation does not. The fracture locations seen in appendix A.29, show failure occurring at the interface for every samples. This is because of the Al4943 depositing within the overaged region of Al6061 AFSD. The hardness is uniformly low within the Al6061, which is why failure would initiate right in the Al6061 region. This is different than the Al4943 deposited on the top surface of the Al6061 because the top of Al6061 does not have uniform hardness. The hardness decreases from the top of the deposit, into the bulk material. The tensile specimens then fractured along the bottom of the gage length as this region had the lowest hardness, correlating with the weakest part of the gage length. In the HT condition, the fracture surface is representative of a HT Al4943 WAAM sample as failure occurred within the WAAM region of this sample. Porosity content is observed along the fracture surface, which provides clear evidence of the failure occurring within the Al4943 WAAM material. Coarse dimples are also seen with almost no indication of shear lips. This is representative of a ductile

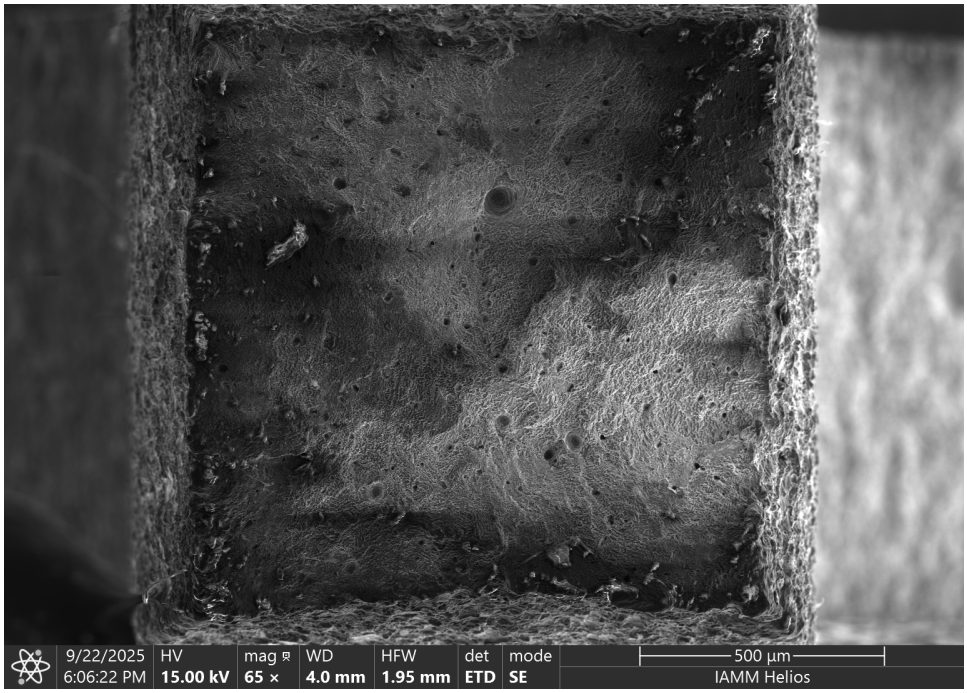


Figure 4.35: Fracture surface in the AD condition of Al4943 deposited via WAAM.

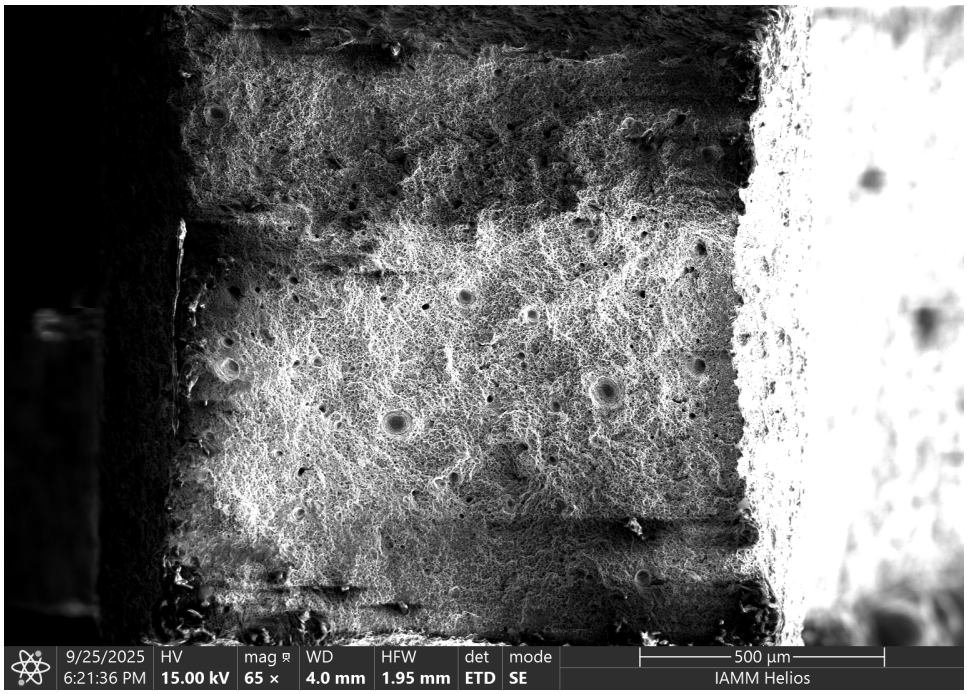


Figure 4.36: Fracture surface in the HT condition of Al4943 deposited via WAAM.

fracture, however not as ductile as in the AD condition. The failure locations can be seen in appendix A.30. The fifth sample shows failure occurring near the top of the gage length, within the Al4943 WAAM region. Failure of most of the samples are seen to be within the Al6061 AFSD region which is expected as this is the weaker of the two parent alloys.

When depositing Al4943 via WAAM on the Al6061 AFSD material, the overaging effect needs to be accounted for in the AD condition. This creates a gradient of material properties through the Al6061 AFSD region, which can initiate failure at its weakest point. This was seen when depositing Al4943 on top of the Al6061 AFSD, as the gage length did not capture the uniform, overaged material. This is located 30 mm from the top of the Al6061 AFSD deposit. The Al4943 deposited on the side of Al6061 was not affected by the gradient as this was printed on the overaged material. The failure of these specimens, is representative of the Al6061 AFSD parent alloy as this is the weakest link. If longer tensile samples were used for the Al4943 on the top of the Al6061 AFSD, then failure would occur within the overaged Al6061. To test this, a modified tensile specimen, with a larger gage length was extracted from the Al4943 deposited on the machined Al6061 AFSD MM. The larger gage length captures the gradient and the overaged material of the Al6061 AFSD. Failure should occur near the bottom of the modified tensile specimen, as the overaged Al6061 AFSD material will have the weakest mechanical properties. The failure will then be more accurately reflected in the Al6061 AFSD parent alloy failure. Appendices A.31 and A.32 show the fractured modified tensile specimens in the AD and HT conditions. In the AD condition, fracture occurs at the bottom of the gage length, within the overaged Al6061 AFSD region. This was expected as this region has the lowest hardness, correlating with the weakest mechanical strength. One sample is seen to have fractured higher in the Al6061 AFSD region, as this is where the overaged hardness reached steady state. In the HT condition, all the samples failed within the overaged Al6061, where the hardness reached a steady state. This is where the

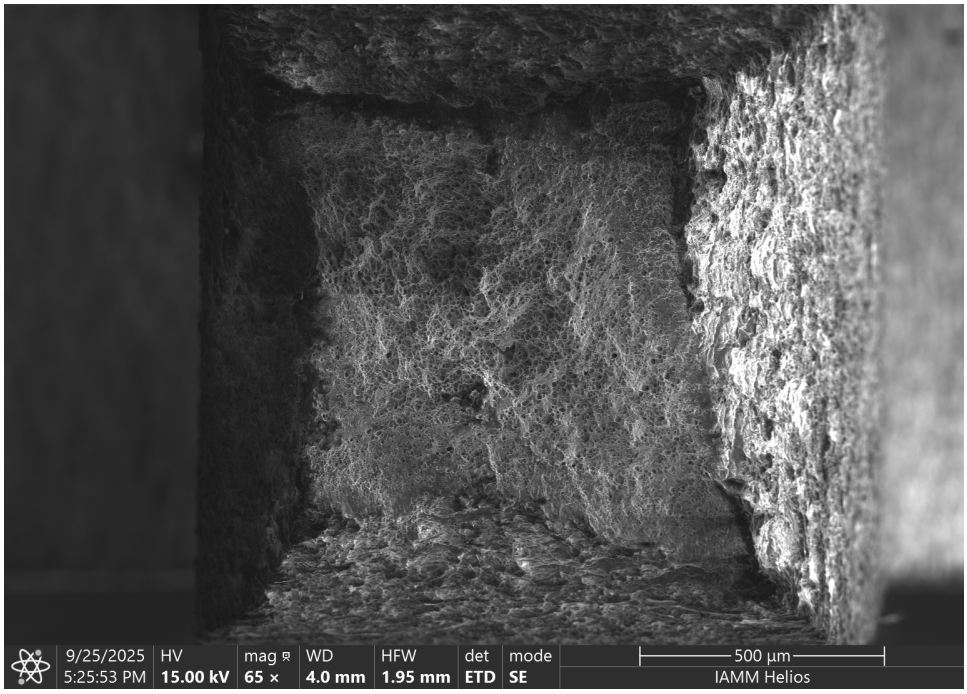


Figure 4.37: Fracture surface in the AD condition of the interface, where Al4943 was deposited on the AFSD AD top surface.

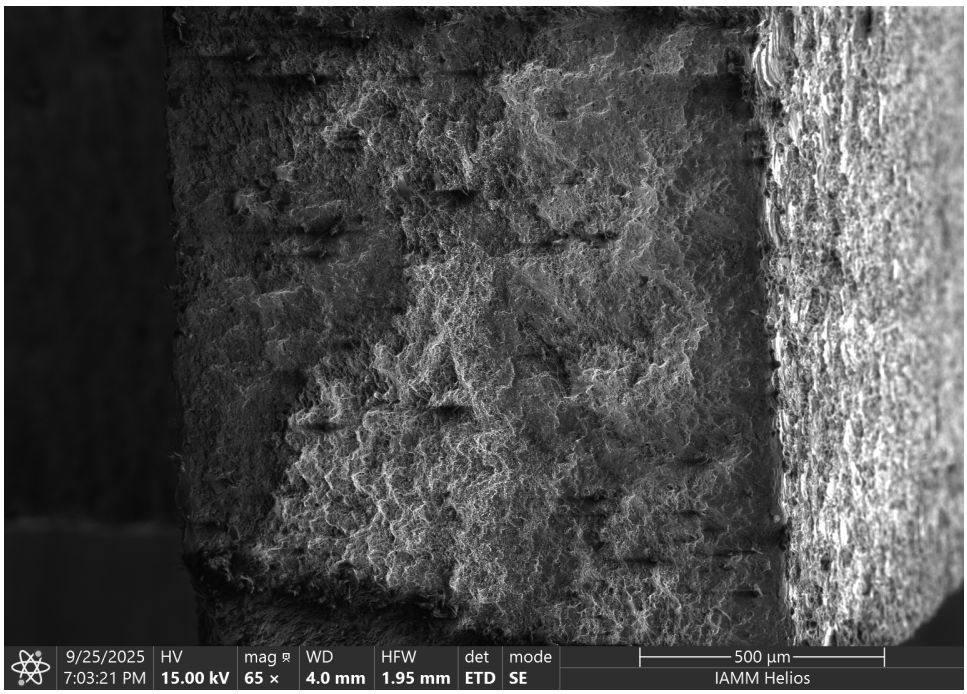


Figure 4.38: Fracture surface in the HT condition of the interface, where Al4943 was deposited on the AFSD AD top surface.

overaged material starts in the bulk of the Al6061 AFSD. The failure location verifies that the weaker parent alloy dictates failure of the MM, not the interface.

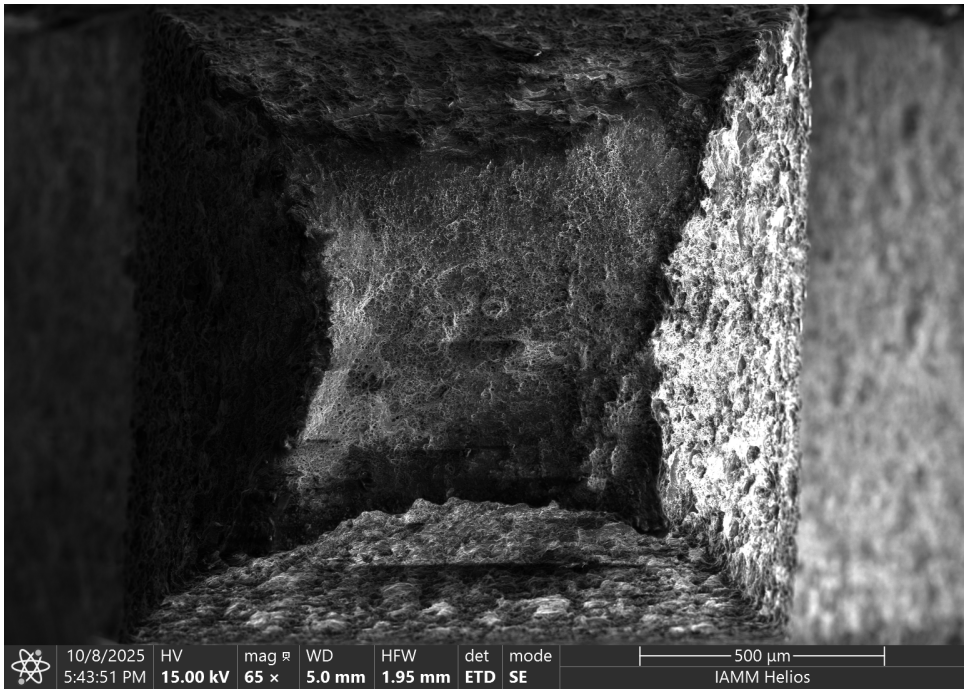


Figure 4.39: Fracture surface in the AD condition of the interface, where Al4943 was deposited on the machined AFSD side surface.

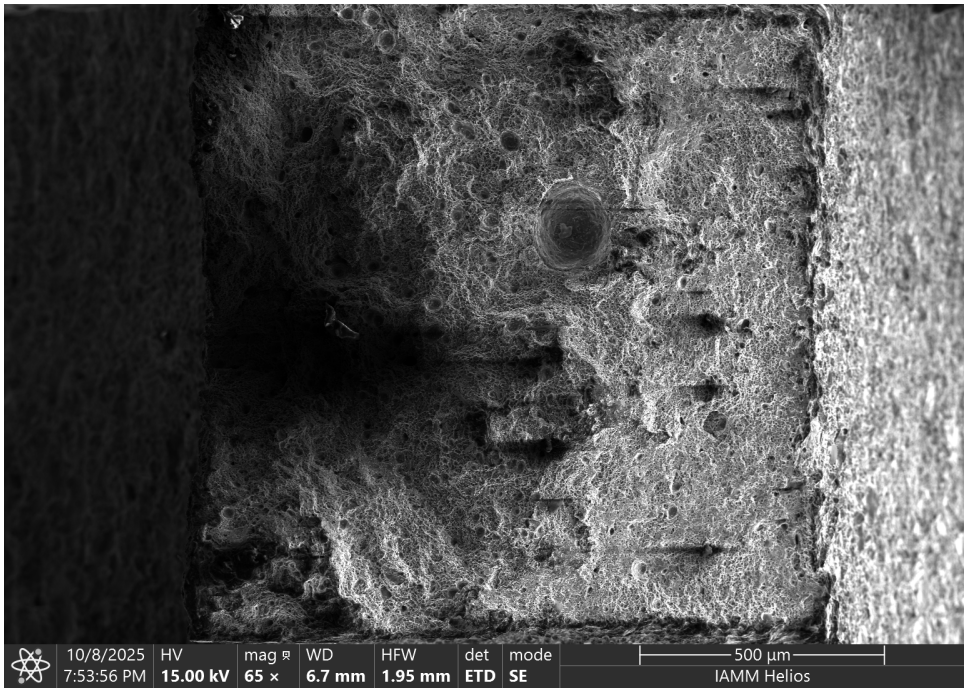


Figure 4.40: Fracture surface in the HT condition of the interface, where Al4943 was deposited on the machined AFSD side surface.

Chapter 5

Conclusions and Future Work

5.1 Conclusions

A novel Al6061-Al4943 MM was developed using a sequential AM approach. AFSD was used to deposit Al6061, then WAAM was used to deposit Al4943 onto the Al6061 deposit. Various MM deposit orientations were evaluated to determine how the anisotropic behavior from the AFSD process effects the interface properties. Material characterization of each alloy, as well as the interface, was achieved through metallography techniques and mechanical testing. Optical microscopy and SEM with EDS displayed different microstructure for both alloys in the AD and HT conditions. Heterogeneity was observed in the AD MM as each parent alloy displayed signs of overaging due to the additive processes. The precipitates were overaged or dissolutionized, due to the repeated thermal cycles during deposition. The interface region showed signs of dilution from the WAAM process into the Al6061. Homogeneity was observed in the HT conditions for both alloys where strengthening precipitates formed. The dilution between the alloys was still prevalent but not as pronounced. The mechanical properties verified these findings as the AD condition was much lower in all aspects when compared to the HT condition. In both conditions, a distinct transition across the interface, was observed. The structural integrity of the

interface presents no cause for concern, as it lacks evidence of significant defects or weaknesses. Microindentation hardness mapping showed that overaging of each alloy was observed in the AD condition, as the hardness increased in the build direction from about 30 mm from the top of the deposit. This was due to the repeated thermal cylces from both the WAAM process and AFSD process. The maximum hardness was measured at the interface of the two alloys. Whereas, the HT condition had a uniform hardness throughout each alloy, with a distinct change at the interface. The tensile properties reciprocated these findings, as the AD condition had low tensile strength with higher ductility in both alloys. The HT condition exhibited improved tensile strength in both alloys with the Al4943 meeting wrought Al6061-T6 properties. The interface region was verified to exceed the mechanical performance of the weaker alloy. A modified tensile specimen, incorporating an increased gage length to fully capture the overaged region of the Al6061, confirmed that failure consistently occurred within the Al6061 rather than at the interface. This approach, of creating a MM utilizing AFSD and WAAM sequentially, is effective as evidenced that the weaker parent alloy will fail before the interface.

When printing large components that are made up of only one material, choosing the best additive process is essential. Specifically, when depositing large aluminum structures, when deciding between AFSD to deposit Al6061 or WAAM to deposit Al4943, considerations must be taken into account. While Al6061 AFSD enables higher deposition rates of 2.12 kg/hr, the mechanical properties from the Al4943 WAAM are superior and only have a slightly lower deposition rate of 1.46 kg/hr. Cycle times for printing large components are usually insignificant as lead times from traditional manufacturing methods can reach up to eighteen months. However, AFSD deposited Al6061 45.2% faster than WAAM deposited Al4943. Component size, print time and desired material properties must all be accounted for when deciding the optimal additive process and alloy to the print the component with.

To proceed with developing a component that utilizes this sequential AM approach, with Al6061 deposited via AFSD and Al4943 deposited via WAAM, a

T6 HT schedule must be followed. The AD condition exhibits anisotropic behavior and has low mechanical properties. The HT condition hardens and strengthens the material to come close to wrought Al6061-T6 properties. The interface region between the two alloys is deemed stronger than the weaker parent alloy. This provides evidence that this approach for developing a MM using sequential AM of AFSD and WAAM is effective.

5.2 Future work

To further develop this MM, more testing can be completed. The dilution zone at the interface of the MM can be measured to determine its size. This would establish a relationship of how the alloys interact based on the welding parameters used during the WAAM process. Understanding the dilution zone would give better feedback into the joining of the material. Other MM alloy combinations can be studied, where solid-state AM would be optimal. Dissimilar metals could also be evaluated if a large MM metal component is needed, as both of these additive processes are optimized for large scale AM.

Bibliography

[1] J. Weritz, *Aluminum Alloy Nomenclature and Temper Designations*, pp. 3–30. ASM International, 12 2018. xii, 6, 8

[2] J. Hirsch, *Annealing of Aluminum and Its Alloys*, pp. 137–147. ASM International, 12 2018. xii, 8

[3] J. G. Kaufman, *Properties and Applications of Wrought Aluminum Alloys*, pp. 202–275. ASM International, 6 2019. xii, 8

[4] D. S. MacKenzie, *Metallurgy of Heat Treatable Aluminum Alloys*, pp. 411–437. ASM International, 12 2018. xii, 6, 7, 8

[5] "Practice for heat treatment of wrought aluminum alloys," 12 2020. xii, 8

[6] H. Aluminum, "Certified material test report aws a5.01 schedule h, class s1," tech. rep. xii, 21

[7] H. Aluminum, "Certified material test report aws a5.01 schedule h, class s1," tech. rep. xii, 21

[8] Z. Shen, M. Zhang, D. Li, X. Liu, S. Chen, W. Hou, Y. Ding, Z. Sun, Y. Su, W. Li, and Y. Tian, "Microstructural characterization and mechanical properties of almg alloy fabricated by additive friction stir deposition," *International Journal of Advanced Manufacturing Technology*, vol. 125, pp. 2733–2741, 3 2023. xiv, 11

[9] K. Anderson-Wedge, D. Avery, S. Daniewicz, J. Sowards, P. Allison, J. Jordon, and R. Amaro, "Characterization of the fatigue behavior of additive friction stir-deposition aa2219," *International Journal of Fatigue*, vol. 142, p. 105951, 2021. xiv, 11

[10] P. C. Metz, C. Franz, J. Kincaid, T. Schmitz, E. A. Lass, S. S. Babu, and K. Page, "Heterogeneous microstructure development in additive friction-stir deposited al-mg-si alloy," *Additive Manufacturing*, vol. 81, 2 2024. xiv, 12, 14

[11] L. P. Cahalan, M. B. Williams, L. N. Brewer, M. M. McDonnell, M. R. Kelly, A. D. Lalonde, P. G. Allison, and J. B. Jordon, "Parametric investigation of parallel deposition passes on the microstructure and mechanical properties of 7075 aluminum alloy processed with additive friction stir deposition," *Applied Sciences (Switzerland)*, vol. 14, 1 2024. xiv, 13, 16

[12] V. Yakubov, H. Ostergaard, S. Bhagavath, C. L. A. Leung, J. Hughes, E. Yasa, M. Khezri, S. K. Löschke, Q. Li, and A. M. Paradowska, "Multimodal defect analysis and application of virtual machining for solid-state manufactured aluminium structure," *Progress in Additive Manufacturing*, 2024. xiv, xviii, 12, 17, 18, 51, 142

[13] "Hobart maxal 4943," tech. rep. xiv, 19, 21, 30

[14] R. Singh, *Arc Welding Processes Handbook*. John Wiley & Sons, Incorporated, 2021. xiv, 20, 23

[15] G. Metzger, "Some mechanical properties of welds in 6061 aluminum alloy sheet," *Welding Journal*, vol. 56, pp. 457–s, 1967. xiv, 22, 25

[16] M. Ahmed, M. Javidani, F. Mirakhorli, A. Maltais, and X. G. Chen, *Novel High-Strength Al-Si-Mg Filler Wires for Aluminum Welding*, pp. 331–340. Springer Nature Switzerland, 2023. xiv, 27, 28, 116

[17] Z. qiang Liu, P. lei Zhang, S. wei Li, D. Wu, and Z. shui Yu, "Wire and arc additive manufacturing of 4043 al alloy using a cold metal transfer method," *International Journal of Minerals, Metallurgy and Materials*, vol. 27, no. 6, pp. 783–791, 2020. xiv, 32, 33, 72, 80

[18] Z. Kallien, E. Eimer, A. Roos, V. Ortolland, L. Rath, S. Williams, and B. Klusemann, "Combining fusion-based and solid-state additive manufacturing: Investigation of additive ded structures with friction surfacing interlayer," *Additive Manufacturing Letters*, vol. 14, p. 100302, 2025. xiv, 35, 36, 37

[19] L. Liu, Z. Zhuang, F. Liu, and M. Zhu, "Additive manufacturing of steel-bronze bimetal by shaped metal deposition: Interface characteristics and tensile properties," *International Journal of Advanced Manufacturing Technology*, vol. 69, pp. 2131–2137, 12 2013. xiv, 35, 37

[20] A. Gibian, "Viewpoint$_u$.s.$forgingcompaniesoverlookedfortoolong$,″ 2024.1

[21] H. Dong, X. Li, K. Xu, Z. Zang, X. Liu, Z. Zhang, W. Xiao, and Y. Li, "A review on solid-state-based additive friction stir deposition," *Aerospace*, vol. 9, no. 10, 2022. 2, 29

[22] "Additive manufacturing-general principles-fundamentals and vocabulary 1,2," tech. rep. 4

[23] T. Childerhouse and M. Jackson, "Near net shape manufacture of titanium alloy components from powder and wire: A review of state-of-the-art process routes," 6 2019. 4

[24] I. Gibson, D. Rosen, B. Stucker, and M. Khorasani, "Additive manufacturing technologies," tech. rep. 5

[25] J. C. Williams and E. A. Starke, "Progress in structural materials for aerospace systems," *Acta Materialia*, vol. 51, pp. 5775–5799, 11 2003. 5

[26] T. He, S. Yu, Y. Shi, and A. Huang, "Forming and mechanical properties of wire arc additive manufacture for marine propeller bracket," *Journal of Manufacturing Processes*, vol. 52, pp. 96–105, 2020. 5

[27] B. Blakey-Milner, P. Gradl, G. Snedden, M. Brooks, J. Pitot, E. Lopez, M. Leary, F. Berto, and A. du Plessis, "Metal additive manufacturing in aerospace: A review," *Materials Design*, vol. 209, p. 110008, 2021. 5

[28] S. Kou, "A criterion for cracking during solidification," *Acta Materialia*, vol. 88, pp. 366–374, 4 2015. 7

[29] N. Coniglio and C. E. Cross, "Initiation and growth mechanisms for weld solidification cracking," *International Materials Reviews*, vol. 58, pp. 375–397, 2013. 7

[30] A. Mehta, L. Zhou, T. Huynh, S. Park, H. Hyer, S. Song, Y. Bai, D. D. Imholte, N. E. Woolstenhulme, D. M. Wachs, and Y. Sohn, "Additive manufacturing and mechanical properties of the dense and crack free zr-modified aluminum alloy 6061 fabricated by the laser-powder bed fusion," *Additive Manufacturing*, vol. 41, 5 2021. 7

[31] M. Rosito, M. Vanzetti, E. Padovano, F. Gili, R. Sampieri, F. Bondioli, and C. F. Badini, "Processability of a6061 aluminum alloy using laser powder bed fusion by in situ synthesis of grain refiners," *Metals*, vol. 13, 6 2023. 7

[32] T. Fedotowsky, B. Williams, P. Gradl, and D. Tinker, "Al6061-ram2 development and hot-fire testing using additive manufacturing laser powder directed energy deposition for liquid rocket engine channel-cooled nozzles," 01 2024. 9

[33] M. R. Rokni, C. A. Widener, O. C. Ozdemir, and G. A. Crawford, "Microstructure and mechanical properties of cold sprayed 6061 al in as-sprayed and heat treated condition," *Surface and Coatings Technology*, vol. 309, pp. 641–650, 1 2017. 9

[34] Nirmal, "Evaluation of physical and mechanical properties of cold sprayed al6061," tech. rep., 2024. 9

[35] H. Gao, P. Dong, and Z. Wei, "Microstructure and properties of 6061 aluminum alloy by additive friction stir deposition," *Metals*, vol. 15, 5 2025. 9, 15, 17, 19, 70, 89, 100

[36] L. Chen, L. Lu, L. Zhu, Z. Yang, W. Zhou, X. Ren, and X. Zhang, "Microstructure evolution and mechanical properties of multilayer aa6061 alloy fabricated by additive friction stir deposition," *Metallurgical and Materials Transactions A: Physical Metallurgy and Materials Science*, vol. 55, pp. 1049–1064, 4 2024. 9, 80, 89

[37] H. Z. Yu, M. E. Jones, G. W. Brady, R. J. Griffiths, D. Garcia, H. A. Rauch, C. D. Cox, and N. Hardwick, "Non-beam-based metal additive manufacturing enabled by additive friction stir deposition," *Scripta Materialia*, vol. 153, pp. 122–130, 8 2018. 9

[38] S. Palanivel and R. S. Mishra, "Building without melting: a short review of friction-based additive manufacturing techniques melting: a short review of friction-based additive manufacturing techniques," tech. rep., 2017. 9

[39] J. Gandra, H. Krohn, R. M. Miranda, P. Vilaça, L. Quintino, and J. F. D. Santos, "Friction surfacing - a review," 2014. 10

[40] L. Rath, Z. Kallien, A. Roos, J. F. Santos, and B. Klusemann, "Anisotropy and mechanical properties of dissimilar al additive manufactured structures generated by multi-layer friction surfacing," *International Journal of Advanced Manufacturing Technology*, vol. 125, pp. 2091–2102, 3 2023. 10

[41] Y. G. Elshaghoul, M. M. E.-S. Seleman, A. Bakkar, S. A. Elnekhaily, I. Albaijan, M. M. Ahmed, A. Abdel-Samad, and R. Reda, "Additive friction stir deposition of aa7075-t6 alloy: Impact of process parameters on the microstructures and properties of the continuously deposited multilayered parts," *Applied Sciences (Switzerland)*, vol. 13, 9 2023. 10

[42] "Meld manufacturing." 10

[43] H. Dong, X. Li, K. Xu, Z. Zang, X. Liu, Z. Zhang, W. Xiao, and Y. Li, "A review on solid-state-based additive friction stir deposition," 10 2022. 12

[44] J. Kincaid, E. Charles, R. Garcia, J. Dvorak, T. No, S. Smith, and T. Schmitz, "Process planning for hybrid manufacturing using additive friction stir deposition," *Manufacturing Letters*, vol. 37, pp. 26–31, 2023. 12

[45] L. Jiang, R. Varma, M. Ramajayam, T. Dorin, M. R. Barnett, and D. Fabijanic, "Effects of extreme deposition rate on the microstructure evolution of additive friction stir deposited aa6061 alloy," *Additive Manufacturing Letters*, vol. 13, 4 2025. 12

[46] gang chen, K. Wu, Y. Wang, Z.-X. Zhu, P. Nie, and F.-F. Hu, "Effect of rotational speed and feed rate on microstructure and mechanical properties of 6061 aluminum alloy manufactured by additive friction stir deposition," 10 2022. 13

[47] B. Phillips, C. Mason, S. Beck, D. Avery, K. Doherty, P. Allison, and J. Jordon, "Effect of parallel deposition path and interface material flow on resulting microstructure and tensile behavior of al-mg-si alloy fabricated by additive friction stir deposition," *Journal of Materials Processing Technology*, vol. 295, p. 117169, 2021. 13, 106

[48] Y. Li, H. Wang, R. Lai, B. Yang, Z. Wang, and Y. Li, "Effect of overlapping deposition strategy on microstructure and mechanical properties of al-clad steel by afsd," *Journal of Manufacturing Processes*, vol. 129, pp. 51–61, 11 2024. 13

[49] J. P. Kincaid, "Automated path planning for additive friction stir deposition," tech. rep. 15

[50] K. Huang and R. E. Logé, "A review of dynamic recrystallization phenomena in metallic materials," 12 2016. 15

[51] C. Zeng, H. Ghadimi, H. Ding, S. Nemati, A. Garbie, J. Raush, and S. Guo, "Microstructure evolution of al6061 alloy made by additive friction stir deposition," *Materials*, vol. 15, 5 2022. 17, 19, 80, 84, 106

[52] Q. Qiao, C. Tang, W. Lam, J. Pu, H. Shi, H. Qian, Z. Li, D. Guo, D. Zhang, C. Kwok, and L. Tam, "Effect of heat input on microstructure and mechanical properties of

aa6061 alloys fabricated by additive friction stir deposition," *Journal of Materials Research and Technology*, vol. 33, pp. 6182–6195, 2024. 17, 89

[53] L. Chen, Y. Li, L. Lu, Z. Yang, X. Ren, and X. Zhang, "The effect of heat treatment on the microstructure and mechanical properties of multilayer aa6061 alloy fabricated by additive friction stir deposition," *Materials Today Communications*, vol. 38, p. 108078, 2024. 17, 19

[54] *New Development in Aluminum Welding Wire - Alloy 4943*, vol. SNAME Maritime Convention of *SNAME Maritime Convention*, 10 2012. 19

[55] D. Holliday, *Gas-Metal Arc Welding*, pp. 180–185. ASM International, 12 2018. 20, 22

[56] P. B. Dickerson, *Welding of Aluminum Alloys*, pp. 722–739. ASM International, 12 2018. 22

[57] A. W. Society, "By authority of the united states of america legally binding document," tech. rep. 22

[58] I. Guzmán, E. Granda, J. Acevedo, A. Martínez, Y. Dávila, and R. Velázquez, "Comparative in mechanical behavior of 6061 aluminum alloy welded by pulsed gmaw with different filler metals and heat treatments," *Materials*, vol. 12, no. 24, 2019. 24

[59] P. STATHERS, A. Hellier, R. Harrison, M. Ripley, and J. Norrish, "Hardness-tensile property relationships for haz in 6061-t651 aluminum," *Welding journal*, vol. 93, pp. 301–s to 311, 08 2014. 24

[60] C. Sagar, P. Kumar, and P. K. Verma, "A study of microstructures of gas metal arc welded aluminium alloy 6061-t6," *IJIRST-International Journal for Innovative Research in Science & Technology—*, vol. 3, 2016. 26

[61] M. Ahmed, M. Javidani, F. Mirakhorli, A. Maltais, and X. G. Chen, "Developing high-strength al-si-mg filler metals for aluminum fusion welding," *Journal of Materials Engineering and Performance*, vol. 32, pp. 2218–2227, 3 2023. 26, 91

[62] B. Anderson, T. Anderson, G. White, and P. Berube, "P16 new development in aluminum welding wire-alloy 4943," tech. rep. 26

[63] M. Ahmed, M. Javidani, A. Maltais, and X. G. Chen, "Microstructure and mechanical properties of high-strength aa6011 aluminum alloy welding with novel 4xxx filler metals," *Materials*, vol. 17, 1 2024. 27

[64] Y. Li, C. Su, and J. Zhu, "Comprehensive review of wire arc additive manufacturing: Hardware system, physical process, monitoring, property characterization, application and future prospects," *Results in Engineering*, vol. 13, p. 100330, 3 2022. 27

[65] C. G. Pickin and K. Young, "Evaluation of cold metal transfer (cmt) process for welding aluminium alloy," *Science and Technology of Welding and Joining*, vol. 11, pp. 583–585, 9 2006. 29

[66] T. Ouellet, M. Croteau, A. Bois-Brochu, and J. Lévesque, "Wire arc additive manufacturing of aluminium alloys †," *Engineering Proceedings*, vol. 43, 2023. 29, 30, 101

[67] A. S. Haselhuhn, M. W. Buhr, B. Wijnen, P. G. Sanders, and J. M. Pearce, "Structure-property relationships of common aluminum weld alloys utilized as feedstock for gmaw-based 3-d metal printing," *Materials Science and Engineering: A*, vol. 673, pp. 511–523, 2016. 29, 30, 72

[68] M. Wieczorowski, A. Pereira, D. Carou, B. Gapinski, and I. Ramírez, "Characterization of 5356 aluminum walls produced by wire arc additive manufacturing (waam)," *Materials*, vol. 16, 4 2023. 31

[69] E. Aldalur, A. Suárez, and F. Veiga, "Metal transfer modes for wire arc additive manufacturing al-mg alloys: Influence of heat input in microstructure and porosity," *Journal of Materials Processing Technology*, vol. 297, 11 2021. 31

[70] J. Wang, K. Zhu, W. Zhang, X. Zhu, and X. Lu, "Microstructural and defect evolution during waam resulting in mechanical property differences for aa5356 component," *Journal of Materials Research and Technology*, vol. 22, pp. 982–996, 1 2023. 31, 72, 80

[71] S. Li, L. J. Zhang, J. Ning, X. Wang, L. L. Zhang, J. Long, X. R. Zhou, and S. J. Na, "Microstructures and properties of wire-arc additively manufactured 5356 aluminium alloy protected by different proportions of nitrogen and argon," *Journal of Materials Science*, vol. 56, pp. 17785–17804, 11 2021. 31

[72] Y. Wang, S. Yang, C. Xie, H. Liu, and Q. Zhang, "Microstructure and ratcheting behavior of additive manufactured 4043 aluminum alloy," *Journal of Materials Engineering and Performance*, vol. 27, pp. 4582–4592, 9 2018. 32

[73] A. Ortega, L. Galvan, M. Salem, K. Moussaoui, S. Segonds, S. Rouquette, and F. Deschaux-Beaume, "Characterisation of 4043 aluminium alloy deposits obtained by wire and arc additive manufacturing using a cold metal transfer process," *Science and Technology of Welding and Joining*, vol. 24, pp. 1–10, 01 2019. 32, 72

[74] G. Campatelli, D. Campanella, A. Barcellona, L. Fratini, N. Grossi, and G. Ingarao, "Microstructural, mechanical and energy demand characterization of alternative waam techniques for al-alloy parts production," *CIRP Journal of Manufacturing Science and Technology*, vol. 31, pp. 492–499, 2020. 32

[75] J. Gu, S. Yang, M. Gao, J. Bai, and K. Liu, "Influence of deposition strategy of structural interface on microstructures and mechanical properties of additively manufactured al alloy," *Additive Manufacturing*, vol. 34, 8 2020. 34

[76] E. Eimer, S. Williams, J. Ding, S. Ganguly, and B. Chehab, "Effect of substrate alloy type on the microstructure of the substrate and deposited material interface in aluminium wire + arc additive manufacturing," *Metals*, vol. 11, 6 2021. 34

[77] E. Eimer, S. Williams, J. Ding, S. Ganguly, and B. Chehab, "Mechanical performances of the interface between the substrate and deposited material in aluminium wire direct energy deposition," *Materials and Design*, vol. 225, 1 2023. 34

[78] T. Hauser, R. T. Reisch, S. Seebauer, A. Parasar, T. Kamps, R. Casati, J. Volpp, and A. F. Kaplan, "Multi-material wire arc additive manufacturing of low and high alloyed aluminium alloys with in-situ material analysis," *Journal of Manufacturing Processes*, vol. 69, pp. 378–390, 2021. 35, 108

[79] "Practice for heat treatment of wrought aluminum alloys," 12 2020. 54

[80] "Test methods for tension testing of metallic materials," 1 2024. 57

[81] "Guide for preparation of metallographic specimens," 8 2025. 62

[82] "Test method for microindentation hardness of materials," 10 2022. 65

[83] J. DuPont, *Dilution in Fusion Welding*, pp. 115–121. ASM International, 12 2018. 79

[84] N. Raghukiran, A. K. Mohamed, and R. Kumar, "Study of the influence of silicon phase morphology on the microstructural stress distribution in al-si alloys using object oriented finite element modeling," *Advanced Engineering Materials*, vol. 16, pp. 112–121, 1 2014. 88

Appendix A

Figures and Tables

A.1 Literature review

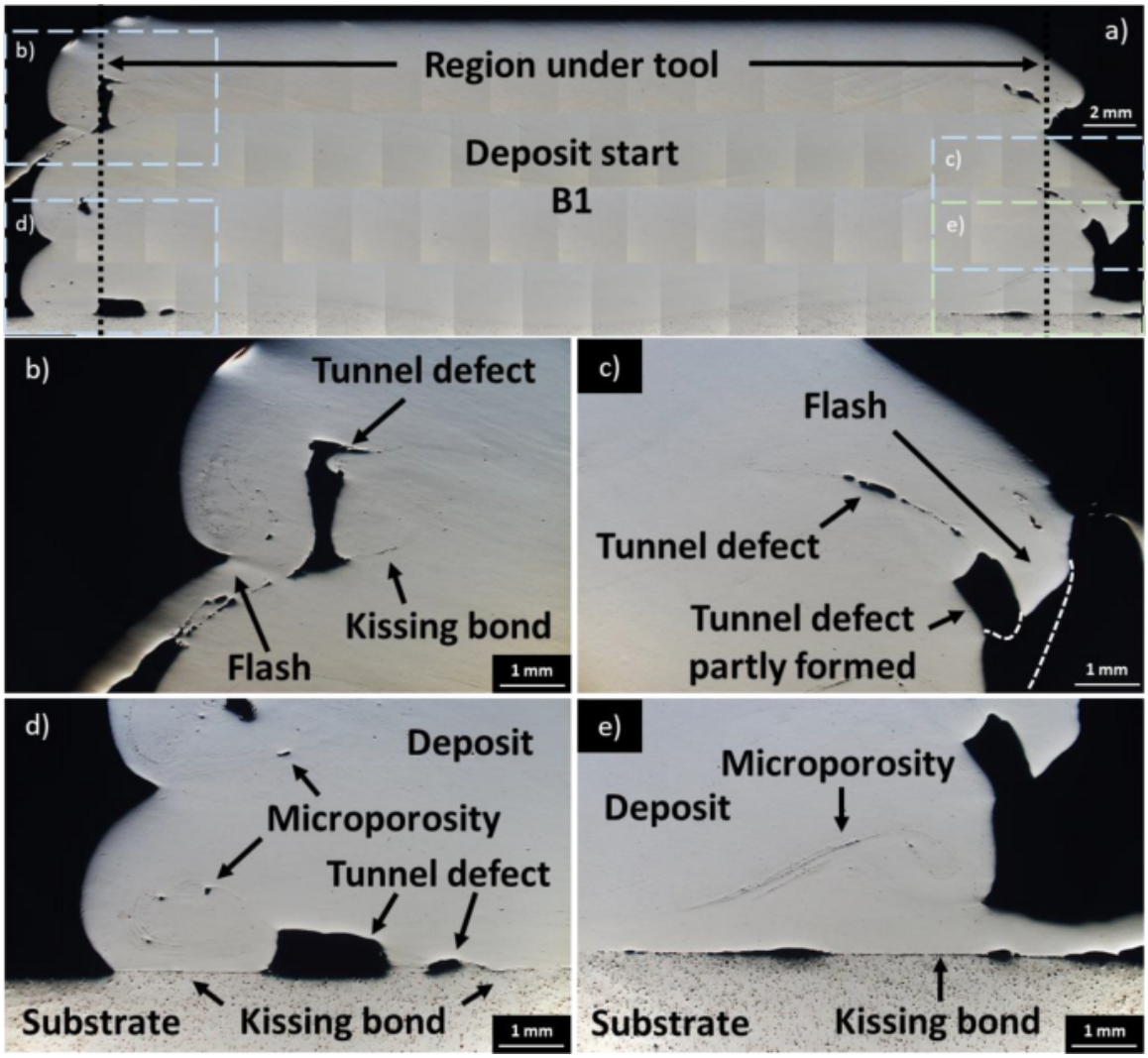
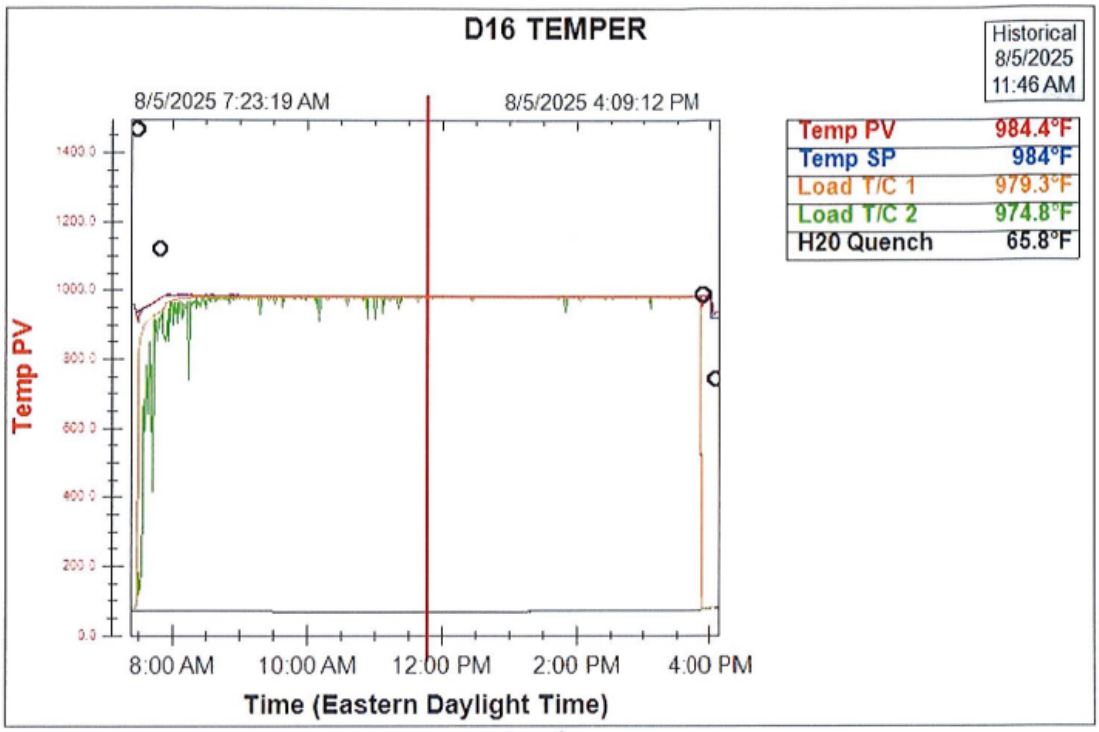


Figure A.1: Cross section of a starting location of an AFSD deposit with the uncertainty zone along the edges of the build (12).

A.2 Materials and methods

A.2.1 Heat treatment certification

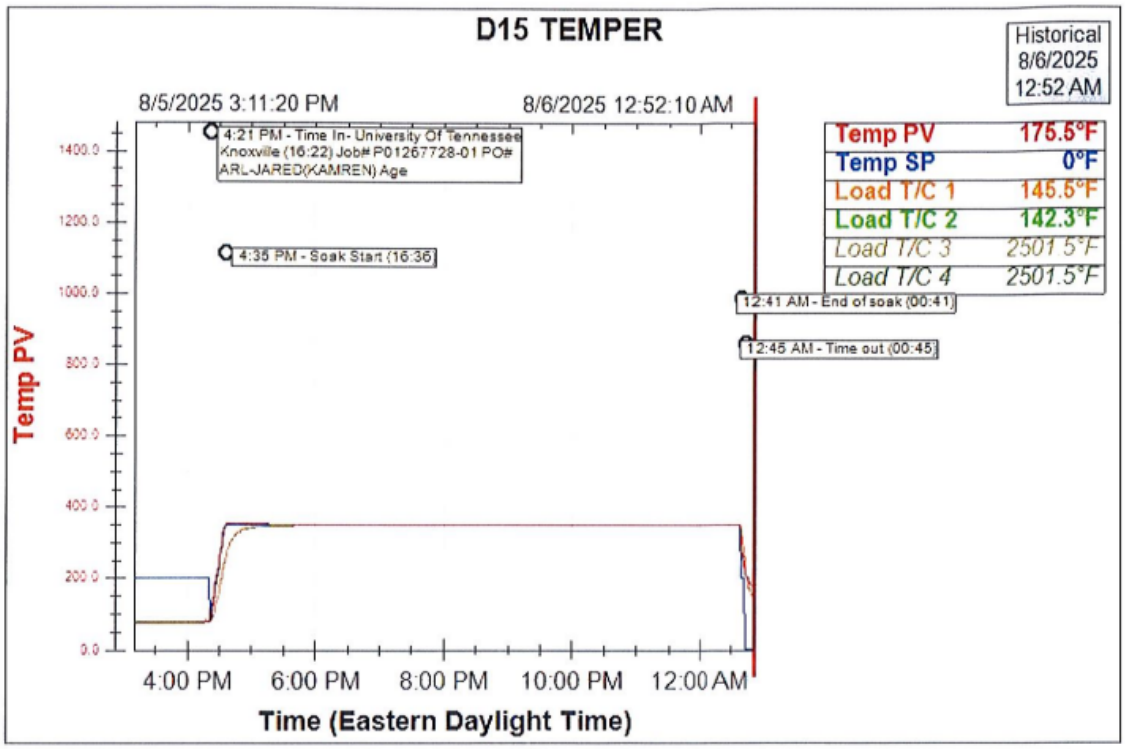


OK [illegible]
8/6/25

Note Section

Note Time	Time Created	Note
8/5/2025		
7:28 AM	8/5/2025 4:33:49 PM	Time In- University OF Tennessee Knoxville (07:29) Job# P01267728-01 PO# ARL-JARED (KAMREN) Water Solution and WQ [P.Dehayes] •
7:48 AM	8/5/2025 4:34:06 PM	Soak Start (07:49) [P.Dehayes] •
3:55 PM	8/5/2025 4:35:01 PM	Soak End, Starting Water Temp: 67.2F (15:55) [P.Dehayes] •
4:05 PM	8/5/2025 4:35:33 PM	Time Out Of Quench, Max Water Temp: 78.2F (16:05) [P.Dehayes] •

Figure A.2: Temperature vs time during the solution and quenching steps of the heat treatment T6 process.



Note Section

OK JSD 8/6/25

Note Time	Time Created	Note
8/5/2025		
4:21 PM	8/5/2025 4:39:11 PM	Time In- University Of Tennessee Knoxville (16:22) Job# P01267728-01 PO# ARL-JARED (KAMREN) Age [P.Dehayes] .
4:35 PM	8/5/2025 4:43:15 PM	Soak Start (16:36) [P.Dehayes] .
8/6/2025		
12:41 AM	8/6/2025 12:48:41 AM	End of soak (00:41) [R.Leopard] .
12:45 AM	8/6/2025 12:51:45 AM	Time out (00:45) [R.Leopard] .

Figure A.3: Temperature vs time during the artificial aging step of the heat treatment T6 process.

A.2.2 Sample Extraction

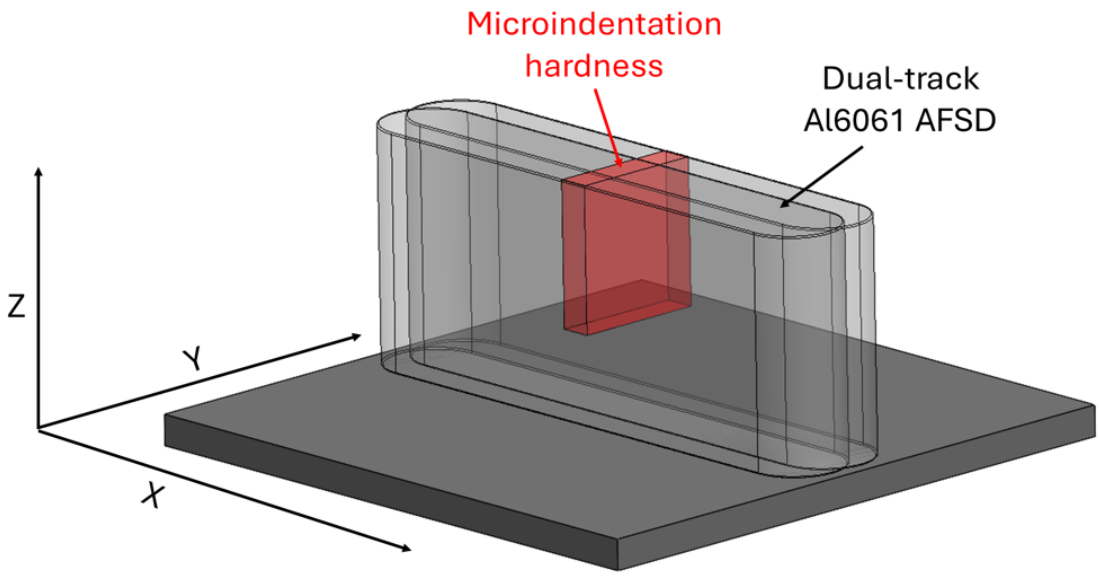


Figure A.4: Extraction site of microindentation hardness sample from an Al6061 AFSD dual-track wall.

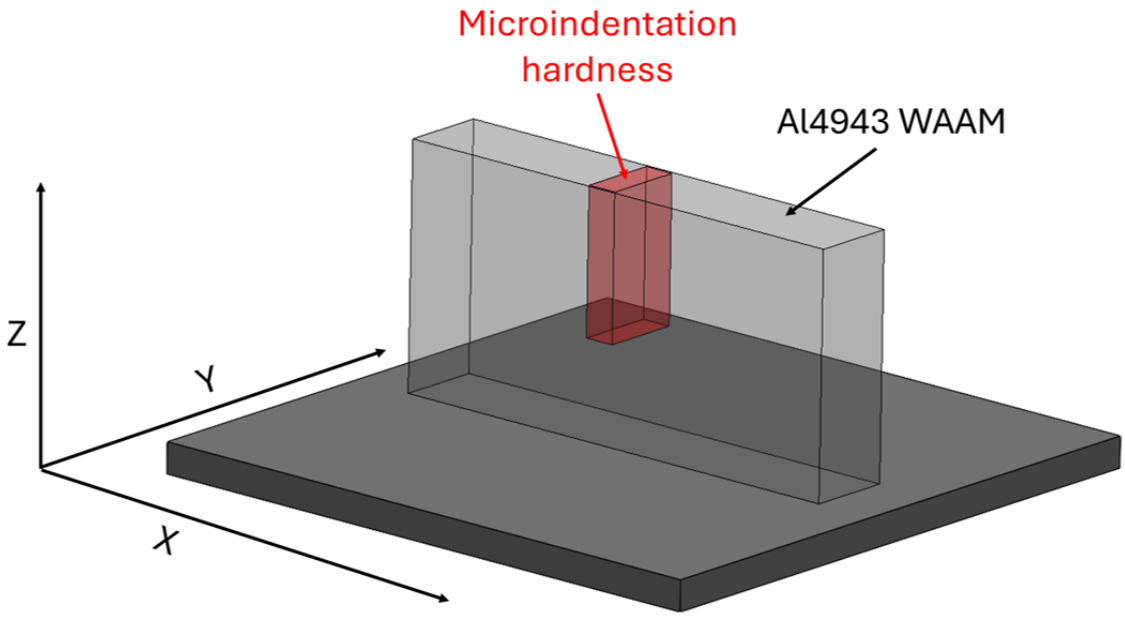


Figure A.5: Extraction site of microindentation hardness sample from an Al4943 WAAM wall.

A.3 Results and Discussion

A.3.1 Surface Roughness

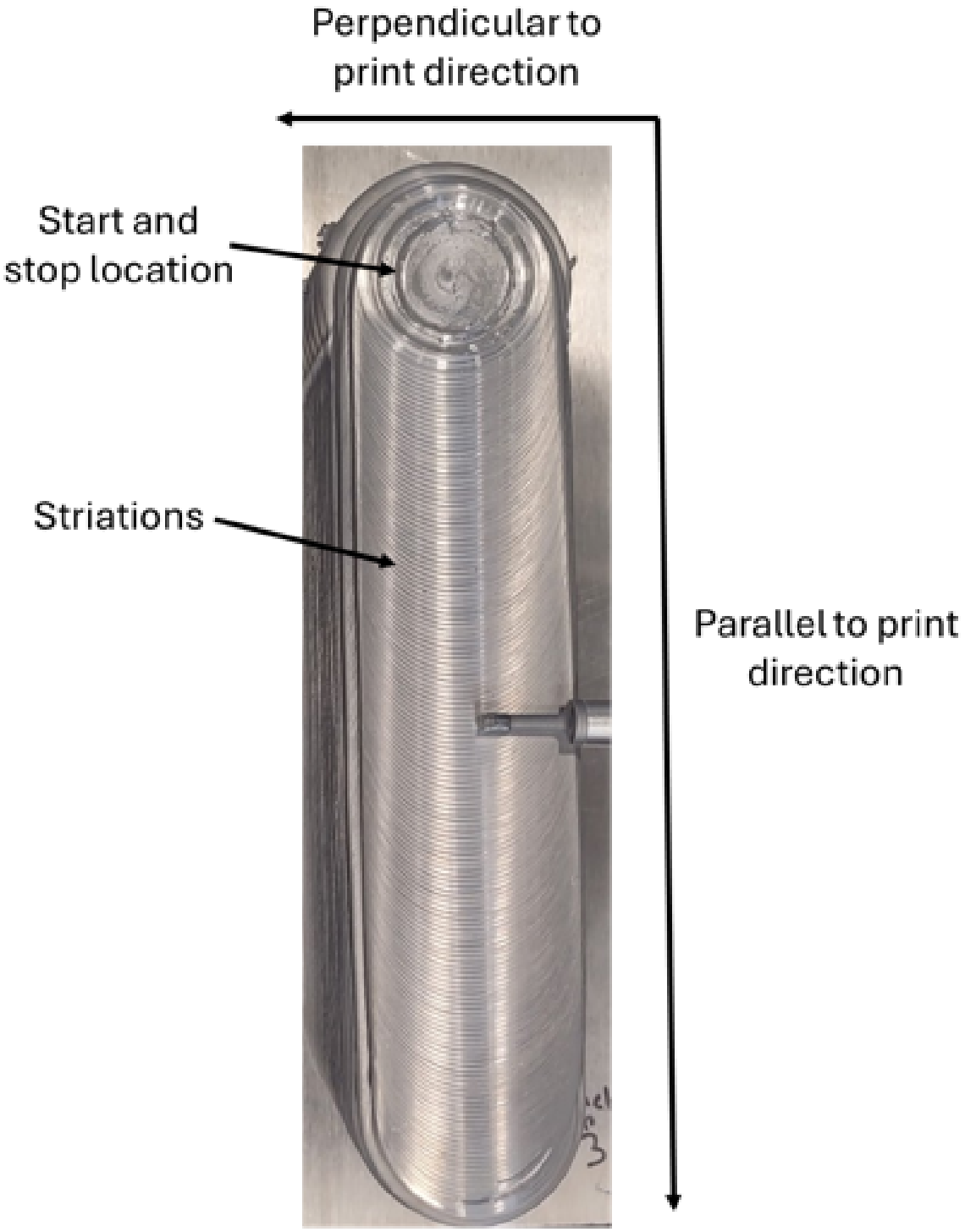


Figure A.6: Surface roughness from the Al6061 AFSD AD top surface.

A.3.2 Optical Microscopy

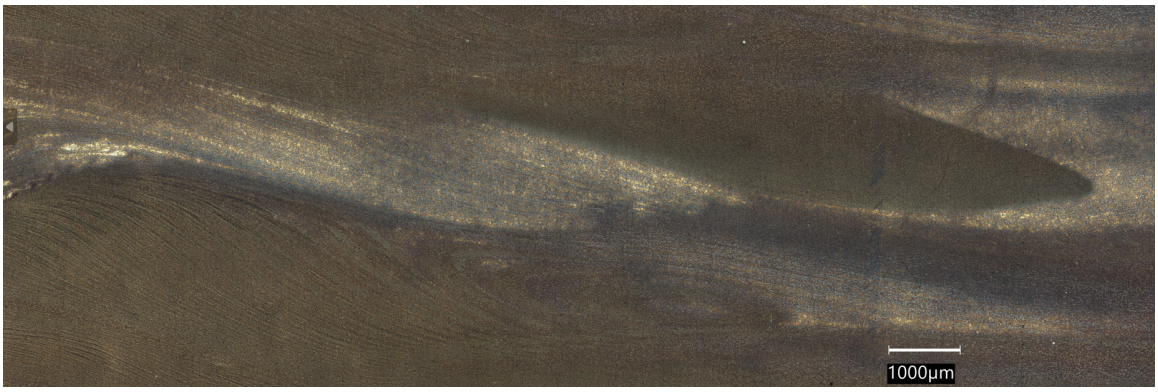


Figure A.7: Stitched image of the etched Al6061 deposited via AFSD in the AD condition.

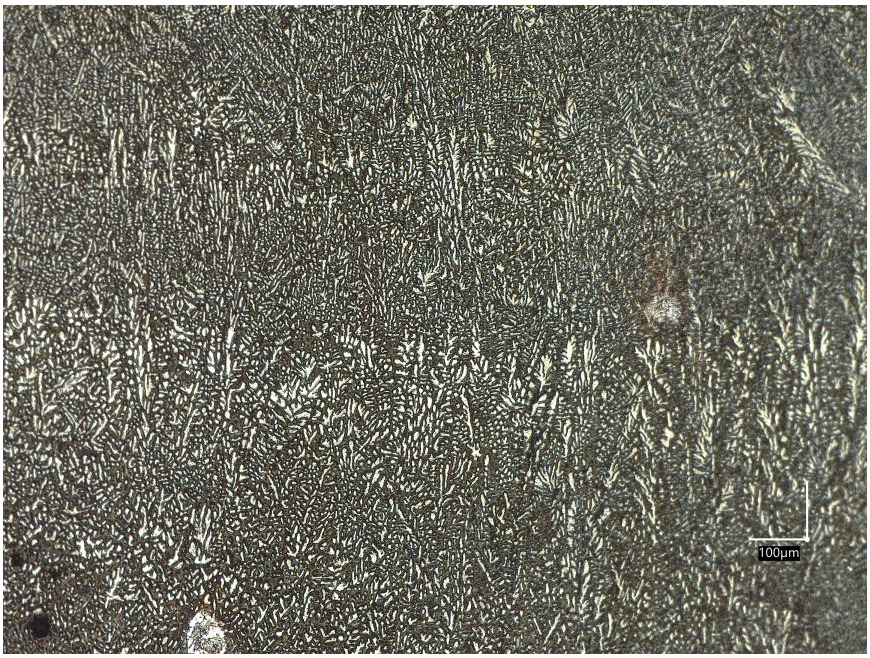


Figure A.8: Grain structure of Al4943 material deposited via WAAM in the AD condition.

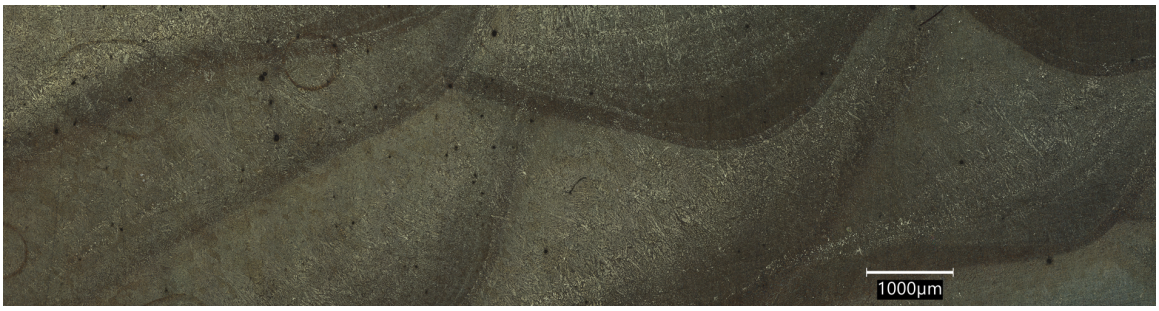


Figure A.9: Stitched image of the etched Al4943 deposited via WAAM in the AD condition.

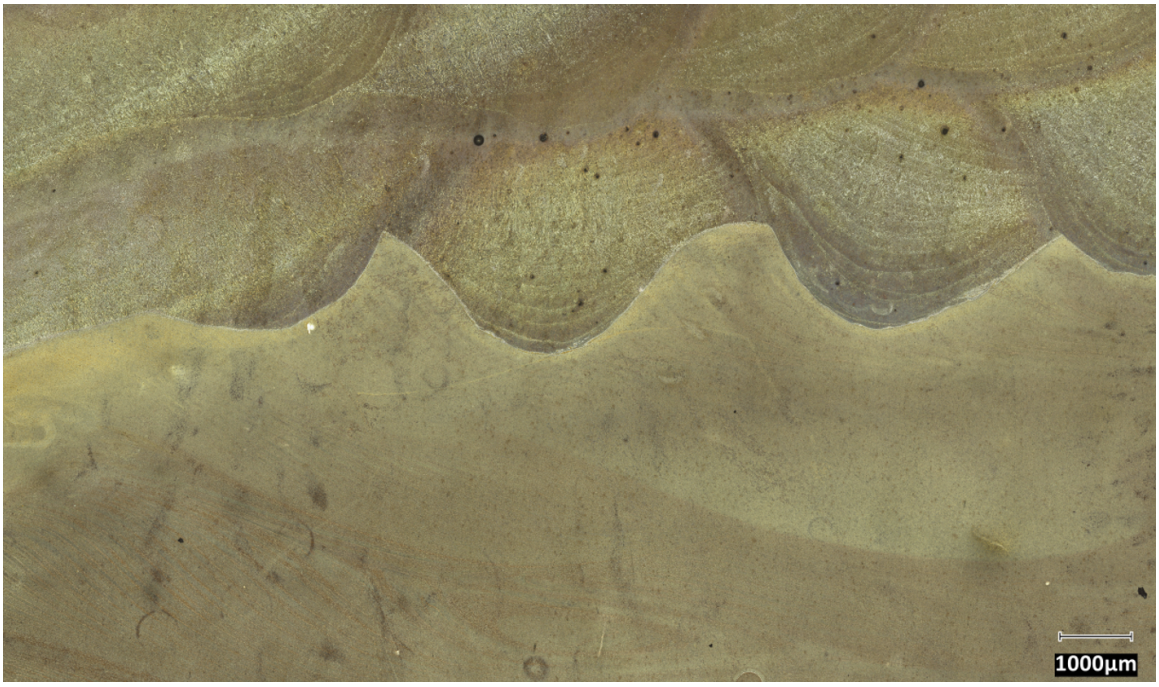


Figure A.10: Stitched image of the etched Al6061-Al4943 interface deposited in the AD condition.

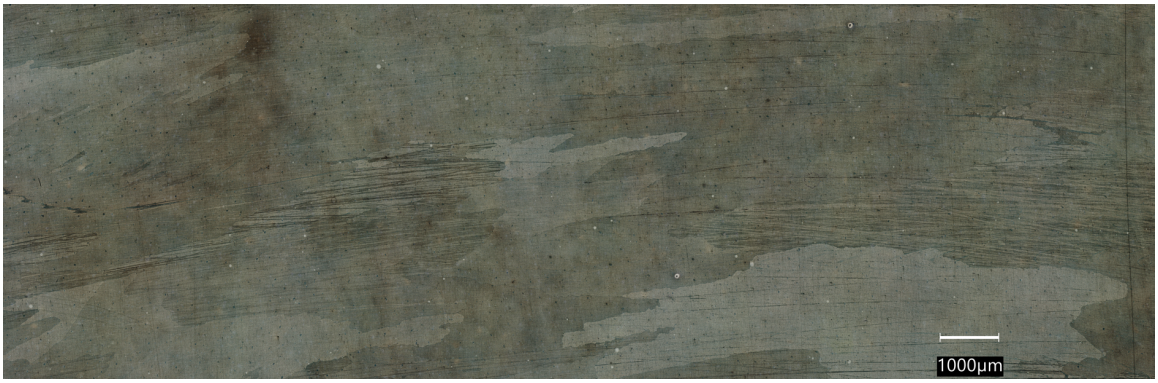


Figure A.11: Stitched image of the etched Al6061 deposited via AFSD in the HT condition.

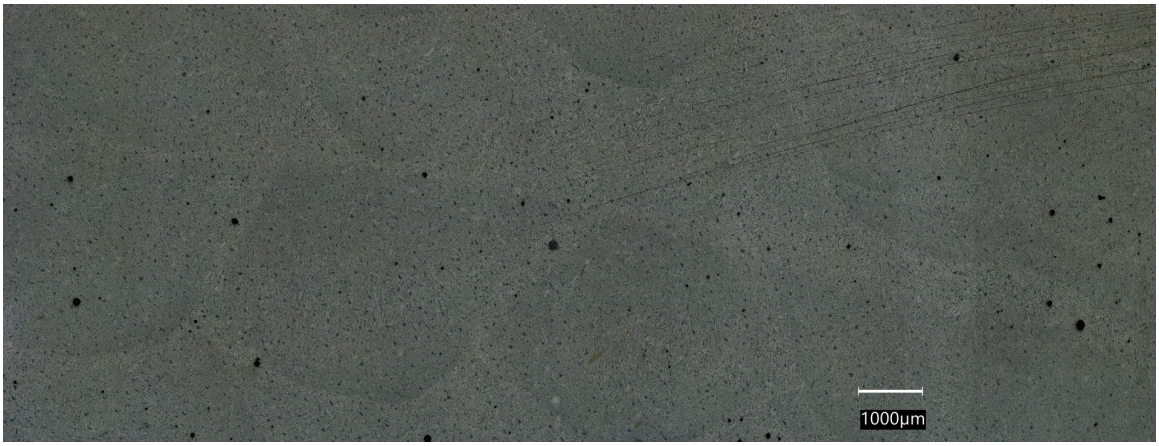


Figure A.12: Stitched image of the etched Al4943 deposited via WAAM in the HT condition.

A.3.3 SEM

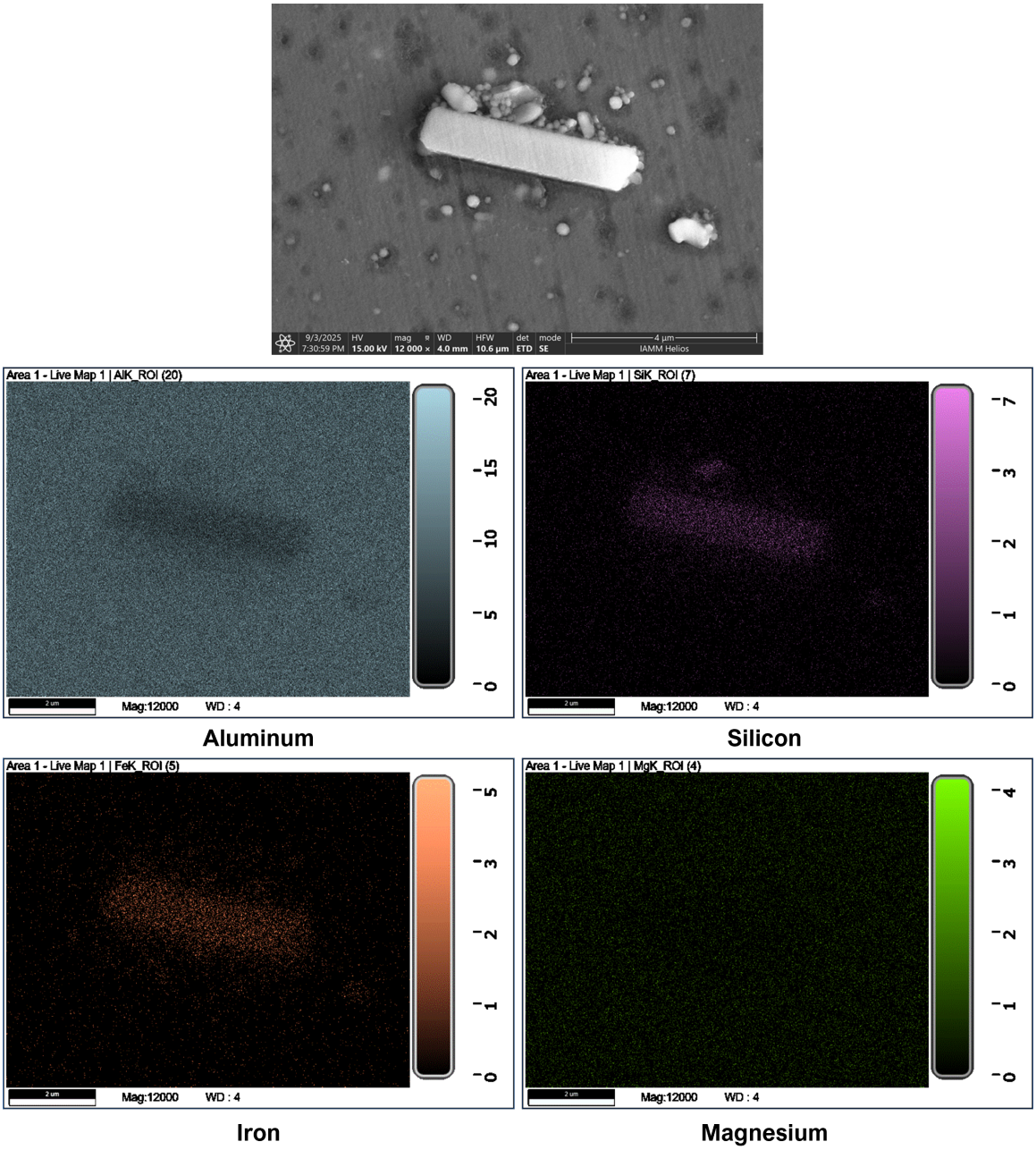


Figure A.13: Iron rich intermetallic found during SEM with EDS of Al6061 deposited via AFSD post HT process.

A.3.4 Microindentation hardness testing

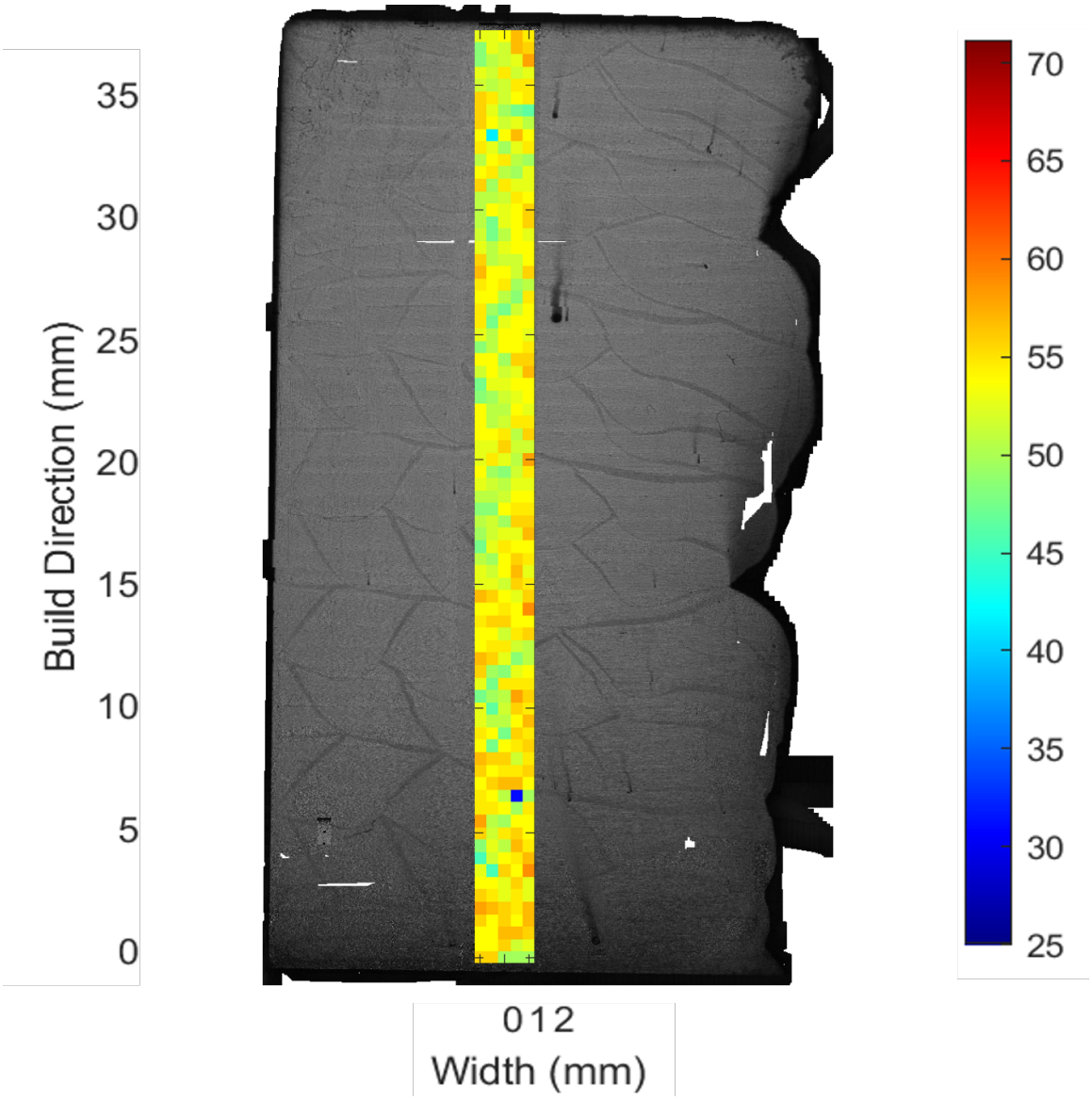


Figure A.14: Microindentation hardness across an AD Al4943 WAAM sample.

Table A.1: Average microindentation hardness for each parent alloy in the AD and HT condition.

Print Condition	**Hardness (HV)**
AD Al6061 AFSD	42
HT Al6061 AFSD	110
AD Al4943 WAAM	50
HT Al4943 WAAM	105
Wrought Al6061-T6	107

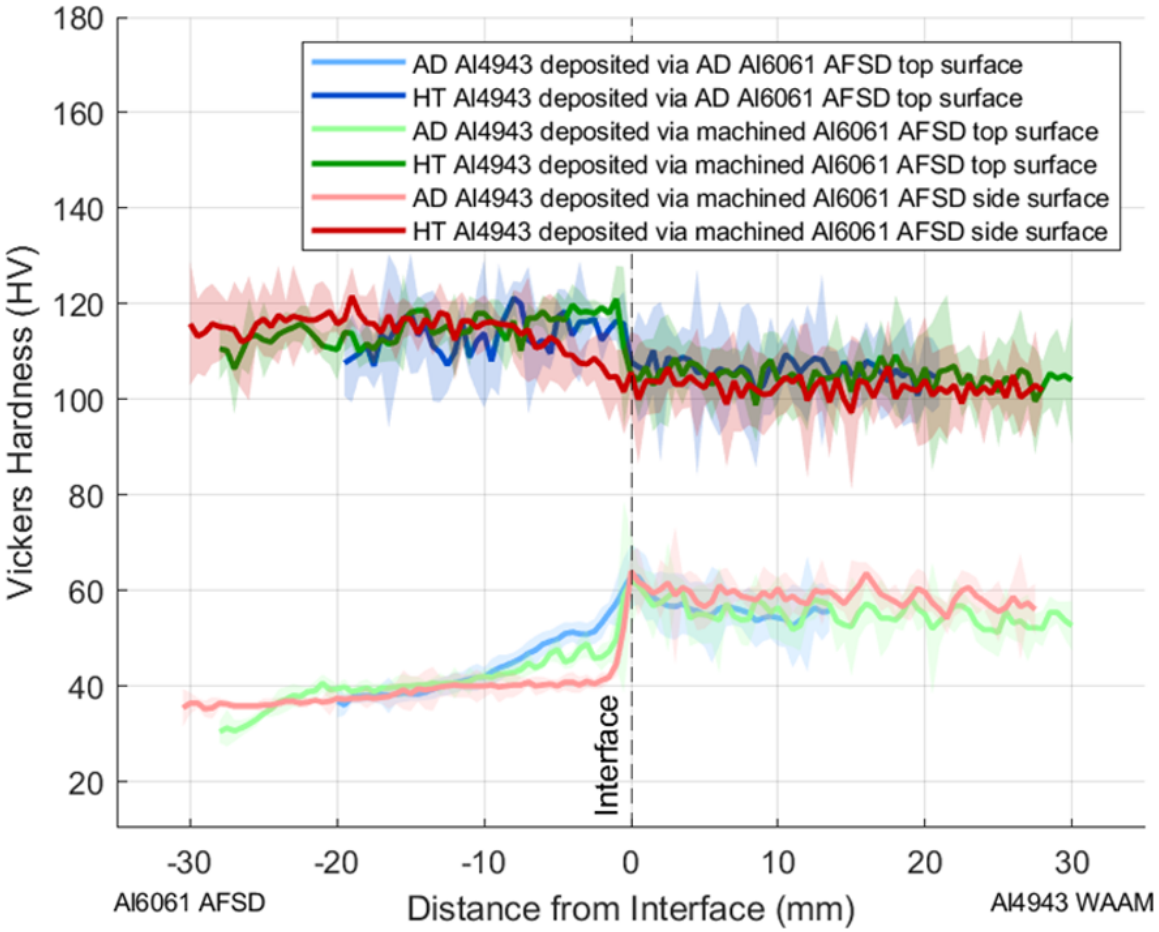


Figure A.15: Average microindentation hardness with two standard deviation across all MM deposits with various conditions.

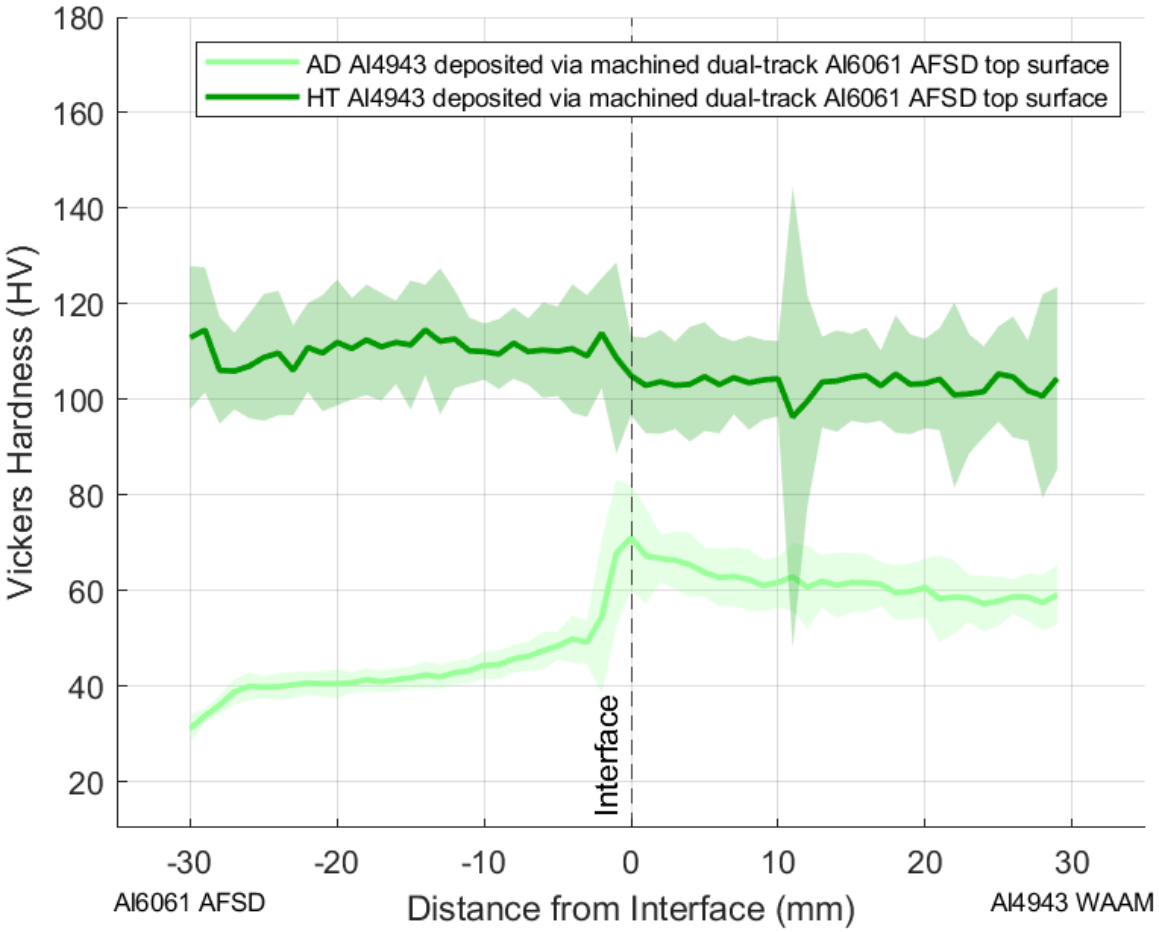


Figure A.16: Average microindentation hardness with two standard deviation across all dual-track MM deposits with various conditions.

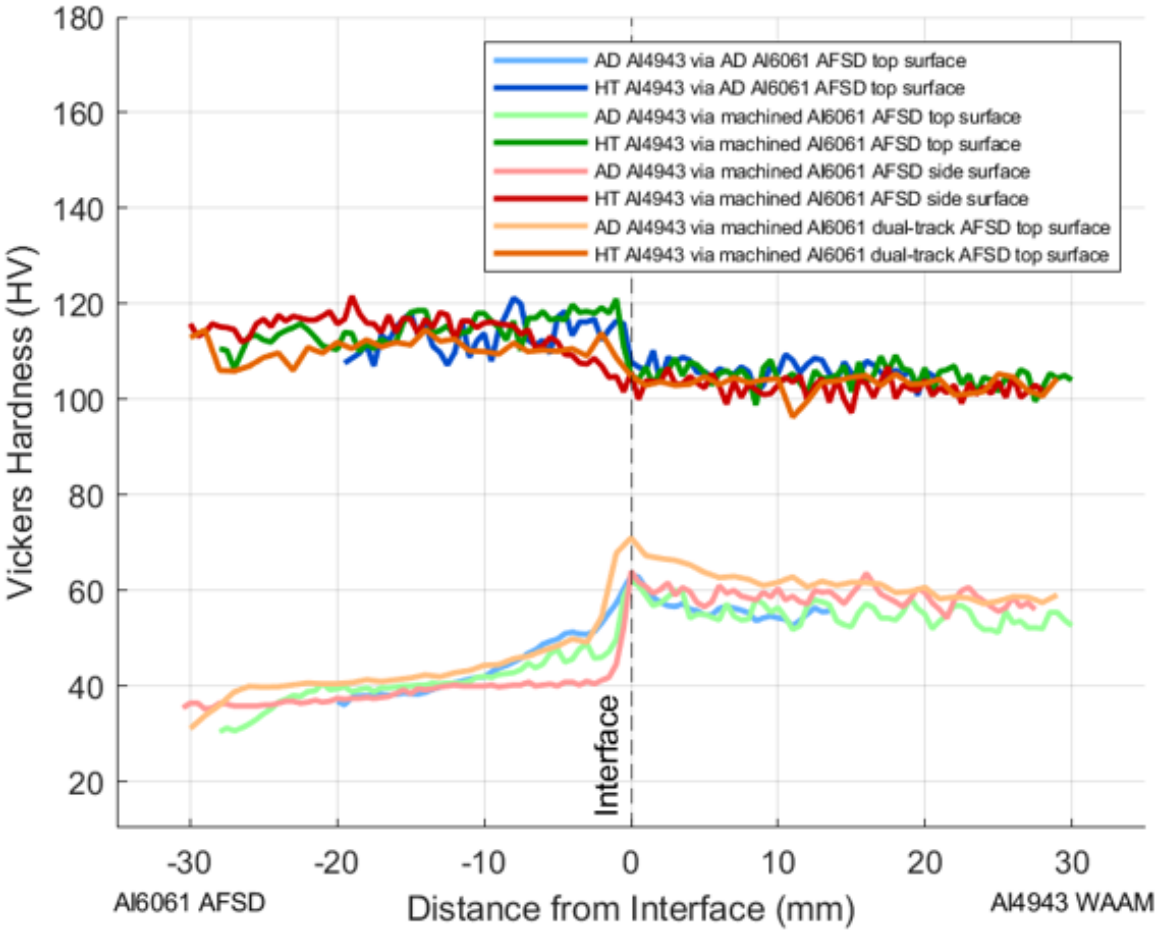


Figure A.17: Average microindentation hardness across all MM deposits with various conditions.

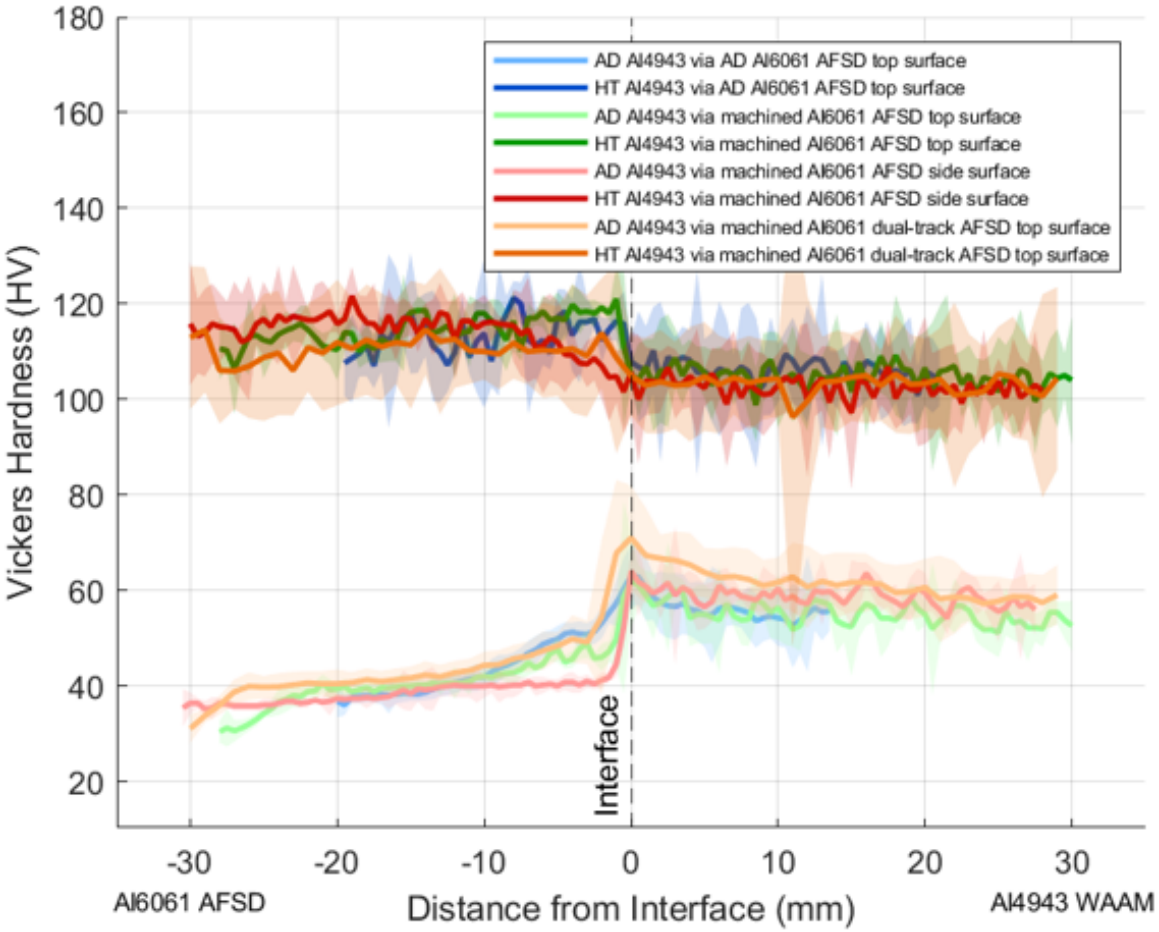


Figure A.18: Average microindentation hardness with two standard deviation across all MM deposits with various conditions.

A.3.5 Tensile testing

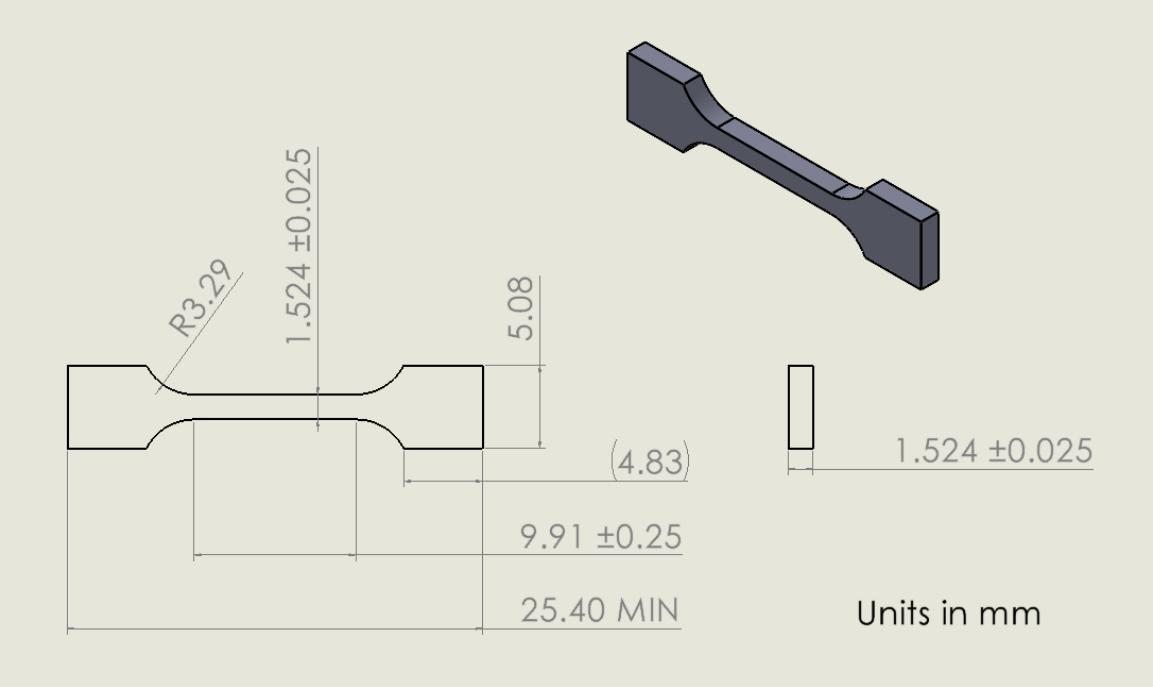


Figure A.19: Miniature tensile specimen dimensions used for tensile testing.

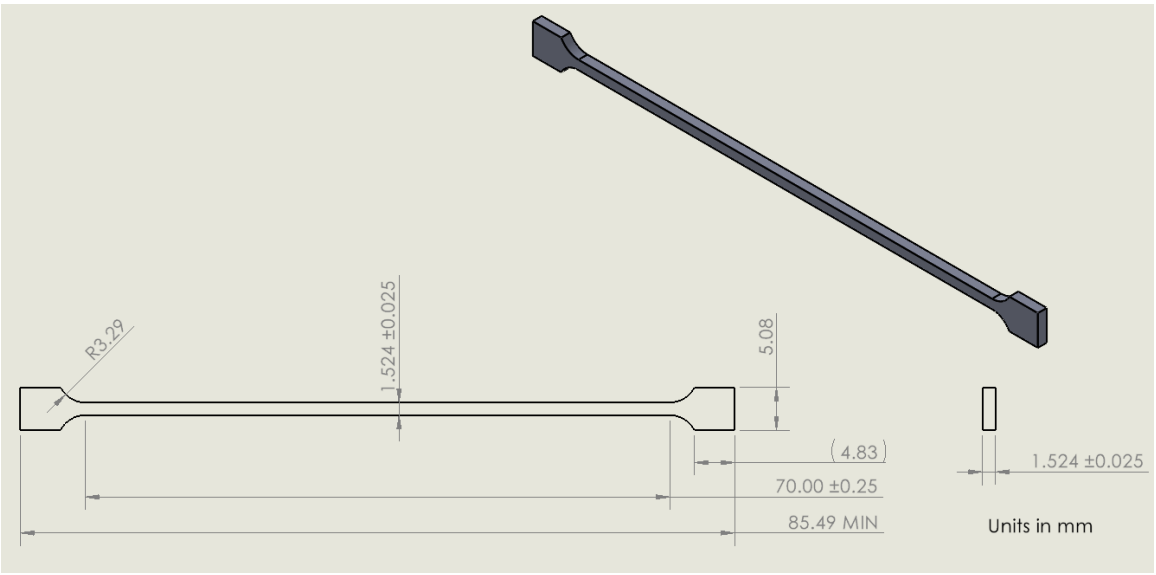


Figure A.20: Modified tensile specimen dimensions used for tensile testing.

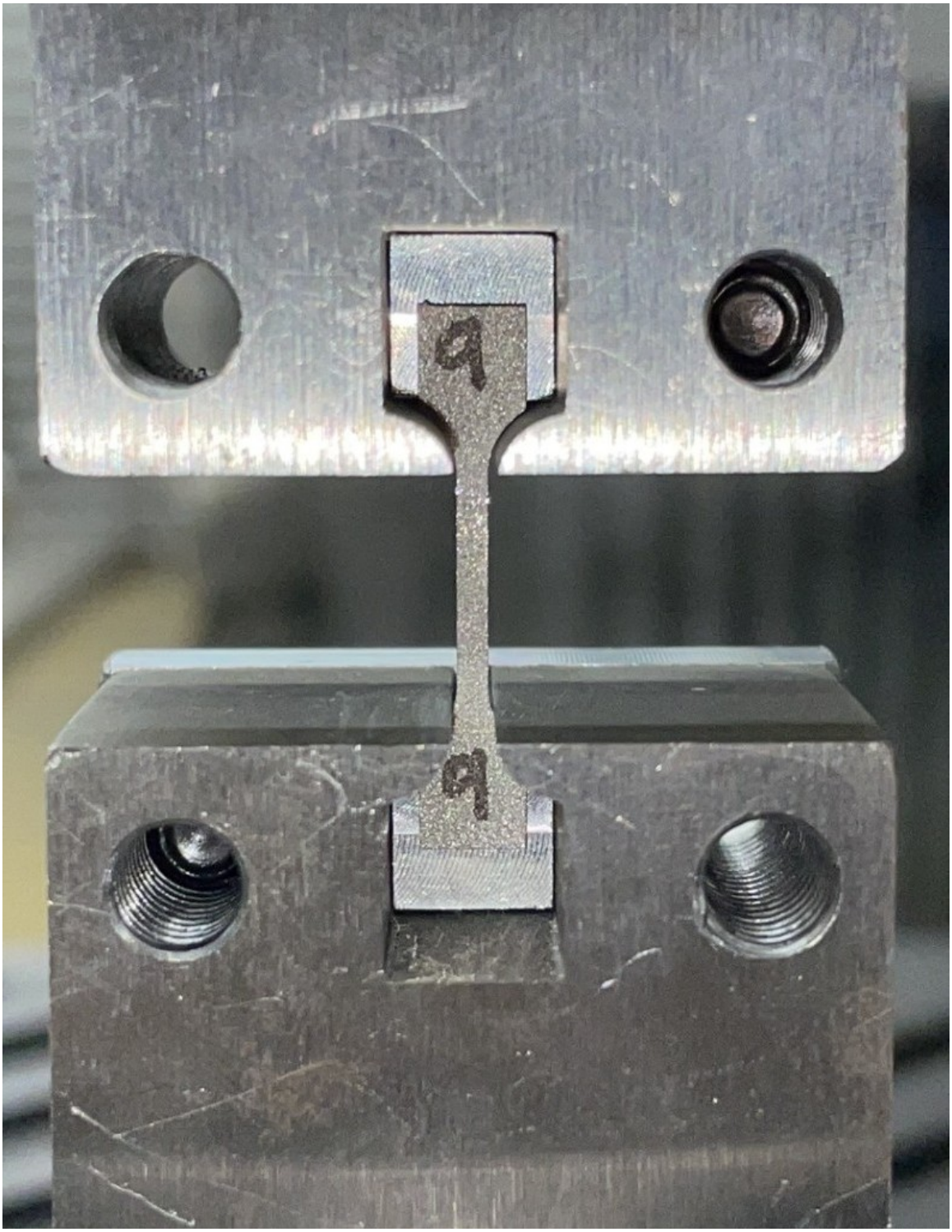


Figure A.21: Tensile grips used during tensile testing of the miniature tensile specimens.

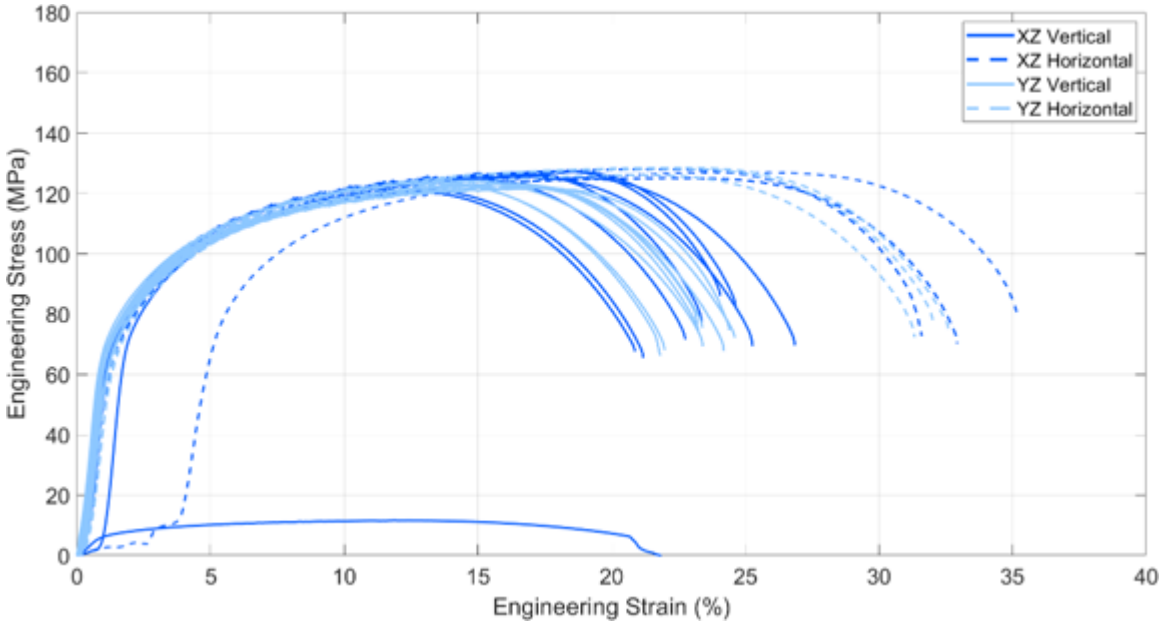


Figure A.22: Engineering stress-strain curves for the AD condition of Al6061 deposited via AFSD containing an outlier.

Table A.2: Yield Strength of Al6061 AFSD, Al4943 WAAM, and interfaces under AD and HT conditions.

Print Condition	**Vertical YS (MPa)**		**Horizontal YS (MPa)**	
	XZ	**YZ**	**XZ**	**YZ**
AD Al6061 AFSD	73.3 ± 4.8	71.1 ± 3.7	73.2 ± 9.1	72.2 ± 7.8
HT Al6061 AFSD	259.4 ± 13.5	263.8 ± 8.7	281.3 ± 28.1	281.7 ± 10.8
AD Al4943 WAAM	89.1 ± 6.3	91.6 ± 4.7	91.1 ± 6.0	90.8 ± 1.8
HT Al4943 WAAM	283.2 ± 5.9	281.2 ± 7.3	285.1 ± 2.2	281.4 ± 1.7
AD Interface (AD top AFSD surface)	114.0 ± 4.8	114.6 ± 8.5	–	–
HT Interface (AD top AFSD surface)	259.1 ± 14.5	270.0 ± 3.4	–	–
AD Interface (Machined top AFSD surface)	101.8 ± 6.6	105.2 ± 4.0	–	–
HT Interface (Machined top AFSD surface)	254.3 ± 13.3	273.9 ± 9.1	–	–
AD Interface (Machined side AFSD surface)	–	–	73.2 ± 4.8 (XY)	75.3 ± 5.6
HT Interface (Machined side AFSD surface)	–	–	278.6 ± 23.6 (XY)	277.0 ± 16.4
Wrought Al6061-T6	276	276	276	276

Table A.3: Ultimate Tensile Strength of Al6061 AFSD, Al4943 WAAM, and interfaces under AD and HT conditions.

Print Condition	**Vertical UTS (MPa)**		**Horizontal UTS (MPa)**	
	XZ	**YZ**	**XZ**	**YZ**
AD Al6061 AFSD	125.1 ± 5.1	123.3 ± 2.0	127.1 ± 3.3	127.7 ± 2.7
HT Al6061 AFSD	267.8 ± 12.6	269.3 ± 10.7	291.5 ± 28.6	301.3 ± 8.6
AD Al4943 WAAM	167.3 ± 5.9	164.8 ± 6.8	167.3 ± 8.4	161.5 ± 1.7
HT Al4943 WAAM	312.5 ± 3.1	310.1 ± 6.5	313.6 ± 2.6	313.4 ± 1.9
AD Interface (AD top AFSD surface)	158.6 ± 3.9	156.9 ± 11.3	–	–
HT Interface (AD top AFSD surface)	269.2 ± 25.3	290.7 ± 2.2	–	–
AD Interface (Machined top AFSD surface)	147.2 ± 5.5	145.6 ± 3.3	–	–
HT Interface (Machined top AFSD surface)	262.1 ± 15.4	281.0 ± 15.6	–	–
AD Interface (Machined side AFSD surface)	–	–	123.8 ± 4.3 (XY)	122.7 ± 4.6
HT Interface (Machined side AFSD surface)	–	–	299.5 ± 26.8 (XY)	290.0 ± 31.5
Wrought Al6061-T6	310	310	310	310

Table A.4: Total elongation at fracture of Al6061 AFSD, Al4943 WAAM, and interfaces under AD and HT conditions.

Print Condition	**Vertical Elongation (%)**		**Horizontal Elongation (%)**	
	XZ	**YZ**	**XZ**	**YZ**
AD Al6061 AFSD	23.63 ± 4.05	23.37 ± 1.96	31.95 ± 1.71	31.98 ± 1.26
HT Al6061 AFSD	7.18 ± 3.02	6.55 ± 4.35	12.07 ± 14.97	6.41 ± 4.68
AD Al4943 WAAM	15.07 ± 3.03	14.82 ± 3.24	19.14 ± 1.22	13.7 ± 0.8
HT Al4943 WAAM	13.18 ± 1.99	12.42 ± 2.83	11.53 ± 4.43	11.45 ± 2.94
AD Interface (AD top AFSD surface)	14.11 ± 2.09	13.56 ± 6.74	–	–
HT Interface (AD top AFSD surface)	7.86 ± 3.62	7.49 ± 5.29	–	–
AD Interface (Machined top AFSD surface)	14.44 ± 1.13	13.5 ± 1.76	–	–
HT Interface (Machined top AFSD surface)	7.03 ± 7.13	5.68 ± 3.62	–	–
AD Interface (Machined side AFSD surface)	–	–	21.37 ± 2.06 (XY)	18.98 ± 0.93
HT Interface (Machined side AFSD surface)	–	–	9.81 ± 5.18 (XY)	9.27 ± 4.13
Wrought Al6061-T6	12	12	12	12

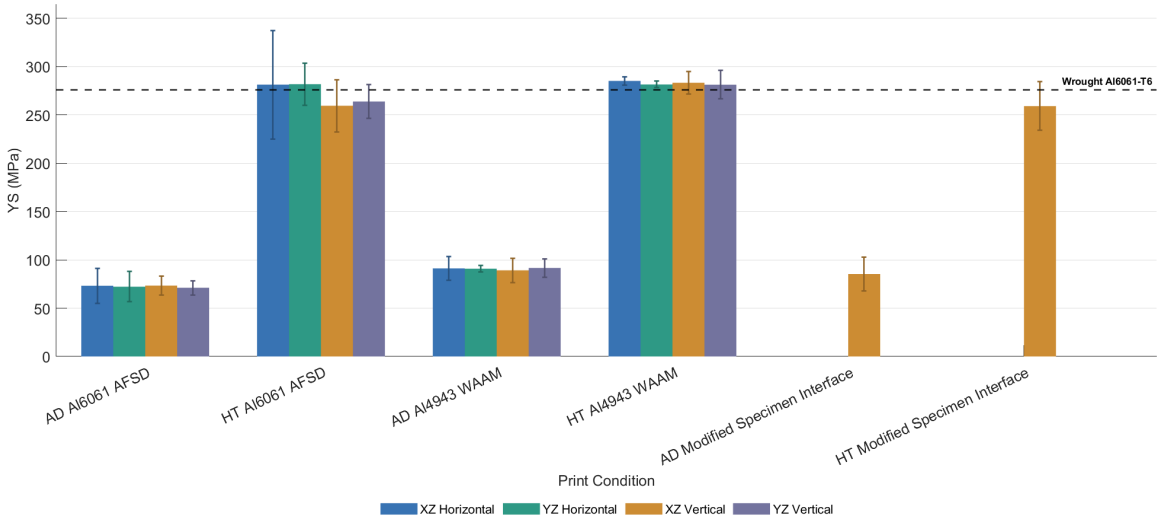


Figure A.23: Yield strength of the modified tensile specimens compared to the parent alloys.

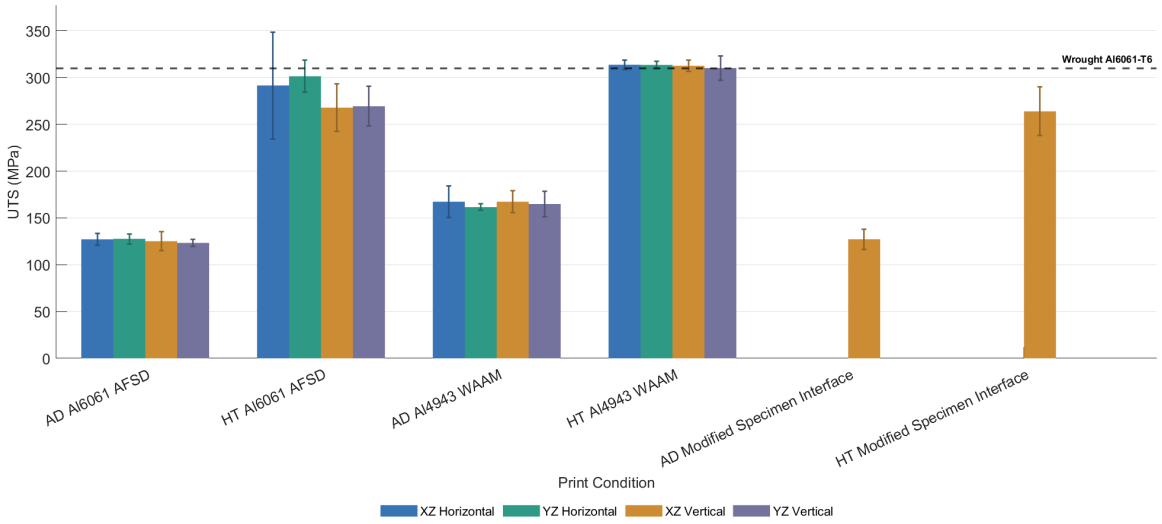


Figure A.24: Ultimate tensile strength of the modified tensile specimens compared to the parent alloys.

A.3.6 Fractography

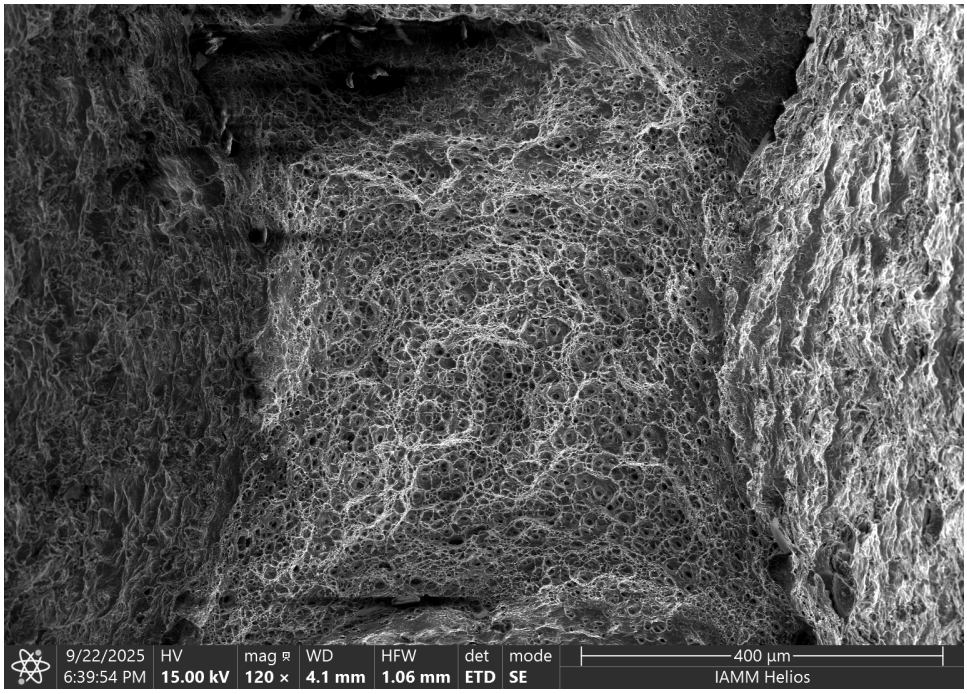


Figure A.25: Higher magnification of the fracture surface in the AD condition of Al6061 deposited via AFSD.

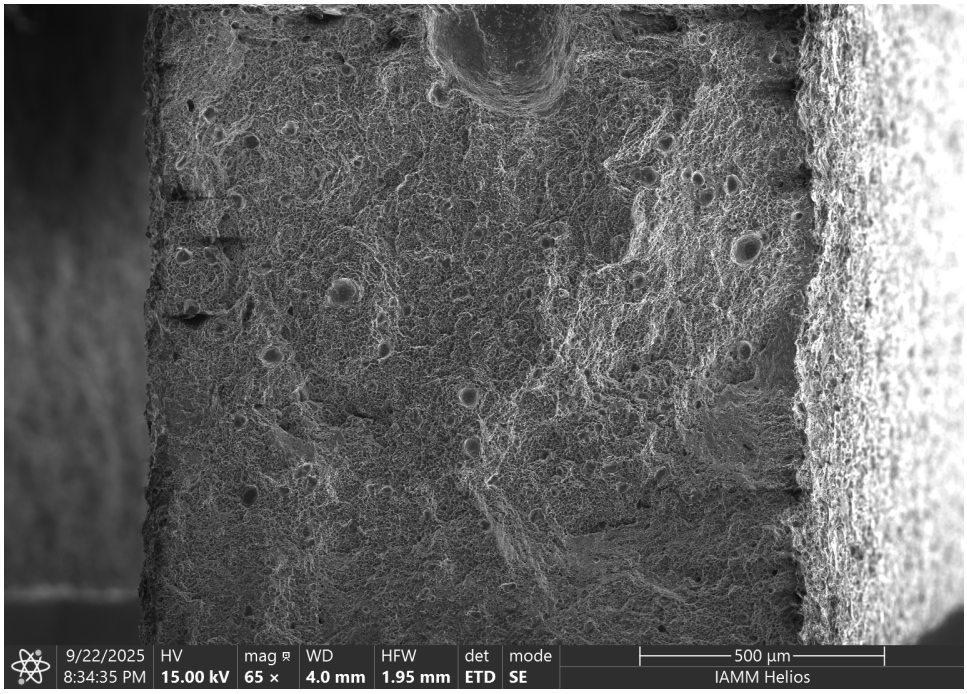


Figure A.26: Fracture surface in the HT condition of Al4943 deposited via WAAM where porosity is observed.

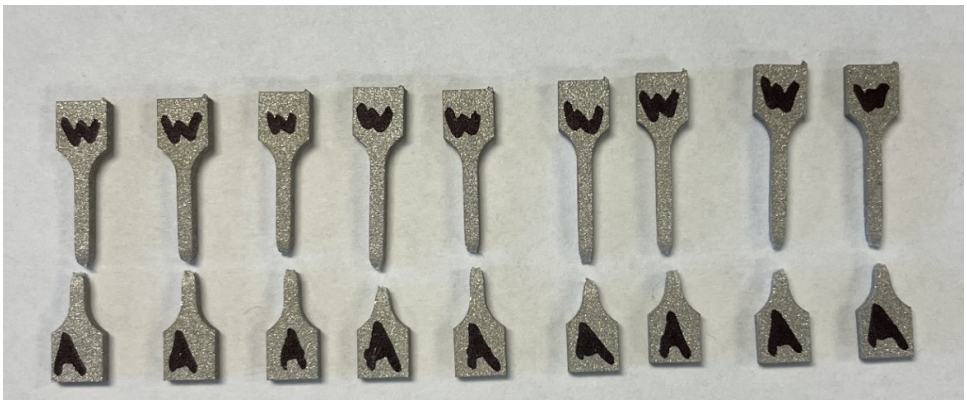


Figure A.27: Fracture location of the Al4943 WAAM deposited on the AD AFSD top surface when in the AD condition.

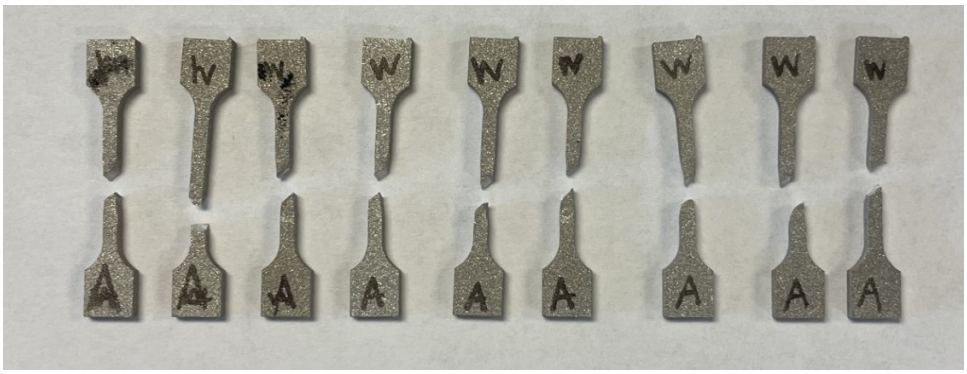


Figure A.28: Fracture location of the Al4943 WAAM deposited on the AD AFSD top surface when in the HT condition.

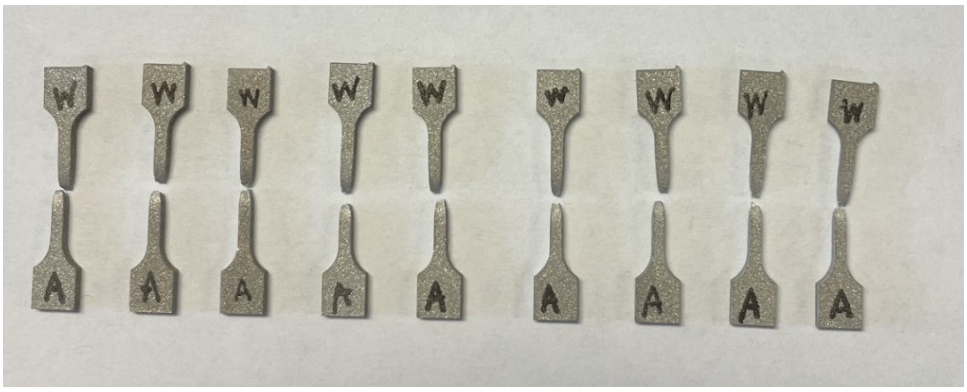


Figure A.29: Fracture location of the Al4943 WAAM deposited on the machined AFSD side surface when in the AD condition.

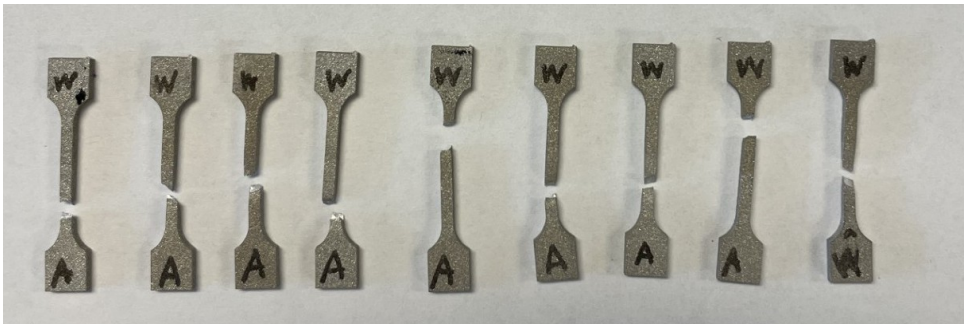


Figure A.30: Fracture location of the Al4943 WAAM deposited on the machined AFSD side surface when in the HT condition.



Figure A.31: Fracture location of the modified specimens when in the AD condition.



Figure A.32: Fracture location of the modified specimens when in the HT condition.

Vita

Kamren Sargent was born and raised in Dallas, Texas. He earned his B.S. in Mechanical and Energy Engineering from the University of North Texas in 2023. He started at the University of Tennessee, Knoxville in 2024 to pursue a Masters in Mechanical Engineering. During his time at the University of Tennessee, he completed work in robotic WAAM, robotic machining and AFSD. He completed his thesis that was focused on aluminum WAAM and AFSD. Post graduation, he plans to join the private industry and continue to work within the metal additive space.